

**UNIVERSIDADE DE SÃO PAULO
INSTITUTO DE FÍSICA DE SÃO CARLOS**

Tiago de Campos

**Spin-orbit coupling effects and g-factors in zinc-blende
InSb and wurtzite InAs nanowires using realistic
multiband $k \cdot p$ method**

São Carlos

2017

Tiago de Campos

**Spin-orbit coupling effects and g-factors in zinc-blende
InSb and wurtzite InAs nanowires using realistic
multiband $k \cdot p$ method**

Thesis presented to the Graduate Program
in Physics at the Instituto de Física de São
Carlos Universidade de São Paulo, to obtain
the degree of Doctor of Science.

Concentration area: Applied Physics
Option: Computational Physics

Advisor: Prof. Dr. Guilherme Matos Sipahi

Corrected version
(Original version available on the Program Unit)

São Carlos

2017

I AUTHORIZE THE REPRODUCTION AND DISSEMINATION OF TOTAL OR PARTIAL COPIES OF THIS DOCUMENT, BY CONVENCIONAL OR ELECTRONIC MEDIA FOR STUDY OR RESEARCH PURPOSE, SINCE IT IS REFERENCED.

Cataloguing data revised by the Library and Information Service
of the IFSC, with information provided by the author

Campos, Tiago de

Spin-orbit coupling effects and g-factors in zinc-blende InSb and wurtzite InAs nanowires using realistic multiband $k \cdot p$ method / Tiago de Campos; advisor Guilherme Matos Sipahi - revised version -- São Carlos 2017.

155 p.

Thesis (Doctorate - Graduate Program in Física Aplicada Computacional) -- Instituto de Física de São Carlos, Universidade de São Paulo - Brasil , 2017.

1. Spin-orbit. 2. g-factor. 3. Nanowires. 4. InSb.
5. InAs. I. Sipahi, Guilherme Matos, advisor. II. Title.

*In memory of my father.
To my family and wife who
supported me all these years.*

ACKNOWLEDGEMENTS

I'd like to thank my wife, Jéssica R. S. de Campos, my mother Renata P. R. de Campos, my sister Talita de Campos and my grandparents Francisco and Sebastiana for their immense support and dedication through the years. I also would like to thank my father and mother in law, Délcio and Sandra, who have always make the greatest effort to make me feel at home in their house.

I thank Prof. Dr. Guilherme Matos Sipahi for his supervision, scientific discussions, and for providing the opportunity to interact with great researchers whom are leading names in their areas. Being under your supervision brought me great life experiences.

A special thanks for the Brazilian friends who helped in my PhD either by scientific discussion or by 'chitchatting'. Paulo Eduardo F. Junior, my best man and former roommate who were 'not always' willing to discuss serious Physics, I thank you. Carlos M. O. Bastos, a special thanks for having the great idea to start to produce real, good and cheap beer of all sorts. Denis R. Candido, I thank you for studying hard, always helping me with 'topological stuffs'. I also could not let to thank the special friends: José Ricardo F. Ronqui for great discussions about libertarianism in the coffee hour; Cesar Uliana for always questioning my libertarian ideas; Renata Batista for being a good listener and fun person; Vinicius H. Aurichio for the computational discussions (and others as well); Agide Marassi for your peculiar enthusiasm; Lucas Assirati and Guilherme Bagnato for being my friends since the undergraduation times.

Also, a special thanks for the friends I made abroad: Petra Högl, Susanne Irmer and Tobias Frank for sharing the office space, and kindly help me in my PhD sandwich period at Universität Regensburg; Martin Gmitra for providing good insights; Jeongsu Lee for being a good friend in all times; Denis Kochan and Marcin Kurpas for their friendship.

Prof. Dr. Jaroslav Fabian, I thank you very much for all the effort in put in this work and also for kindly provide the unforgettable opportunity I had at Universität Regensburg. The discussions I had with you and your group enriched my scientific knowledge.

Prof. Dr. Igor Žutić, I thank you very much for kindly host me at Buffalo and also provide me with the opportunity to make my Post-Doctoral research with you.

I also would like to thank the people at IFSC from their help and dedication. Specially Silvio, Ricardo, Sonia, Paulo, Italo and Maria Cristina.

CNPq for the financial support of PhD scholarship (grant No. 149904/2013-4) and CAPES for the financial support of my Sandwich period at Regensburg (grant No. 88881.068174/2014-01).

Lastly but not least I leave my special thanks to all the libertarian thinkers who help spread the idea that freedom, and only freedom, will make a better world.

“There are two ways to be fooled. One is to believe what isn't true. The other is to refuse to accept what is true.”

Soren Kierkegaard

ABSTRACT

CAMPOS, T. **Spin-orbit coupling effects and g-factors in zinc-blende InSb and wurtzite InAs nanowires using realistic multiband $\mathbf{k} \cdot \mathbf{p}$ method.** 2017. 155p. Tese (Doutorado em Ciências) - Instituto de Física de São Carlos, Universidade de São Paulo, São Carlos, 2017.

Spin-dependent phenomena in semiconductor nanowires have recently gained a lot of attention, in special because these nanostructures can be a viable setup to study exotic states of matter like the Majorana fermions. One of the key ingredients to accommodate the Majorana zero modes is the spin-orbit coupling in the nanowires, which has been usually treated with two-band Hamiltonians. The spin-orbit coupling in semiconductors arise from two distinct sources being the bulk inversion asymmetry, when the unit cell does not present inversion symmetry, e.g. when the crystal unit cell is composed by two different atoms, and the structural inversion asymmetry, when the whole system does not have a mirror symmetry. To describe the system these effective models take as input, parameters that are dependent on the system configuration and measurement setups. Although these effective models have been successful in determine relevant physical properties, a more realistic description of the interacting energy bands is required, specially in quantum confined systems where the interplay between both sources of spin-orbit coupling can change the system's properties in non-trivial ways. For instance, in quantum wells there is an anisotropy of the g-factor due to the quantum confinement and structural inversion asymmetry. Furthermore, the in-plane g-factor also have an anisotropy which is due to the intrinsic spin-orbit coupling and it is not captured by these effective models. In this study, we use realistic multiband $\vec{k} \cdot \vec{p}$ Hamiltonians, including both spin-orbit coupling mechanisms, to determine the band structure of zincblende InSb and wurtzite InAs nanowires under a transverse electric field. We analyze the effects of the lateral quantum confinement for a hexagonal cross-section geometry and of the change in growth directions, extracting the relevant physical parameters for the first conduction subband. We found that the g-factors are heavily dependent on the quantum confinement and nanowire orientation, with in-plane/out-of-plane anisotropies up to 3%. We also found that for zinc-blende nanowires the extrinsic spin-orbit coupling is dominant over the intrinsic one whereas, for wurztize, the opposite behavior holds. In order to assess if the nanowires could host the aforementioned Majorana zero modes we investigate under which circumstances the topological phase transition occurs, using the Bogoliubov-de Gennes formalism to couple the nanowire with a superconductor, and we found that using realistic and experimental feasible parameters, indeed, the phase transition occurs. In conclusion, our systematic investigation of nanowires shows that the spin-orbit coupling energy can be fine tuned by the external electric field in experimentally achievable setups that ultimately could guide the search for the elusive Majorana modes. Moreover, our numerical approach

is not restricted to a specific material or dimensionality and can be used to study others systems to provide useful insights into the electronic and spintronic fields.

Keywords: Spin-orbit. g-factor. Nanowires. InSb. InAs.

RESUMO

CAMPOS, T. **Efeitos do acoplamento spin-órbita e fatores giromagnéticos em nanofios de blenda de zinco InSb e wurtzita InAs usando o método $k \cdot p$ multibanda.** 2017. 155p. Tese (Doutorado em Ciências) - Instituto de Física de São Carlos, Universidade de São Paulo, São Carlos, 2017.

Recentemente, fenômenos dependentes de spin em nanofios semicondutores se tornaram uma área de pesquisa ativa especialmente porque essas nanoestruturas podem ser viáveis para o estudo de estados exóticos da matéria como, por exemplo, os férmions de Majorana. Um dos ingredientes chave para que esses modos de excitação possam existir em nanofios é o acoplamento spin-órbita, o qual tem sido usualmente tratado com modelos de duas bandas. O acoplamento spin-órbita em semicondutores aparece de duas fontes distintas sendo elas a assimetria de inversão no *bulk*, quando a célula unitária do cristal não possui simetria de inversão, por exemplo, quando é formada por dois átomos diferentes, e a assimetria de inversão estrutural, quando o sistema como um todo não possui simetria de inversão. Para descrever o sistema, os modelos efetivos de duas bandas usam como entrada parâmetros que dependem tanto do sistema específico quanto da configuração do arranjo experimental. Apesar desses modelos terem sucesso em descrever algumas das propriedades físicas relevantes, uma descrição mais realística da interação entre as bandas de energia se faz necessária, especialmente em sistemas com confinamento quântico onde a ação combinada das duas fontes de acoplamento spin-órbita muda as propriedades do sistema de maneira não-trivial. Por exemplo, o fator giromagnético em poços quânticos é anisotrópico devido aos efeitos de ambos, confinamento quântico e a assimetria de inversão estrutural. Ademais, o fator giromagnético ao longo do plano também possui uma anisotropia, a qual tem origem no acoplamento spin-órbita intrínseco do sistema e não é capturada por esses modelos efetivos. Nesse estudo, nós usamos Hamiltonianos $\vec{k} \cdot \vec{p}$ multibanda, incluindo ambos os mecanismos de acoplamento spin-órbita, para determinar a estrutura de bandas de nanofios de InSb na fase blenda de zinco e InAs na fase wurtzita sob a ação de um campo elétrico transversal. Nós analisamos os efeitos do confinamento quântico lateral, para fios com seção transversal hexagonal, e diferentes direções de crescimento, extraíndo parâmetros físicos relevantes para a primeira sub-banda de condução. Nós encontramos que os fatores giromagnéticos são fortemente influenciados pelo confinamento quântico e orientação dos nanofios, com anisotropias no plano e fora do plano de até 3%. Nós também encontramos que para nanofios de InSb na fase blenda de zinco, o acoplamento spin-órbita extrínseco domina o intrínseco enquanto que, em nanofios de InAs na fase wurtzita, vale o oposto. Para avaliar se os nanofios podem hospedar os modos de Majorana de energia zero nós investigamos sob quais circunstâncias a transição de fase topológica ocorre usando o formalismo de Bogoliubov-de Gennes para acoplar o nanofio a um supercondutor, e

encontramos que usando nossos parâmetros e em condições experimentalmente factíveis, de fato, a transição de fase ocorre. Em conclusão, nossa investigação sistemática nos nanofios mostrou que o acoplamento spin-órbita pode ser ajustado por fontes externas, tais como um campo elétrico aplicado, e em configurações experimentais factíveis e que ultimamente pode guiar à busca dos elusivos modos de Majorana. Além do mais, nossa abordagem numérica não é restrita a esses materiais em específico e nem a nanofios, podendo ser usada para estudar outros sistemas provendo intuições úteis nos campos de eletrônica e spintrônica.

Palavras-chave: Spin-órbita. g-factor. Nanofios. InSb. InAs.

LIST OF FIGURES

Figure 1 – Effect of the spin-orbit coupling in a crystal without inversion symmetry, either bulk or structural. a) Degenerate bands without spin-orbit coupling and b) spin split bands, with visual representation of the spin-orbit coupling energy, E_{SO}	30
Figure 2 – Bust of Ettore Majorana at Sapienza University of Rome.	31
Figure 3 – Heterostructure with a 1D confinement profile. The junction of two or more materials creates a confinement profile along the growth direction.	47
Figure 4 – Bulk band scheme and first Brillouin zone for a zinc-blende crystal. In a) we depict the 14 bands taken into account in the Extended Kane model. In b) we show the Brillouin zone and its high symmetry points.	53
Figure 5 – Representation of the new coordinate axis in the old frame of reference. We are rotating the $[001]$ to the $[110]$, i. e., we want the \hat{z} to be transformed to \hat{z}'	59
Figure 6 – Representation of the new coordinate axis in the old frame of reference. We are rotating the $[001]$ to the $[111]$, i. e., we want the \hat{z} direction to be transformed to \hat{z}'	61
Figure 7 – Bulk band scheme and first Brillouin zone for a wurtzite crystal. In a) we depict the 8 bands taken into account in the wurtzite model. In b) we show the Brillouin zone with the high symmetry points. The energy labels are, in the Chuang & Chang ¹⁴⁵ notation: $E_c = E_g + \Delta_1 + \Delta_2$, $E_1^0 = \Delta_1 + \Delta_2$, $E_2^0 = \frac{\Delta_1 - \Delta_2}{2} + \sqrt{\left(\frac{\Delta_1 - \Delta_2}{2}\right)^2 + 2\Delta_3^2}$ and $E_3^0 = \frac{\Delta_1 - \Delta_2}{2} - \sqrt{\left(\frac{\Delta_1 - \Delta_2}{2}\right)^2 + 2\Delta_3^2}$, where E_g is the gap energy, Δ_1 is the crystal field splitting (due to the distinction between z and xy) and Δ_2 and Δ_3 are the spin-orbit coupling energies.	62
Figure 8 – Representation of the new coordinate axis in the old frame of reference. We are rotating the $[0001]$ to the $[11\bar{2}0]$, i. e., we want the \hat{z} direction to be transformed to \hat{z}'	66

Figure 9 – Representation of the new coordinate axis in the old frame of reference. We are rotating the $[0001]$ to the $[10\bar{1}0]$, i. e., we want the \hat{z} direction to be transformed to \hat{z}'	67
Figure 10 – Spin-orbit coupling field. a) Spherical plot of the magnitude of the Dresselhaus spin-orbit field in the momentum space. b) Dresselhaus vector field over the Fermi sphere.	80
Figure 11 – Spin-orbit coupling field. a,c) Spherical plot of the magnitude of the spin-orbit field in the momentum space for two distinct momenta k_a and k_c where $k_a > k_c$. b,d) Vector field over the Fermi sphere.	81
Figure 12 – Energy dispersion of the BdG model. The outer solid lines corresponds to the s-wave coupling whereas the inner solid to the p-wave coupling. The inner dashed corresponds to the case where the superconducting proximity effect coupling, Δ , is turned off. The arrow on the right side indicates the main energy separation of the bands. $E_{\text{pwave}} \approx \Delta$	87
Figure 13 – a) Schematics of a hexagonal NW and the coordinate axes we use in the text. The nanowire growth direction is along z , and the electric field is applied along the y -direction. The wire diameter is L , which is the distance between the opposite vertices of the hexagon. In b) and c) we show the growth planes for ZB and WZ crystals, respectively. The shaded regions inside the conventional unit cells indicate the crystal planes perpendicular to the growth directions. The coordinate axes with respect to the crystal orientations are also indicated for $[001]$ ZB and $[0001]$ WZ structures. These are the same axes as used in the confinement geometry a).	92

Figure 14 – Schematics of the band mismatch. On the left, for the ZB 14-band model both the lowest s and the highest p conduction bands have the same mismatch to the vacuum region. On the right, for WZ 8-band model, the distinction is that, besides the lack of the highest p conduction bands, the p valence bands have an extra splitting (due to the crystal field) at Γ -point, making the p valence bands only spin degenerate. In the figure, the energy labels are, in the Ref. 145 notation: $E_c = E_g + \Delta_1 + \Delta_2$, $E_1^0 = \Delta_1 + \Delta_2$, $E_2^0 = \frac{\Delta_1 - \Delta_2}{2} + \sqrt{\left(\frac{\Delta_1 - \Delta_2}{2}\right)^2 + 2\Delta_3^2}$ and $E_3^0 = \frac{\Delta_1 - \Delta_2}{2} - \sqrt{\left(\frac{\Delta_1 - \Delta_2}{2}\right)^2 + 2\Delta_3^2}$, where E_g is the gap energy, Δ_1 is the crystal field splitting (due to the distinction between z and xy) and Δ_2 and Δ_3 are the spin-orbit coupling energies. 95

Figure 15 – Aliasing and Gibbs phenomena. a) Sampling leads to ambiguous frequencies given the same value at sampling point. b) Overshoot (or undershoot) of the values of reconstructed signal at a discontinuity suppressed by application of the Nuttall window.¹⁹⁵ 96

Figure 16 – a), b) and c) show the g_x^* , g_y^* and g_z^* for zinc-blende InSb nanowires, respectively. d), e) and f) show the g_x^* , g_y^* and g_z^* for wurtzite InAs nanowires, respectively. The g-factors were determined without an applied electric field. In the wurtzite case, for notation simplicity, we labeled both orientations ($[10\bar{1}0]$ and $[11\bar{2}0]$) as $[10\bar{1}0]$ 98

Figure 17 – g-factor anisotropy, as defined in Eq. (3.2). a), b) and c) show the Δg_{zx}^* , Δg_{zy}^* and Δg_{xy}^* for zinc-blende InSb nanowires, respectively. d), e) and f) show the Δg_{zx}^* , Δg_{zy}^* and Δg_{xy}^* for wurtzite InAs nanowires, respectively. The g-factors anisotropy were determined without an applied electric field. In the wurtzite case, for notation simplicity, we labeled both orientations ($[10\bar{1}0]$ and $[11\bar{2}0]$) as $[10\bar{1}0]$ 99

Figure 18 – Crosssectional cut of the spin-orbit coupling along the growth directions for ZB and WZ. 100

Figure 19 – a) Quadratic fit to the $\mathbf{k} \cdot \mathbf{p}$ calculated lowest conduction band structure around Γ of InAs wurtzite nanowire oriented along $[0001]$. The wire diameter is 60 nm, and the applied electric field 1 mV/nm. b) Spin-orbit splitting of the band in a) divided by momentum. This line is fitted to obtain the linear and cubic spin-orbit coefficients.	102
Figure 20 – a) Atomic arrangement along $[001]$ orientation of a zinc-blende structure with indicated x and y axis. b) Mirror symmetry planes of the atomic structure (solid) and of the hexagonal confinement (dashed).	103
Figure 21 – Calculated electronic subband dispersion for a zinc-blende InSb hexagonal nanowire of 60 nm diameter oriented along $[001]$ direction. a) With applied electric field along x axis and b) along y axis. In each subfigure the left most spectrum corresponds to an electric field of $E = -4$ mV/nm, the central panel to zero applied electric field and the right most spectrum is for an electric field $E = 4$ mV/nm.	104
Figure 22 – Zoom of the calculated first conduction subband of $[001]$ oriented InSb zinc-blende nanowire at: a) zero; b) finite electric field, $E_x = 4$ mV/nm, along the x axis; and c) finite electric field, $E_y = 4$ mV/nm, along the y axis. In b) and c) we show, in the insets, the SIA induced spin-orbit splitting of the first conduction subband.	105
Figure 23 – a) and c), linear spin-orbit splitting coefficients, ΔS_L ; b) and d) cubic spin-orbit splitting coefficients, ΔS_C , for different diameters L , for InSb zincblende nanowires oriented along $[001]$. In a) and b), the applied electric field goes along the x axis and in c) and d) along the y axis.	106
Figure 24 – Calculated spin-orbit energy, for different diameters L_x and different transverse electric fields E , for InSb zincblende nanowires oriented along $[001]$. a) applied electric field along x axis and b) along y axis.	107
Figure 25 – a) Atomic arrangement along $[110]$ orientation of a zinc-blende structure with indicated x and y axis. b) Mirror symmetry planes of the atomic structure (solid) and of the hexagonal confinement (dashed).	107

Figure 26 – Calculated electronic subband dispersion for a zinc-blende InSb hexagonal nanowire of 60 nm diameter oriented along [110] direction. a) With applied electric field along x axis and b) along y axis. In each subfigure the left most spectrum corresponds to an electric field of $E = -4$ mV/nm, the central panel to zero applied electric field and the right most spectrum is for an electric field $E = 4$ mV/nm.	108
Figure 27 – Zoom of the calculated first conduction subband of [110] oriented InSb zinc-blende nanowire at: a) finite electric field, $E_x = -4$ mV/nm, along the x axis; b) zero field; c) finite electric field, $E_x = 4$ mV/nm, along the x axis; and d) finite electric field, $E_y = 4$ mV/nm, along the y axis. In b), in the inset, we show the confinement BIA induced spin-orbit splitting and in a), c) and d), the SIA induced spin-orbit splitting of the first conduction subband.	109
Figure 28 – a) and c), linear spin-orbit splitting coefficients, ΔS_L ; b) and d) cubic spin-orbit splitting coefficients, ΔS_C , for different diameters L , for InSb zincblende nanowires oriented along [110] . In a) and b), the applied electric field goes along the x axis and in c) and d) along the y axis. . .	110
Figure 29 – Calculated spin-orbit energy, for different diameters L_x and different transverse electric fields E , for InSb zincblende nanowires oriented along [110] . a) applied electric field along x axis and b) along y axis.	111
Figure 30 – a) Atomic arrangement along [111] orientation of a zinc-blende structure with indicated x and y axis. b) Mirror symmetry planes of the atomic structure (solid) and of the hexagonal confinement (dashed).	111
Figure 31 – Calculated electronic subband dispersion for a zinc-blende InSb hexagonal nanowire of 60 nm diameter oriented along [111] direction. a) With applied electric field along x axis and b) along y axis. In each subfigure the left most spectrum corresponds to an electric field of $E = -4$ mV/nm, the central panel to zero applied electric field and the right most spectrum is for an electric field $E = 4$ mV/nm.	112

Figure 32 – Zoom of the calculated first conduction subband of [111] oriented InSb zinc-blende nanowire at: a) finite electric field, $E_x = -4$ mV/nm, along the x axis; b) zero field; c) finite electric field, $E_x = 4$ mV/nm, along the x axis; and d) finite electric field, $E_y = 4$ mV/nm, along the y axis. In the insets of a), c) and d) we show the SIA induced spin-orbit splitting of the first conduction subband.	113
Figure 33 – a) and c), linear spin-orbit splitting coefficients, ΔS_L ; b) and d) cubic spin-orbit splitting coefficients, ΔS_C , for different diameters L , for InSb zincblende nanowires oriented along [111] . In a) and b), the applied electric field goes along the x axis and in c) and d) along the y axis. . .	114
Figure 34 – Calculated spin-orbit energy, for different diameters L_x and different transverse electric fields E , for InSb zincblende nanowires oriented along [111] . a) applied electric field along x axis and b) along y axis.	115
Figure 35 – Spin orientation of [001] oriented zincblende nanowires. With electric field applied along a) x axis and b) y -axis.	119
Figure 36 – Spin orientation of [110] oriented zincblende nanowires. With electric field applied along a) x axis and b) y -axis. The tiled arrow in b) represents the mixing of BIA and SIA spin-orbit coupling, actually the BIA contribution to the spin orientation is about 1/10 of the SIA contribution.	119
Figure 37 – Spin orientation of [111] oriented zincblende nanowires. With electric field applied along a) x axis and b) y -axis. The tiled arrow in b) represents the mixing of BIA and SIA spin-orbit coupling, actually the BIA contribution to the spin orientation is about 1/10 of the SIA contribution.	120
Figure 38 – a) Atomic arrangement along [0001] orientation of a wurtzite structure with indicated x and y axis. b) Mirror symmetry planes of the atomic structure (solid) and of the hexagonal confinement (dashed). In b), the dotted line represents the WZ glide planes, i. e., they need an extra translation of $\frac{c}{2}$ along the z direction.	120

- Figure 39 – Calculated electronic subband dispersion for a wurtzite InAs hexagonal nanowire of 60 nm diameter oriented along $[0001]$ direction. a) With applied electric field along x axis and b) along y axis. In each subfigure the left most spectrum corresponds to an electric field of $E = -4$ mV/nm, the central panel to zero applied electric field and the right most spectrum is for an electric field $E = 4$ mV/nm. 121
- Figure 40 – Zoom of the calculated first conduction subband of $[0001]$ oriented InAs wurtzite nanowire at: a) zero; b) finite electric field, $E_x = 4$ mV/nm, along the x axis; and c) finite electric field, $E_y = 4$ mV/nm, along the y axis. In b) and c) we show, in the insets, the SIA induced spin-orbit splitting of the first conduction subband. 122
- Figure 41 – a) and c), linear spin-orbit splitting coefficients, ΔS_L ; b) and d) cubic spin-orbit splitting coefficients, ΔS_C , for different diameters L , for InAs wurtzite nanowires oriented along $[0001]$. In a) and b), the applied electric field goes along the x axis and in c) and d) along the y axis. . . 123
- Figure 42 – Calculated spin-orbit energy, for different diameters L_x and different transverse electric fields E , for InAs wurtzite nanowires oriented along $[0001]$. a) applied electric field along x axis and b) along y axis. . . . 124
- Figure 43 – a) Atomic arrangement along $[10\bar{1}0]$ orientation of a wurtzite structure with indicated x and y axis. b) Mirror symmetry planes of the atomic structure (solid) and of the hexagonal confinement (dashed). 125
- Figure 44 – a) Atomic arrangement along $[11\bar{2}0]$ orientation of a wurtzite structure with indicated x and y axis. b) Mirror symmetry planes of the atomic structure (solid) and of the hexagonal confinement (dashed). 125
- Figure 45 – Calculated electronic subband dispersion for a wurtzite InAs hexagonal nanowire of 60 nm diameter oriented along $[10\bar{1}0]$ or $[11\bar{2}0]$ direction. a) With applied electric field along x axis and b) along y axis. In each subfigure the left most spectrum corresponds to an electric field of $E = -4$ mV/nm, the central panel to zero applied electric field and the right most spectrum is for an electric field $E = 4$ mV/nm. 126

Figure 46 – Zoom of the calculated first conduction subband of $[10\bar{1}0]$ or $[11\bar{2}0]$ oriented InAs wurtzite nanowire at: a) finite electric field, $E_x = -4$ mV/nm, along the x axis; b) zero field; c) finite electric field, $E_x = 4$ mV/nm, along the x axis; and d) finite electric field, $E_y = 4$ mV/nm, along the y axis. In b), in the inset, we show the confinement BIA induced spin-orbit splitting and in a), c) and d), the SIA induced spin-orbit splitting of the first conduction subband. 127

Figure 47 – a) and c), linear spin-orbit splitting coefficients, ΔS_L ; b) and d) cubic spin-orbit splitting coefficients, ΔS_C , for different diameters L , for InAs wurtzite nanowires oriented along $[10\bar{1}0]$ or $[11\bar{2}0]$. In a) and b), the applied electric field goes along the x axis and in c) and d) along the y axis. 128

Figure 48 – Calculated spin-orbit energy, for different diameters L_x and different transverse electric fields E , for InAs wurtzite nanowires oriented along $[10\bar{1}0]$ or $[11\bar{2}0]$. a) applied electric field along x axis and b) along y axis. 129

Figure 49 – Spin orientation of $[0001]$ oriented wurtzite nanowires. With electric field applied along a) x axis and b) y -axis. 131

Figure 50 – Spin orientation of $[10\bar{1}0]$ or $[11\bar{2}0]$ oriented wurtzite nanowires. With electric field applied along a) x axis and b) y -axis. The tiled arrow in b) represents the mixing of BIA and SIA spin-orbit coupling, actually the SIA contribution to the spin orientation is about 1/10 of the BIA contribution. 132

Figure 51 – Zinb-blende InSb nanowire with $L = 100$ nm with magnetic field applied along the nanowire axis (and perpendicular to the spin-orbit coupling) and superconductivity proximity effect. a) Lowest subband spectrum for $\mu = B = \Delta = 0$. b) Excitation spectrum of the creation or annihilation of an electron for $\mu = B = \Delta = 0$. c) Excitation spectrum for $B = 0.15$ T, $\Delta = \mu = 0$ where Zeeman splitting opens a gap at $k_z = 0$. d) $B = 0.15$ T, $\Delta = 0.25$ meV, $\mu = 0$ with a superconducting gap for $k_z \neq 0$ and a Zeeman gap near $k_z = 0$. e) $B = 0.15$ T, $\Delta = 0.369$ meV, $\mu = 0$ meaning $V_z = \Delta$ where the gap at $k_z = 0$ is closed meaning a phase transition. f) $B = 0.15$ T, $\Delta = 0.045$ meV, $\mu = 0$ here the gap reopens confirming the phase transition. g) $B = 0.15$ T, $\Delta = 0.25$ meV, $\mu = 0.2715$ meV meaning $V_z^2 = \Delta^2 + \mu^2$, the gap at $k_z = 0$ also closes driven by the changes in the chemical potential. h) $B = 0.15$ T, $\Delta = 0.25$ meV, $\mu = 0.4$ meV the gap at $k_z = 0$ reopens, signaling the phase transition. 133

Figure 52 – Wurtzite InAs nanowire oriented along $[0001]$ direction with $L = 100$ nm and magnetic field applied along the x axis (perpendicular to both the nanowire main axis and the spin-orbit coupling) and superconductivity proximity effect. a) Lowest subband spectrum for $\mu = B = \Delta = 0$. b) Excitation spectrum of the creation or annihilation of an electron for $\mu = B = \Delta = 0$. c) Excitation spectrum for $B = 0.1$ T, $\Delta = \mu = 0$ where Zeeman splitting opens a gap at $k_z = 0$. d) $B = 0.1$ T, $\Delta = 0.045$ meV, $\mu = 0$ with a superconducting gap for $k_z \neq 0$ and a Zeeman gap near $k_z = 0$. e) $B = 0.1$ T, $\Delta = 0.058$ meV, $\mu = 0$ meaning $V_z = \Delta$ where the gap at $k_z = 0$ is closed meaning a phase transition. f) $B = 0.1$ T, $\Delta = 0.07$ meV, $\mu = 0$ here the gap reopens confirming the phase transition. g) $B = 0.1$ T, $\Delta = 0.045$ meV, $\mu = 0.0366$ meV meaning $V_z^2 = \Delta^2 + \mu^2$, the gap at $k_z = 0$ also closes driven by changes in the chemical potential. h) $B = 0.1$ T, $\Delta = 0.045$ meV, $\mu = 0.05$ meV the gap at $k_z = 0$ reopens, signaling the phase transition. 135

Figure 53 – Wurtzite InAs nanowire oriented along $[10\bar{1}0]$ or $[11\bar{2}0]$ direction with $L = 100$ nm and magnetic field applied along the x axis (perpendicular to both the nanowire main axis and the spin-orbit coupling) and superconductivity proximity effect. a) Lowest subband spectrum for $\mu = B = \Delta = 0$. b) Excitation spectrum of the creation or annihilation of an electron for $\mu = B = \Delta = 0$. c) Excitation spectrum for $B = 0.15$ T, $\Delta = \mu = 0$ where Zeeman splitting opens a gap at $k_z = 0$. d) $B = 0.15$ T, $\Delta = 0.045$ meV, $\mu = 0$ with a superconducting gap for $k_z \neq 0$ and a Zeeman gap near $k_z = 0$. e) $B = 0.15$ T, $\Delta = 0.0695$ meV, $\mu = 0$ meaning $V_z = \Delta$ where the gap at $k_z = 0$ is closed meaning a phase transition. f) $B = 0.15$ T, $\Delta = 0.08$ meV, $\mu = 0$ here the gap reopens confirming the phase transition. g) $B = 0.15$ T, $\Delta = 0.045$ meV, $\mu = 0.045$ meV meaning $V_z^2 = \Delta^2 + \mu^2$, the gap at $k_z = 0$ also closes driven by changes in the chemical potential. h) $B = 0.15$ T, $\Delta = 0.045$ meV, $\mu = 0.07$ meV the gap at $k_z = 0$ reopens, signaling the phase transition. 137

LIST OF TABLES

Table 1 – Basis set, in the angular momentum representation, for the 14-band $\mathbf{k} \cdot \mathbf{p}$ model. We denote the antibonding s and p orbitals as $\Gamma_i^c, i = 6, 7, 8$ and the bonding p orbitals $\Gamma_i^v, i = 7, 8$	54
Table 2 – Basis set, in the quasi-angular momentum representation, for the 8-band wurtzite $\mathbf{k} \cdot \mathbf{p}$ model.	63
Table 3 – Linear, ΔS_L , and cubic, ΔS_C , spin-splitting coefficients of the total Hamiltonian for the first subband of zinc-blende and wurtzite nanowires. Here we use the Rashba parameter $\alpha_R = \langle \alpha_{\text{ele},R}^0 \rangle + \langle \alpha_{\text{bm},R}^0 \rangle$. Since WZ $[11\bar{2}0]$ and $[10\bar{1}0]$ have the same contribution we just use one label to address it, namely WZ $[11\bar{2}0]$	84
Table 4 – Zinc-blende InSb $\mathbf{k} \cdot \mathbf{p}$ parameters.	93
Table 5 – WZ InAs $\mathbf{k} \cdot \mathbf{p}$ parameters.	94
Table 6 – Bulk g-factor for wurtzite InAs.	96

CONTENTS

1	INTRODUCTION	29
2	THEORY	41
2.1	The effective mass equations	41
2.1.1	$k \cdot p$ method: Introduction	41
2.1.2	$k \cdot p$ method: a more general case	44
2.1.3	$k \cdot p$ method: envelope function approximation	45
2.2	Time reversal symmetry - Intermission	47
2.3	Landè g-factor	50
2.3.1	One-band model	50
2.3.2	Degenerate bands	51
2.4	Bulk $k \cdot p$ matrices	52
2.4.1	Extended Kane model	53
2.4.1.1	[110] direction	57
2.4.1.2	[111] direction	60
2.4.2	Wurtzite model	62
2.4.2.1	$[11\bar{2}0]$ and $[10\bar{1}0]$ directions	66
2.5	Plane wave expansion	70
2.5.1	g-factor in the envelope function approximation and plane wave expansion	73
2.5.1.1	$\vec{\pi}$ matrix element	76
2.6	Effective spin-orbit coupling model	78
2.6.1	Zinc-blende BIA fields	79
2.6.2	Wurtzite BIA fields	80
2.6.3	Effective Hamiltonian and dispersion relation	81
2.7	Superconductor proximity effects	85
2.7.1	Bogoliubov-de-Gennes (BdG) formalism	86
2.7.1.1	s-wave superconductors	88
2.7.1.2	p-wave superconductors in one dimension	88
2.7.2	Proximity effects on $k \cdot p$ Hamiltonians	89

3	RESULTS	91
3.1	System setup	91
3.2	g-factor	94
3.3	Spin-orbit coupling	101
3.3.1	Zinc-blend InSb nanowires	102
3.3.1.1	[001] oriented nanowires	103
3.3.1.2	[110] oriented nanowires	105
3.3.1.3	[111] oriented nanowires	110
3.3.1.4	Discussion	115
3.3.2	Wurtzite InAs nanowires	119
3.3.2.1	[0001] oriented nanowires	120
3.3.2.2	$[10\bar{1}0]$ and $[11\bar{2}0]$ oriented nanowires	123
3.3.2.3	Discussion	127
3.4	Superconductor proximity effects	132
4	CONCLUSION	139
4.1	Future activities and projects	141
	REFERENCES	143

1 INTRODUCTION

Low dimensional semiconductor systems such as quantum wells, wires and dots present distinct optical and electronic properties in contrast with their bulk counterpart. This dimensionality dependence may be seen in the anisotropy of the polarization spectrum of a nanowire¹ or in the anisotropy of the g-factor in quantum wells²⁻⁵ as well as in the quantized conductance (quantum Hall effect), or more recently, the quantum spin Hall effect⁶⁻⁸ and also in many more effects. The knowledge acquired when we understand these phenomena walks hand-in-hand with possible breakthroughs in technological applications. The spin control (or spintronics)⁹ in nanostructures is an example where a fundamental phenomenon is explored to implement unique devices in its functions, such as the integration of memory and logic using the spin quantum Hall effect^{10,11} or using carbon nanotubes,¹² or the use of spin polarization to increase laser efficiency.¹³⁻¹⁵

Recently, the field of spintronic got fueled again with the re-interpretation of the quantum spin Hall effect,⁷ where the spin-orbit interaction generates surface spin-polarized currents going in opposite directions thus creating a transverse spin-polarized (helical) current even without a magnetic field.^{16,17} Before the quantum spin Hall effect, the integer Hall effect was known to support topologically protected edge states. In this case, however, the topological transition was driven by an external magnetic field in opposition to the, internal, spin-orbit interaction in the quantum spin Hall effect.¹⁸ The interpretation of the quantum spin Hall effect as a topological phase transition lead us to the topological insulator era. A topological insulator is a material with conducting surfaces states protected by time reversal symmetry and particle number conservation.¹⁹⁻²² It was predicted back in 1987²³ that symmetry protected edge states could occur in quantum wells with inverted gap (such as HgTe/CdTe or InAs/GaSb) and first observed experimentally in 2007.²⁴ This symmetry protection arises from spin-orbit coupling that, in special conditions, robustly locks the spin with the momentum, even when scattering occurs. With the attention gained, this field thrived, our understanding of new topological phases of matter enhanced and new applications were proposed like the latest rechargeable spin battery.²⁵ More in-depth understanding of topological insulators may be found in the reviews in Ref. 16 and Ref. 17.

In common insulators, here we include typical bulk semiconductors and heterostruc-

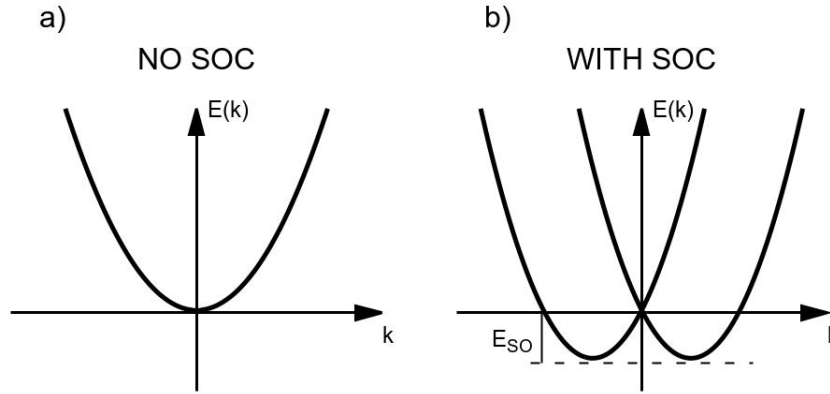


Figure 1: Effect of the spin-orbit coupling in a crystal without inversion symmetry, either bulk or structural. a) Degenerate bands without spin-orbit coupling and b) spin split bands, with visual representation of the spin-orbit coupling energy, E_{SO} .

Source: By the author.

tures, the electrons have a parabolic energy dispersion relation near some high symmetry point, see Fig. 1a). On the other hand in systems where there is a topological phase transition we have a gapless linear dispersion in the band crossing point. This linear energy dispersion characterizes the electrons as massless Dirac fermions, because it resembles the light cone. Using the very fact that topological insulators could be described by the Dirac equation Fu & Kane²⁶ proposed that if superconducting pairing was induced in such systems they could support zero-energy Majorana bound states. Proposed by Ettore Majorana in 1937²⁷ (see Fig. 2) the Majorana fermions are solutions of the Dirac equation which describe a neutral spin- $\frac{1}{2}$ particle indistinguishable from its anti-particle. There is no doubt that these Majorana fermions should exist, but the open question is whether the zero-energy Majorana bound states exists or not.²⁸

Since the zero-energy Majorana bound states have the peculiar property that they are both the particle and the anti-particle they require special conditions to arise, i. e., they should be neutral and spinless quasi-particles. In principle, any fermion can be seen as a superposition of two zero-energy Majorana fermions, so strictly speaking the Majoranas should be seen as ‘half’ of a regular fermion. These aforementioned requirements constrains our search space in condensed matter systems: i) in metals, electrons and holes could be seen as candidates because they can annihilate themselves to create other fermionic excitations but they carry opposite charges; ii) in superconductor, on the other hand, the Cooper-pairs could also be seen as candidates since they violate the charge conservation

but the electrons condensate via the s-wave pairing, meaning that the Cooper-pairs are composed by electrons with the same spin. Hence, to create neutral and spinless quasi-particles, one would need an odd superconducting pairing called p-wave.²⁹



Figure 2: Bust of Ettore Majorana at Sapienza University of Rome.

Source: Photo taken by P. E. Faria Junior.

These zero-energy Majorana bound states, if proven to exist, can revolutionize the quantum computing field because they have non-Abelian exchange statistics. This means that one could use the Majorana fermions as qubits, encoding information and performing computation, in a fault-proof fashion.^{30,31} In 2010 [Sau et al.](#)³² proposed to switch the topological insulator by a regular semiconductor heterostructure with strong spin-orbit coupling. Provided that time-reversal symmetry was broken by a magnetic insulator and that s-wave superconductivity was induced, he showed that a zero-energy Majorana bound state could exist in this configuration. Following his idea, [Alicea](#)³³ also proposed to switch the topological insulator by a semiconductor heterostructure but now breaking the time-reversal symmetry by applying an in-plane magnetic field. Both ideas are based on the fact that when s-wave superconductivity is induced in the semiconductor heterostructure, due to the spin-orbit coupling, there appears an effective p-wave pairing

that couples spinless (or fully spin-polarized) particles.

Strong spin-orbit coupling is a requirement because it gives a linear energy dispersion (Dirac like behavior) to the spin-split energy bands at small momenta, see Fig. 1b). The presence of a magnetic interaction through the Zeeman splitting effectively opens a gap making the spin-split bands no longer cross each other, and when the chemical potential lies inside the Zeeman gap we have a single Fermi surface with spinless (or fully spin-polarized electrons) that resembles the Kitaev chain.^{30,34,35} Early experiments with InSb^{36,37} and InAs³⁸ nanowires highlighted the existence of the main signature of the presence of zero-energy Majorana bound states, which is a peak at zero bias in the conductance. Nevertheless, there are other mechanisms that could give this same peak, such as the Kondo effect,³⁹ disorder^{40,41} and more.^{42–45} Hence, the confirmation of the existence of the zero-energy Majorana bound states in semiconductor-superconductor hybrid devices is questionable^{46–48} and new proposals to enhance the measurements have already been made.^{49–52} Moreover, very recently He et al.⁵³ reported that they found that quantum anomalous Hall insulator-superconductor hybrid structures can host the zero-energy Majorana modes.

The spin-orbit coupling in semiconductors arises from two distinct sources: the bulk inversion asymmetry, known as BIA,⁵⁴ and the structural inversion asymmetry, known as SIA.⁵⁵ The first mechanism is present in materials whose unit cell does not possess inversion symmetry, i.e., if the base is composed by two different atoms. Therefore, the crystal is defined as non-centro-symmetric. The second mechanism appears when the system is submitted to an external asymmetric potential, usually an electric potential; or even the very heterostructure is composed by materials with distinct widths (making an asymmetric quantum well, for instance). Note that both spin-orbit couplings arise from the breaking of spatial inversion symmetry either at the microscopic or the macroscopic levels. Under the spin-orbit coupling, the allowed states of a nanostructure can be characterized by their spin texture, i.e., a specific spin configuration, which is crucial to application development. It is known that certain spin textures provide a very long carrier life time due to the suppression of certain spin relaxation mechanisms.

In particular, the magnitudes of the BIA and SIA spin-orbit coupling can be fine-tuned to obtain interesting properties. In quantum well heterostructures, the SIA effect can be controlled via the doping profile or via an external gate induced potential bias,

as well as by constructing asymmetric heterostructures. The BIA, however, is mainly controlled by quantum confinement and by the doping density. The interplay between BIA and SIA mechanisms opened a vast field of interest in spintronics. For example, when the strengths of both mechanisms are tuned to be equal, the spin texture assumes a configuration that is persistent (or independent) of the momentum, making the states robust against spin-flip process. This phenomena is known as persistent spin helix.^{56,57} This configuration allows non-ballistic spin transistors,⁵⁸ because one knows exactly the spin orientation at each momenta, contrary to the original Datta-Das⁵⁹ spin transistor proposal, where only the SIA mechanism was taken into account leading to a momentum dependent spin polarization, susceptible to scattering process which randomizes the spin orientation. Moreover, the control of the spin polarization and of the density of spin polarized carriers allow more efficient devices such as the spin lasers. Due to the spin-orbit coupling, the spin polarized carriers injected in the active region of the laser keep their polarization enabling distinct optical transitions (which leads to distinct lasing thresholds). The transitions emits light with specific polarization (circularly polarized to the right or left). Therefore, the spin control in lasers allows light with a high degree of polarization and low energy consumption and, by consequence, an efficient operation.^{14,15}

Experimentally, reliable determination of the spin-orbit coupling strength in nanowires is a challenging task.⁶⁰ Nevertheless, it has been investigated in a variety of distinct setups^{61,62} each one leading to different values for the spin-orbit coupling strength. For example, experiments of magnetoconductance in the anti localization regime provides us with a variety of values for the spin-orbit coupling strengths for the same material.^{37,63–65} These values are obtained by carefully engineering the experimental setup, such as the placement of the electrodes and the gating tuned to break the structural symmetry of the system, leading to large spin-orbit coupling parameters.⁵⁵ To theoretically investigate the spin-orbit coupling, it is common to use reduced models for the semiconductor conduction band.^{9,55,66,67} In these models, the spin-orbit coupling enters as an empirical parameter that can assume a wide range of values for the same system depending on the measurement setup.^{62,68,69} Hence, it is important to devise a theoretical method in which the spin-orbit coupling parameters can be reliable and precisely determined for different nanowire configurations.

A complete separate field of research on its own is the superconductivity. When

metals are cooled below a critical temperature it undergoes a phase transition where its resistivity goes to zero, i. e., a current flowing through a superconductor wire can persist indefinitely with no power source. Is not my intention to explore in depth the details of superconductivity, but I wish to make clear some basic concepts that I will use in my thesis. The complete microscopic theory was proposed by [Bardeen, Cooper & Schrieffer](#)⁷⁰ in 1957 and it is known as the BCS theory. The theory explains the superconductivity as a superfluid made of pairs of electrons, the Cooper pairs, interacting through exchange of phonons.⁷⁰ In short, they considered only the electrons on the Fermi surface and replaced the interaction between electrons and phonons by an attractive interaction between electrons resulting in a coupling only between electrons with opposite momenta. In the next year, 1958, [Bogoljubov, Tolmachov & Širkov](#)⁷¹ proposed a more general solution to the problem where they used a canonical transformation, based on the idea that particles with opposite momenta form bound pairs, and found that the solution first proposed by [Bardeen, Cooper & Schrieffer](#)⁷⁰ was correct in first order in their new formulation. When a superconductor is placed in contact with a normal non-superconductor metal the superconductivity is induced, through what we call proximity effect, to the normal metal. It is known that in the metal the electrons are described by plane waves without any ordering whatsoever, whereas in the superconductor the electrons are in an ordered state, the Cooper pairs. Therefore, in the junction the electron ordering in one system cannot abruptly change in the other. Instead, the paired state in the superconducting metal is carried over to the normal metal, where it loses its ordering up to a typical penetration length. Conversely, the electrons of the metal are also carried over to the superconductor lowering the superconductor gap near the interface. The microscopic theory describing this phenomena is the Andreev reflection.⁷²

One of the key ingredients in the hybrid semiconductor-superconductor setup is the magnetic field. The criteria for the system to undergo a topological transition and, therefore, host the Majorana bound states is that $V_Z > \sqrt{\Delta_{SC}^2 + \mu^2}$.^{29,32-35,48,73} In principle this could be achieved by increasing the magnetic field strength but not without losing the superconductor properties. A way around, is to use semiconductors with high g-factor values, so with a small enough magnetic field, one could get larger Zeeman splittings without breaking the superconductor behavior. For zinc-blende semiconductors the conduction band g-factor has a compact expression due to [Roth, Lax & Zwerdling](#)⁷⁴

where its values are related to the material's gap, the spin-orbit coupling splitting and the interband coupling. For wurtzite, the g-factor expression, see Ref. 75, is not as simple as in the zinc-blende, nevertheless, it is also possible to relate the value of the g-factor to the gap, spin-orbit splitting and interband couplings.

The g-factor is an important and active research topic both theoretically^{4,76–87} and experimentally.^{2,3,5,88–92} It is known that quantum confinement and spin-orbit coupling heavily affect the g-factor with a renormalization of its value as well as generating an anisotropy, i. e., a non-zero difference between its values parallel and perpendicular to the applied magnetic field.⁴ For free electrons, the g-factor has a very well established value, $g_0 = 2.0023$, but in bulk semiconductors, due to the gap renormalization and spin-orbit interaction, it varies from $g^* = 1.26$ for InP to $g^* = -51$ for InSb and also can have values very close to zero, such as $g^* = -0.44$ for GaAs.⁷⁵ Therefore, by combining distinct materials in a quantum well heterostructure one can engineer the g-factor to obtain a desired value, or even achieve a $g^* = 0$.^{4,76,80} Moreover, in quantum wells, the electrons are free to move in the plane perpendicular to the confinement but their motion strongly depends on the confinement. Thus, both BIA and SIA spin-orbit coupling can affect the g-factor, making them anisotropic.^{4,78,85} Another nanostructure system in which the g-factor has been vastly studied is the quantum dot.^{77,79,84,88,89,92,93} In these structures, the motion of the electrons is confined in all three spatial directions thus, the energy levels are discrete and resemble the energy levels of atoms. The high quantum confinement and the fact that the states are a combination of both, the spin and the orbital degrees of freedom, allow a great control of the spins via external gates⁹⁴ as well as by fabrication engineering (shape, surrounding barriers and etching) i. e., influencing the intrinsic spin orbit coupling mechanisms.^{79,84,89}

On one hand, we have seen that quantum wells and dots have a vast literature regarding the g-factor. On the other hand, although there are some studies^{95–98} on free-standing nanowires, there still lacks an in-depth theoretical and experimental investigation because most of the studies regards electrically defined quantum dots in a nanowire.^{83,88,89,93,99} Electric measurements of the g-factor requires electrodes to be deposited into the sample creating a electrically defined quantum dot in the nanowire. Theoretically, the calculation of the g-factor tensor can be carried out by reduced models focusing on the lowest conduction subband only^{96–98} or by more robust methods that take into account the interaction with

remote bands as well as the geometry of the nanowire from the beginning.^{77,79,100} The multiband $\mathbf{k} \cdot \mathbf{p}$ method belongs the former case, in which with low enough computational cost, one can compute the electronic band structure as well as the wave functions of any low dimensional semiconductor nanostructures and with them compute the properties such as effective masses, g-factors and spin-splittings.

Besides the $\mathbf{k} \cdot \mathbf{p}$ method, there are other methods to study the properties of semiconductor nanostructures such as: first-principles methods based on the density functional theory^{101,102} or phenomenological approaches based on the tight-binding method.^{103–105} Each class of method has its own pros and cons. First-principles methods require minimum input from external sources because they are based on the fundamental laws of physics. It takes the atoms' position as input and applying principles of quantum mechanics, statistical physics and electromagnetism it is able compute a series of properties including the electronic band structure. For bulk systems, were with only a few atoms one describes the unit cell, first-principles methods are the most reliable and accurate method and are very successful in determining properties of novel systems such as the III-V compounds in the wurtzite crystal phase^{106–109} and also of 2D materials.^{110–113} However, for confined system, where thousands of atoms are required to describe the system, its computational cost becomes prohibitive. The tight-binding method is also atomistic but the system's description is based on atomic orbital overlap parameters that are usually obtained from first-principles calculations. Although it provides a very nice physical picture (or intuition) of the interacting orbitals, the resulting Hamiltonian can be quite large. Nevertheless, tight-binding is widely used in condensed matter physics in special to study III-V low dimensional nanostructures^{114–116} and also 2D materials.^{117,118}

The $\mathbf{k} \cdot \mathbf{p}$ method applies a different approach to determine physical properties of semiconductor nanostructures. Like the first-principles methods it uses the information of only a few atoms comprising the unit cell to determine its basis set, as periodic functions given by Bloch's theorem. Like the tight-binding method it relies on parameters (matrix elements among the basis set defined by the symmetries of the system) that have to be obtained by external sources, which are usually first-principles calculations or experimental measurements.¹¹⁹ Unlike both first-principles and tight-binding, the $\mathbf{k} \cdot \mathbf{p}$ method uses a continuum description of the system and it is based on a perturbative approach for the energy bands around a high-symmetry point of the Brillouin zone.^{120–122} One defines the

core set of energy bands to be used in the system's description and includes the effects of all the other bands as a perturbation. The interaction of the core set of energy bands with the remote ones gives rise to the effective mass (a renormalization of the particle's mass) as a second order correction,¹²³ and the explicit coupling between the bands in the core set is given by the optical matrix element, also known as the Kane matrix element.¹²⁴ The main advantage of the $\mathbf{k} \cdot \mathbf{p}$ method over the other methods is the description of confined systems via the envelope function approximation.^{125–128} Since it is a continuum method in the reciprocal space based on momentum operators, to treat confined systems one substitutes the momentum operator, \vec{k} , by the derivative operator, $-i\vec{\nabla}$.

The $\mathbf{k} \cdot \mathbf{p}$ method in all its variants has been applied over the years to successfully study a wide range of semiconductor systems and properties. Here we like to emphasize a few that are related to the present work developed in this Thesis. In the field of spintronics it has been used to further clarify the role of the spin-orbit coupling effects in low dimensional semiconductor nanostructures,^{82,83,100,129–136} its relation to the anisotropy of the g-factor,^{4,76–78,81,85} as well as the study of novel phases of the matter such as topological insulators^{7,137,138} and the elusive Majorana fermion.⁷³

Motivated by hybrid semiconductor-superconductor proposal to search for the zero-energy Majorana bound states, that uses semiconductor nanowires with high spin-orbit coupling, we, in this study, investigate the role of the BIA and SIA spin-orbit couplings in zinc-blende InSb and wurtzite InAs free-standing nanowires. In particular, we want to access theoretically how the quantum confinement, given by the nanowire diameter, and the orientation of the nanowire (growth direction) modifies the two main parameters that define if the system can (or cannot) host these zero-energy excitations: the spin-orbit coupling energy and the g-factors. We analyzed nanowires with hexagonal cross section in three different growth directions: [001], [110] and [111] for zinc-blende; [0001] (c-plane), [11 $\bar{2}$ 0] (a-plane) and [10 $\bar{1}$ 0] (m-plane) for wurtzite.^{139–142} Furthermore, we used realistic multiband $\mathbf{k} \cdot \mathbf{p}$ models, namely: 14-band Kane model^{67,132,143} to treat zinc-blende InSb nanowires; and 8-band model¹⁴⁴ to treat wurtzite InAs nanowires under the envelope function approximation and plane wave expansion. The BIA spin-orbit coupling for zinc-blende is taken into consideration with the addition of the extra conduction bands and their explicit coupling parameters; whereas in the wurtzite case, it is taken care, by the addition of the often neglected^{108,145–152} linear in momentum spin-orbit coupling term

in the 8-band model. Moreover, the SIA spin-orbit coupling arises by the breaking of structural symmetry when we apply an external electric field. Due to the realistic nature of our model, we can verify the application limits of the SIA spin-orbit coupling, known as Rashba model, which is carelessly used in many effective models for a wide range of applied electric fields.

We have calculated nanowires with diameter ranging from $L = 30$ nm to $L = 100$ nm and applied electric fields, along x and y directions, ranging from $E = -4$ mV/nm to $E = 4$ mV/nm. Focusing on the first conduction subband, we derived compact analytical expressions for the BIA spin-orbit coupling Hamiltonian for both crystal phases and all nanowire orientations based on symmetry considerations. Furthermore, applying a numerical fitting method to the calculated subband dispersion, we extracted pertinent parameters to describe the first conduction subband with a phenomenological two-band Hamiltonian. With this simple model and fitted parameters, we analyze the interplay between BIA and SIA spin-orbit mechanisms and calculated the spin-orbit coupling energy. Also, using perturbation theory, we were able to calculate the g-factor tensor and assess how the spin-orbit coupling provides its anisotropies, both in- and out-of-plane. Moreover, to provide realistic predictions on whether the nanowires could host the zero-energy excitations or not, using the fitted parameters and the calculated g-factors, we applied the BdG formalism and verified if our system could undergo the required topological transition.

We found that the BIA spin-orbit coupling in the first conduction subband of zinc-blende nanowires oriented along $[001]$ and $[111]$ direction has a linear in momentum functional form, in contrast to the cubic in momentum dependence of their bulk counterparts, whereas $[110]$ oriented nanowires still maintain the cubic dependence (and all other odd powers of the momentum). The BIA also gives a particular spin orientation: it orients the spin along the z direction for $[001]$ nanowires and along the y direction for both $[110]$ and $[111]$ oriented nanowires. Moreover, for wurtzite nanowires we found that the BIA is absent from the first conduction subband on $[0001]$ oriented nanowires, whereas for $[10\bar{1}0]$ or $[11\bar{2}0]$ oriented nanowires it presents linear and cubic functional forms that resemble the bulk contributions and provides a spin orientation along the y direction. Furthermore, for zinc-blende nanowires the BIA is heavily influenced by the quantum confinement. On the other hand, wurtzite has a dominant linear in momentum

bulk BIA contribution that is kept constant even in the presence of quantum confinement.

By applying an electric field transverse to the nanowire we, besides breaking the structural symmetry, generate an extra quantum confinement that lifts the energy levels and can break the orbital degeneracy. With the symmetry breaking there appears the SIA spin-orbit coupling that further splits the energy bands for a generic wave vector. The model describing the SIA spin-orbit coupling is the Rashba model, given simply by $H_R = \alpha_0 \vec{\sigma} \cdot \vec{k} \times \vec{E}$. This model has a linear dependence both on the momentum and on the applied electric field. We found that in general this simpler linear model does not always hold and due to the multiband nature of our model Hamiltonian we saw a deviance from the linearity dependence on the momentum and, specially, for high values of applied potential a further deviation from the linear dependence on \vec{E} . Furthermore, for zinc-blende InSb nanowire the SIA is dominant over the BIA for all orientations. For wurtzite InAs, however, we found that for [0001] oriented nanowires (where the BIA is absent) the Rashba coefficient is rather small, compared with the zinc-blende. Therefore, for $[10\bar{1}0]$ or $[11\bar{2}0]$ the BIA, which is already large in the bulk, dominates over the SIA.

We also have calculated the g-factor tensor for the lowest conduction subband and we found that their values have a large dependence on the quantum confinement. For instance, the well known bulk g-factor for zinc-blende InSb is $g \approx -51$ in all three Cartesian directions. We found that for $L = 30$ nm in diameter InSb nanowires $g^* \approx -25$ reaching values of the order of $g^* \approx -42$ for $L = 100$ nm in diameter. For wurtzite InAs nanowires the bulk g-factor already are distinct for the three cartesian directions, and the confinement enhances this anisotropy. For instance, InAs nanowires oriented along [0001] direction have an in-plane g-factor between $g_{x,y}^* = -5.7$ and -6.4 and the out of plane varies from $g_z^* \approx -5$ to -10 in the same range of diameters considered above. On the other hand, $[10\bar{1}0]$ or $[11\bar{2}0]$ oriented nanowires have $g^x = -4$ to -10 , $g^y \approx -5$ on average and $g_z^* \approx -5$ to -7 . Since we used the multiband $\mathbf{k} \cdot \mathbf{p}$ model, we were able to also calculate the in-plane anisotropy due to both quantum confinement and spin-orbit coupling. We found that zinc-blende InSb oriented along [111] have the largest in-plane anisotropy. For wurtzite [0001] oriented nanowires we saw practically no anisotropy while for $[10\bar{1}0]$ or $[11\bar{2}0]$ oriented nanowires there is a large in-plane anisotropy.

Applying the BdG formalism we found that with the realistic parameters obtained for the first conduction subband and with experimentally measured induced pairing,^{36,38}

indeed the nanowires undergo the topological transition and can host the zero-energy Majorana modes. Furthermore, zinc-blende InSb nanowires showed a more robust gap near $k_z = 0$ due to the higher induced pairing. Nevertheless further investigation about the stability of the topological gap should be performed.²⁹

In conclusion, motivated by the hybrid semiconductor-superconductor setup to realize the zero-energy Majorana modes we apply a systematic numerical investigation using realistic $\mathbf{k} \cdot \mathbf{p}$ Hamiltonians taking into account both spin-orbit coupling mechanisms and lateral quantum confinement in experimentally achievable zinc-blend InSb and wurtzite InAs nanowire configurations. We found that in zinc-blend InSb nanowires the SIA dominates over the BIA while for wurtzite InAs nanowires BIA dominates over SIA. We also calculated the g-factor tensor and found that the quantum confinement generates a high degree of anisotropy between the in-plane/out-of-plane values. Finally, we apply the BdG formalism and confirmed that indeed, with a realistic parameter set, both crystal phases undergo the required topological transition to host the zero-energy Majorana modes. We like to emphasize that our approach is not restricted only to hexagonal nanowires of these specific materials, but instead can be used to study any kind of low dimensional semiconductor nanostructures, providing useful insights for the field of electronics and spintronics.

2 THEORY

In this chapter we go through the derivation of the effective mass equations in the context of the $\mathbf{k} \cdot \mathbf{p}$ perturbation method. We also discuss a little about time reversal symmetry and its applications in centro and non-centro symmetric systems resulting in the Kramers theorem. Based on the effective mass equations, we derive both effective mass and g-factor tensor as the symmetric and anti-symmetric component of the second order, $\vec{P} \cdot \vec{\pi}$, perturbation. We also provide the matrix form of the effective mass equations for both bulk zinc-blende and wurtzite crystal phases showing how to perform the rotations to other orientation of the wave vector. Furthermore, we discuss how from the bulk matrices we can compose heterostructures and formulate the envelope function approximation and the plane wave expansion as a way to express, and computationally solve, the electronic band structure. Moreover, we provide a simplified two band model to describe the lowest conduction subband of the nanowires taking into account both spin-orbit coupling mechanisms arising from the bulk and structural inversion asymmetries. Finally, we show how to apply the BdG formalism under the $\mathbf{k} \cdot \mathbf{p}$ perturbation method to study the proximity effects induced by a superconductor.

2.1 The effective mass equations

In this section we present a comprehensive derivation of the effective mass equations in the context of the $\mathbf{k} \cdot \mathbf{p}$ perturbation method. We start by the effective one-electron Schrödinger equation adding spin-orbit coupling and derive a set of couple differential equations that describes the electrons as a set of couple electronic bands.

2.1.1 $\mathbf{k} \cdot \mathbf{p}$ method: Introduction

Crystals are a system composed by a periodic arrangement of particles, electrons or protons, interacting with the field generated by the others. Although crystals have a many body character, we can derive a single particle Hamiltonian, through the Born-Oppenheimer approximation, where the electron is under the effect of an effective periodic potential with the same periodicity of the Bravais crystal lattice. Such Hamiltonian can

be written as

$$H = \frac{p^2}{2m_0} + V_0(\vec{r}), \quad (2.1)$$

where the first term is the electron's kinetic energy, with $\vec{p} = (-i\hbar)\nabla$, and the second, the periodic potential of the crystal. For now we neglect spin-dependent interactions.

Suppose that we know the energies, $\varepsilon_n^{(0)}$, and the Bloch functions, $b_{n,0}(\vec{r}) = \sqrt{\frac{\Omega}{V}}u_{n,0}(\vec{r})$, at the Brillouin zone center, $\vec{k} = 0$. Here, Ω is the volume of a unit cell of the crystal, V is the crystal volume, and $u_{n,0}(\vec{r})$ is a spinor with the lattice periodicity. We wish to obtain an approximate expression for the energy of a particular band, (say the j th), at a point in the Brillouin zone slightly away from $\vec{k} = 0$. Since the system is periodic we use the Bloch theorem, which states that the wave functions of the system can be separated into a function that have the periodicity of the system multiplied by a plane wave. The basis set, in the Bloch theorem, is

$$\phi_{n,\vec{k}}(\vec{r}) = \sqrt{\frac{\Omega}{V}}u_{n,0}(\vec{r})e^{i\vec{k}\cdot\vec{r}}. \quad (2.2)$$

The generalization to any other point of the Brillouin zone, is straight forward. We consider now $u_{n,\vec{k}}(\vec{r})$ and decomposed it in terms of the Bloch functions at $\vec{k} = 0$,^{123,124}

$$u_{n,\vec{k}}(\vec{r}) = \sum_{n'} c_{n'n}(\vec{k} - \vec{k}_0) u_{n',\vec{k}_0}(\vec{r}). \quad (2.3)$$

but for simplicity and without loss of generality we will consider the case where the high symmetry point we want to describe is the Γ -point, $\vec{k} = 0$.

The set of states (2.2) is the basis set for the Kohn-Luttinger representation.¹²³

Applying the Hamiltonian given by Eq. (2.1) on $\phi_{n,\vec{k}}$, we get

$$H\phi_{n,\vec{k}} = e^{i\vec{k}\cdot\vec{r}} \left(\frac{\vec{p}^2}{2m} + V_0(\vec{r}) + \frac{\hbar}{m} \vec{k} \cdot \vec{p} + \frac{\hbar^2 \vec{k}^2}{2m} \right) u_{n,0}(\vec{r}). \quad (2.4)$$

Since we suppose we know that $\left\{ \frac{\vec{p}^2}{2m} + V_0(\vec{r}) \right\} u_{n,0}(\vec{r}) = \varepsilon_n^{(0)} u_{n,0}(\vec{r})$, we have,

$$H\phi_{n,\vec{k}} = e^{i\vec{k}\cdot\vec{r}} \left(\varepsilon_n^{(0)} + \frac{\hbar}{m} \vec{k} \cdot \vec{p} + \frac{\hbar^2 \vec{k}^2}{2m} \right) u_{n,0}(\vec{r}). \quad (2.5)$$

Using the fact that, given $U(\vec{r})$, a function varying slowly over a unit cell of the lattice, and $g(\vec{r})$ is a function with the lattice periodicity, then¹²¹

$$\langle \phi_{n',\vec{k}'} | g(\vec{r})U(\vec{r}) | \phi_{n,\vec{k}} \rangle \cong g_{n',n} U_{\vec{k}',\vec{k}}, \quad (2.6)$$

where

$$g_{n',n} = \int_{\text{unitcell}} u_{n,0}^*(\vec{r}) g(\vec{r}) u_{n,0}(\vec{r}) d\tau, \quad (2.7)$$

and

$$U_{\vec{k}',\vec{k}} = \frac{1}{V} \int e^{-i\vec{k}'\cdot\vec{r}} U(\vec{r}) e^{i\vec{k}\cdot\vec{r}} d\tau. \quad (2.8)$$

the matrix element of H between two states $\phi_{n',\vec{k}'}$ and $\phi_{n,\vec{k}}$ will be diagonal in \vec{k} , and we find,

$$\langle \phi_{n',\vec{k}'} | H | \phi_{n,\vec{k}} \rangle \cong \left(\varepsilon_n^{(0)} \delta_{n',n} + \frac{\hbar}{m} \vec{k} \cdot \vec{p}_{n',n} + \frac{\hbar^2 \vec{k}^2}{2m} \delta_{n',n} \right) \delta_{\vec{k}',\vec{k}}, \quad (2.9)$$

where

$$\vec{p}_{n',n} = \int_{\text{unitcell}} u_{n',0}^* \vec{p} u_{n,0} d\tau. \quad (2.10)$$

The energy of the j th band up to the second order in perturbation theory can be obtained from Eq. (2.9) and it is,

$$\varepsilon \cong \varepsilon_j^{(0)} + \frac{\hbar^2 \vec{k}^2}{2m} + \sum_{\mu} \left(\frac{\hbar}{m} \right)^2 \frac{\vec{k} \cdot \vec{p}_{j\mu} \vec{p}_{\mu j} \cdot \vec{k}}{(\varepsilon_j^{(0)} - \varepsilon_{\mu}^{(0)})}, \quad (2.11)$$

where the sum is over all bands $\mu \neq j$. This expression can be rewritten as

$$\varepsilon = \varepsilon_j^{(0)} + \left(\frac{\hbar^2}{2} \right) \vec{k} \cdot \vec{m}_j^{-1} \cdot \vec{k}, \quad (2.12)$$

where \vec{m}_j^{-1} is an inverse mass tensor given by

$$\vec{m}_j^{-1} = \frac{1}{m} \vec{I} + \frac{2}{m} \sum_{\mu} \frac{\vec{p}_{j\mu} \vec{p}_{\mu j}}{(\varepsilon_j^{(0)} - \varepsilon_{\mu}^{(0)})}. \quad (2.13)$$

The present discussion states the simplicity of the effective mass equations and serve as a starting point to understand the more complex problem of several coupled and nearly degenerate bands in the presence of external potentials. The presence of the term $\vec{k} \cdot \vec{p}_{n',n}$, in Eq. (2.9), gives the name to the method.

2.1.2 $\mathbf{k} \cdot \mathbf{p}$ method: a more general case

In this subsection, we will look into a more general case for effective mass equations.

We consider the one-electron Hamiltonian

$$H = \frac{1}{2m} (\vec{p} + e\vec{A})^2 + g\mu_B \vec{S} \cdot \vec{B} - eV_0(\vec{r}) - eV(\vec{r}) + \frac{\hbar}{4m_0^2 c^2} [\vec{\nabla} (V + V_0) \times (\vec{p} + e\vec{A})] \cdot \vec{S}, \quad (2.14)$$

where we made use of the minimal coupling: $\vec{p} \rightarrow \vec{p} + e\vec{A}$, with \vec{A} being the vector potential $\vec{B}(\vec{r}) = \vec{\nabla} \times \vec{A}$. In the Hamiltonian above we have a description of an electron with orbital and spin interactions with an uniform external magnetic field described by the vector potential, the Zeeman splitting, and a perturbing potential $V(\vec{r})$.

We consider the unperturbed Hamiltonian as

$$H_0 = \frac{\vec{p}^2}{2m} + \frac{\hbar}{4m_0^2 c^2} (\nabla V_0 \times \vec{p}) \cdot \vec{S} - eV_0(\vec{r}), \quad (2.15)$$

including the spin-orbit coupling, since spin-orbit splittings of many bands are comparable to the band gaps. We use the set of states (2.2) as our wave functions to compute the action of the Hamiltonian (2.14). Operating (2.14) on (2.2), gives

$$\begin{aligned} H\phi_{n,\vec{k}} &= \left(\sqrt{\frac{\Omega}{V}} \right) \left[e^{i\vec{k}\cdot\vec{r}} \left\{ \left(\frac{\vec{p}^2}{2m} - eV_0(\vec{r}) + \frac{\hbar}{4m^2 c^2} \nabla V_0 \times \vec{p} \cdot \vec{S} \right) u_{n,0} \right\} \right. \\ &\quad + \left\{ \frac{1}{2m} \left(\vec{p} + \frac{e}{c} \vec{A} \right)^2 e^{i\vec{k}\cdot\vec{r}} \right\} u_{n,0} + \left\{ \left(\vec{p} + \frac{e}{c} \vec{A} \right) e^{i\vec{k}\cdot\vec{r}} \right\} \\ &\quad \times \left\{ \left(\frac{\vec{p}}{m} + \frac{\hbar}{4m^2 c^2} \nabla V_0 \times \vec{S} \right) u_{n,0} \right\} \\ &\quad \left. + \left(g\mu_B \vec{S} \cdot \vec{B} - eV(\vec{r}) + \frac{\hbar}{4m^2 c^2} \nabla V \times \vec{p} \cdot \vec{S} \right) e^{i\vec{k}\cdot\vec{r}} u_{n,0} \right] \end{aligned} \quad (2.16)$$

where we are for the moment using the convention that operator act only inside $\{\}$. Since we know the energies of the unperturbed problem, Eq. (2.16) becomes

$$\begin{aligned} H\phi_{n,\vec{k}} &= \left(\sqrt{\frac{\Omega}{V}} \right) \left[\varepsilon_n^{(0)} e^{i\vec{k}\cdot\vec{r}} u_{n,0} + \left\{ \frac{1}{2m} \vec{P}^2 e^{i\vec{k}\cdot\vec{r}} \right\} u_{n,0} \right. \\ &\quad + \left\{ \vec{P} e^{i\vec{k}\cdot\vec{r}} \right\} \cdot \{ \vec{\pi} u_{n,0} \} \\ &\quad \left. + \left(g\mu_B \vec{S} \cdot \vec{B} - eV(\vec{r}) + \frac{\hbar}{4m^2 c^2} \nabla V \times \vec{p} \cdot \vec{S} \right) e^{i\vec{k}\cdot\vec{r}} u_{n,0} \right] \end{aligned} \quad (2.17)$$

where $\vec{P} = \vec{p} + e\vec{A}$ and $\vec{\pi} = \frac{\vec{p}}{m} + \frac{\hbar}{4m^2c^2} \nabla V_0 \times \vec{S}$.

We now multiply Eq. (2.17) on the left by $\phi_{n',\vec{k}'}^*$ and integrate to obtain the matrix element $\langle \phi_{n',\vec{k}'} | H | \phi_{n,\vec{k}} \rangle$.

$$\langle \phi_{n',\vec{k}'} | H | \phi_{n,\vec{k}} \rangle = \varepsilon_n^{(0)} \delta_{n',n} \delta_{\vec{k}',\vec{k}} + \langle \phi_{n',\vec{k}'} | H_1 | \phi_{n,\vec{k}} \rangle, \quad (2.18)$$

where

$$\begin{aligned} \langle \phi_{n',\vec{k}'} | H_1 | \phi_{n,\vec{k}} \rangle &= \frac{(\vec{P}^2)_{\vec{k}',\vec{k}}}{2m} \delta_{n',n} + \vec{P}_{\vec{k}',\vec{k}} \cdot \vec{\pi}_{n',n} + g\mu_B \vec{S}_{n',n} \cdot \vec{B} \delta_{\vec{k}',\vec{k}} \\ &\quad - eV_{\vec{k}',\vec{k}} \delta_{n',n} + \frac{\hbar}{4m^2c^2} (\nabla V \times \vec{p})_{\vec{k}',\vec{k}} \cdot \vec{S}_{n',n}. \end{aligned} \quad (2.19)$$

The matrix element of \vec{S} appears in Eq. (2.19) since the function $u_{n',0}(\vec{r})$ and $u_{n,0}(\vec{r})$ are explicit functions of spin with the spin-orbit interaction included in the zeroth order problem.

To carry on the perturbation theory one has to realize that, in general, the energy bands will have degenerescence. Therefore, one has to use the quasi-degenerate perturbation theory or, also called, Löwdin partitioning.^{120,123,132} Conventional stationary and quasi-degenerate perturbation theory are similar, but the latter is more powerful due to the fact that one does not need to distinguish between nondegenerate and degenerate perturbation theory.

We assume that we can divide the set of eigenfunctions $\{\phi_n\}$ into two weakly interaction subsets A and B. The set A is defined as $\{\phi_\alpha\}$ and the set B as $\{\phi_\beta\}$. Also, $\{\phi_\alpha\} \cap \{\phi_\beta\} \equiv \{0\}$ and $\{\phi_\alpha\} \cup \{\phi_\beta\} \equiv \{\phi_n\}$. The goal is to construct a transformed Hamiltonian, $\tilde{H} = e^{-S} H e^S$, such that matrix elements $\langle \phi_\alpha | \tilde{H} | \phi_\beta \rangle$ vanish up to a desired order of H_1 . Details of the calculation are omitted in this Thesis but can be found in Ref. 132. In other words, we project the effects of remote bands onto the set A.

2.1.3 $\mathbf{k} \cdot \mathbf{p}$ method: envelope function approximation

The final goal is to have an eigenvalue/eigenstate equation that when applied to some wave function, gives us the energies and wave functions of our desired problem, such as $H_0 \phi_{n,\vec{k}} = \varepsilon_{n,\vec{k}} \phi_{n,\vec{k}}$. This is not always possible. Nevertheless, the functions $\phi_{n,\vec{k}}$ form a

complete set in which we can expand a general wave function ψ as $\psi = \sum_{n,\vec{k}(B.Z.)} A_n(\vec{k}) \phi_{n,\vec{k}}$, where the sum over \vec{k} is over the first Brillouin zone.

Proceeding with the Löwdin partitioning we obtain,

$$\sum_{j,\vec{k}} \left[\langle \phi_{l,\vec{k}'} | H_{\text{eff}} | \phi_{j,\vec{k}} \rangle - \varepsilon \delta_{lj} \right] A_j(\vec{k}) = 0, \quad (2.20)$$

where

$$\langle \phi_{l,\vec{k}'} | H_{\text{eff}} | \phi_{j,\vec{k}} \rangle = \varepsilon_l^{(0)} \delta_{l,j} \delta_{\vec{k}',\vec{k}} + \langle \phi_{l,\vec{k}'} | H_1 | \phi_{j,\vec{k}} \rangle + \sum_{\mu,\vec{k}''} \frac{\langle \phi_{l,\vec{k}'} | H_1 | \phi_{\mu,\vec{k}''} \rangle \langle \phi_{\mu,\vec{k}''} | H_1 | \phi_{j,\vec{k}} \rangle}{(\varepsilon - \varepsilon_\mu^{(0)})} + \dots \quad (2.21)$$

We can simplify the expression to

$$\langle \phi_{l,\vec{k}'} | H_{\text{eff}} | \phi_{j,\vec{k}} \rangle = \varepsilon_l^{(0)} \delta_{l,j} \delta_{\vec{k}',\vec{k}} + \left((H_{1\text{eff}})_{lj} \right)_{\vec{k},\vec{k}'}, \quad (2.22)$$

where

$$(H_{1\text{eff}})_{lj} = \left\{ H_{1lj} + \sum_{\mu} \frac{H_{1l\mu} H_{1\mu j}}{(\varepsilon - \varepsilon_\mu^{(0)})} + \sum_{\mu,\nu} \frac{H_{1l\mu} H_{1\mu\nu} H_{1\nu j}}{(\varepsilon - \varepsilon_\mu^{(0)}) (\varepsilon - \varepsilon_\nu^{(0)})} + \dots \right\}, \quad (2.23)$$

with

$$H_{1n'n} = \frac{\vec{P}^2}{2m} \delta_{n',n} + \vec{P} \cdot \vec{\pi}_{n',n} + g\mu_B \vec{S}_{n',n} \cdot \vec{B} - eV(\vec{r}) \delta_{n',n} = \frac{\hbar}{4m^2 c^2} (\nabla V \times \vec{p}) \cdot \vec{S}_{n',n}. \quad (2.24)$$

Multiplying eq. (2.20) on the left with $e^{i\vec{k}' \cdot \vec{r}} / \sqrt{V}$ and summing over \vec{k}' , we obtain

$$\sum_j \left[(H_{\text{eff}})_{lj} - \varepsilon \delta_{lj} \right] f_j(\vec{r}) = 0, \quad (2.25)$$

which are the effective mass equations in real space, with $(H_{\text{eff}})_{lj} = \varepsilon_l^{(0)} \delta_{lj} + (H_{1\text{eff}})_{lj}$.

Here,

$$f_j(\vec{r}) = \sum_{\vec{k}} \frac{1}{\sqrt{V}} A_j(\vec{k}) e^{i\vec{k} \cdot \vec{r}}, \quad (2.26)$$

are the slowly varying functions, called envelope functions. ^{125–128}

In this derivation, the envelope functions appeared because we cannot write an analytical expression that describes the motion of an electron in the presence of some

external potential and we expanded the general wave function, ψ , as a combination of the Kohn-Luttinger functions, $\phi_{n,\vec{k}}$, which forms a complete basis states of our unperturbed system. Consider, for example, the case of a heterostructure (depicted in Fig. 3). In this type of system, the junction of two (or more) types of materials give rise to a confinement potential due to the band mismatch (difference in gap energy together with its alignment with respect to each other) of the materials. Therefore, the total wave function will be composed by the Bloch factors, $u_{n,\vec{k}}(\vec{r})$, of each material enveloped by slowly varying functions.¹²⁵⁻¹²⁸ This implies that each material that composes our nanostructure has a distinct Bloch function, which at the end implies that all material related parameter acquires a spatial dependence. Usually, this spatial dependence of the Bloch factor is neglected and only the effective masses are allowed to vary.¹⁵³

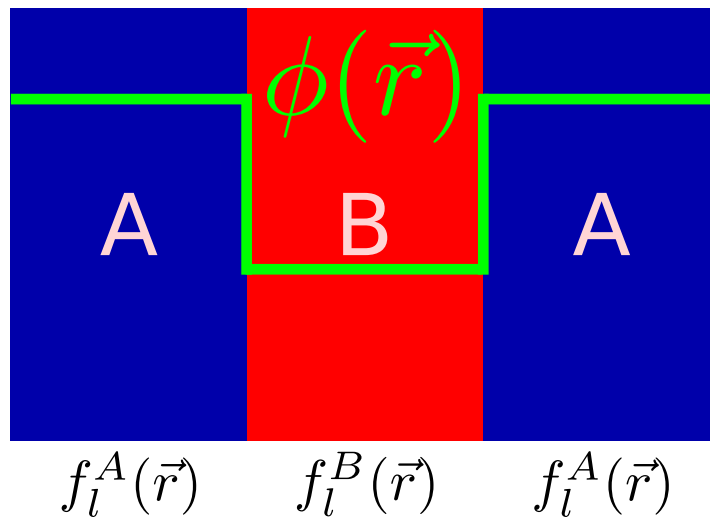


Figure 3: Heterostructure with a 1D confinement profile. The junction of two or more materials creates a confinement profile along the growth direction.

Source: By the author.

2.2 Time reversal symmetry - Intermission

Time reversal is a transformation that reverses the arrow of time: $T : t \rightarrow -t$. It's a symmetry, T , of the Hamiltonian, H , if $[H, T] = 0$, which means that if $|\Psi\rangle$ is an eigenstate of H , then so is $T |\Psi\rangle$.

To find the representation of the time reversal operator, we look at the commutators

with \hat{x} and \hat{p} . We know that

$$T\hat{x}T^{-1} = \hat{x}, \quad T\hat{p}T^{-1} = -\hat{p}, \quad (2.27)$$

therefore

$$\begin{aligned} T[\hat{x}, \hat{p}]T^{-1} &= T(\hat{x}\hat{p} - \hat{p}\hat{x})T^{-1} \\ &= T\hat{x}\hat{p}T^{-1} - T\hat{p}\hat{x}T^{-1} \\ &= T\hat{x}T^{-1}T\hat{p}T^{-1} - T\hat{p}T^{-1}T\hat{x}T^{-1} \\ &= -\hat{x}\hat{p} + \hat{p}\hat{x} \\ &= -[\hat{x}, \hat{p}], \end{aligned} \quad (2.28)$$

meaning that

$$T[\hat{x}, \hat{p}]T^{-1} = TihT^{-1} = -[\hat{x}, \hat{p}] = -ih, \quad (2.29)$$

leading to the equation $TiT^{-1} = -i$.

Hence, the time reversal operator is proportional to the complex conjugation operator. Such operators are called anti-unitary. For spinless particles, $T = UK$, where K is the complex-conjugation operator and U is a unitary matrix.

If we apply the time reversal operator two times, we should go back to the original state, up to a phase matrix, therefore

$$T^2 = UKUK = UU^* = U(U^T)^{-1} = \phi, \quad (2.30)$$

leading to

$$U(U^T)^{-1} = \phi \rightarrow U = \phi U^T, \quad U^T = U\phi, \quad (2.31)$$

and, hence,

$$U = \phi U^T = \phi U\phi. \quad (2.32)$$

This can happen only if $\phi = \pm 1$, meaning that $T^2 = \pm 1$. For spinless particles, $\phi = 1$ which satisfies the unitary requirement for U .

For spinful particles, since the spin is an internal angular momentum, \vec{S} , and because the angular momentum is itself a momentum which is odd under time reversal, we get $T\vec{S}T^{-1} = -\vec{S}$. This implies that the spin flips its direction under time reversal and we can represent this action by a rotation π around some arbitrary axis. The time reversal operator is fixed:¹⁵⁴

$$T = e^{-i\pi S_y} K. \quad (2.33)$$

Assuming the standard spin representation for S_y as purely imaginary, we have

$$\begin{aligned} T \cdot T &= \exp(-i\pi S_y) [K \exp(-i\pi S_y) K] \\ &= \exp(-i\pi S_y) \exp(i\pi S_y^*) \\ &= \exp(-i2\pi S_y), \end{aligned} \quad (2.34)$$

meaning that the application of the time reversal operator twice rotates the spin by 2π : for particles with integer spin it is equivalent to the identity, but for half-integer spin, it gives a factor of -1. Evaluating the exponential for spin- $\frac{1}{2}$ using $\vec{S} = \frac{\hbar}{2}(\sigma_x, \sigma_y, \sigma_z)$ we obtain

$$\begin{aligned} e^{-\frac{i\pi\sigma_y}{2}} &= \sum_{k=0}^{\infty} \frac{1}{k!} \left(-\frac{i\pi\sigma_y}{2}\right)^k \\ &= \cos\left(\frac{\pi}{2}\right) \begin{pmatrix} 1 & 0 \\ 0 & 1 \end{pmatrix} + \sin\left(\frac{\pi}{2}\right) \begin{pmatrix} 0 & -1 \\ 1 & 0 \end{pmatrix} \\ &= -i\sigma_y, \end{aligned} \quad (2.35)$$

making $T^2 = -1$.

Perhaps the most known use of time reversal symmetry is in the Kramer's theorem, that says that for each energy in a system with an odd number of half-integer spin particles there are at least two degenerate states. The proof is simple and just require us to show the orthogonality between $|\Psi\rangle$ and $T|\Psi\rangle$. Also, for time reversal invariant Hamiltonians, we can show that states comes in Kramers' degenerate pairs. When there is also translational symmetry, the momentum becomes a good quantum number. In this case, the Kramer's degenerescence generically split into states at momenta \vec{k} and $-\vec{k}$. Only states at special momenta $\vec{k} = -\vec{k}$ remain double degenerated. This specials points are

usually the high symmetry points of our system. For graphene they are the K points and for III-V semiconductors the Γ -point.

2.3 Landè g-factor

In this section we show that using the minimal coupling in the effective mass equations we obtain the orbital corrections to the electron g-factor.

2.3.1 One-band model

For a crystal with inversion symmetry, the one-electron band state for a given n and \vec{k} is at least twofold degenerate. For this system the effective mass equations up to second order in perturbation theory, for $\vec{P} \cdot \vec{\pi}$, become particularly simple. Neglecting the terms involving $V(\vec{r})$, the pair of coupled equations (2.25) becomes,

$$\left\{ \frac{\vec{P}}{2m} + \sum_{\mu} \frac{\vec{P} \cdot \vec{\pi}_{j\mu} \vec{\pi}_{\mu j} \cdot \vec{P}}{(\varepsilon_j^{(0)} - \varepsilon_{\mu}^{(0)})} + g\mu_B \vec{S}_j \cdot \vec{B} - \varepsilon \right\} f_j(\vec{r}) = 0, \quad (2.36)$$

where $\vec{\pi}_{j\mu}$ and \vec{S}_j are 2×2 matrices.

Any 2×2 matrix can be written as a combination of Pauli matrices, hence¹²¹

$$\begin{aligned} \pi_{j\mu} &= \vec{t}_{j\mu} \vec{I} + i(\vec{u}_{j\mu} \sigma_x + \vec{v}_{j\mu} \sigma_y + \vec{w}_{j\mu} \sigma_z) \\ \pi_{\mu j} &= \vec{t}_{j\mu} \vec{I} - i(\vec{u}_{j\mu} \sigma_x + \vec{v}_{j\mu} \sigma_y + \vec{w}_{j\mu} \sigma_z) \\ S_j &= \vec{a}_j \frac{\sigma_x}{2} + \vec{b}_j \frac{\sigma_y}{2} + \vec{c}_j \frac{\sigma_z}{2}. \end{aligned} \quad (2.37)$$

From Eq. (2.37), the product of two π -matrix components can be decomposed into a spin-independent symmetric part and a spin-dependent anti-symmetric part as,

$$\pi_{nn'}^{\xi} \pi_{m'm}^{\eta} = \left\{ \pi_{nn'}^{\xi}, \pi_{m'm}^{\eta} \right\}_S + \left\{ \pi_{nn'}^{\xi}, \pi_{m'm}^{\eta} \right\}_{AS}. \quad (2.38)$$

Here ξ, η are x, y, z . $\left\{ \pi_{nn'}^{\xi}, \pi_{m'm}^{\eta} \right\}_S$ is the symmetrized combination,

$$\begin{aligned} \left\{ \pi_{nn'}^{\xi}, \pi_{m'm}^{\eta} \right\}_S &= \frac{1}{2} \left[\pi_{nn'}^{\xi} \pi_{m'm}^{\eta} + \pi_{mm'}^{\eta} \pi_{n'n}^{\xi} \right] \\ &= \left[t_{nn'}^{\xi} t_{mm'}^{\eta} + u_{nn'}^{\xi} u_{mm'}^{\eta} + v_{nn'}^{\xi} v_{mm'}^{\eta} + w_{nn'}^{\xi} w_{mm'}^{\eta} \right] \vec{I}, \end{aligned} \quad (2.39)$$

and $\{\pi_{nn'}^\xi, \pi_{m'm}^\eta\}_{AS}$ is the anti-symmetrized combination,

$$\begin{aligned} \{\pi_{nn'}^\xi, \pi_{m'm}^\eta\}_{AS} &= \frac{1}{2} [\pi_{nn'}^\xi \pi_{m'm}^\eta - \pi_{mm'}^\eta \pi_{n'n}^\xi] \\ &= -i\sigma_x [t_{nn'}^\xi u_{mm'}^\eta - u_{nn'}^\xi t_{mm'}^\eta + w_{nn'}^\xi v_{mm'}^\eta - v_{nn'}^\xi w_{mm'}^\eta] \\ &\quad -i\sigma_y [t_{nn'}^\xi v_{mm'}^\eta - v_{nn'}^\xi t_{mm'}^\eta + u_{nn'}^\xi w_{mm'}^\eta - w_{nn'}^\xi u_{mm'}^\eta] \\ &\quad -i\sigma_z [t_{nn'}^\xi w_{mm'}^\eta - w_{nn'}^\xi t_{mm'}^\eta + v_{nn'}^\xi u_{mm'}^\eta + u_{nn'}^\xi v_{mm'}^\eta], \end{aligned} \quad (2.40)$$

therefore

$$\{\pi_{j\mu}^x, \pi_{\mu j}^y\}_{AS} = \frac{1}{2} [\vec{\pi}_{j\mu} \times \vec{\pi}_{\mu j}]_z. \quad (2.41)$$

Applying this definitions to (2.36), and using the commutation relations $[P_x, P_y] = -i\hbar e B_z$, etc, we find,

$$\left[\frac{1}{2m} \vec{P} \cdot \vec{\alpha}_j \cdot \vec{P} + \mu_B \vec{S} \cdot \vec{g}_j \cdot \vec{B} - \varepsilon \right] f_j(\vec{r}) = 0, \quad (2.42)$$

where

$$\vec{\alpha}_j = \vec{I} + 2m \sum_{\mu} \frac{\{\vec{\pi}_{j\mu}, \vec{\pi}_{\mu j}\}_S}{(\varepsilon_j^{(0)} - \varepsilon_{\mu}^{(0)})}, \quad (2.43)$$

is the effective mass tensor, and

$$\mu_B \vec{S} \cdot \vec{g}_j \cdot \vec{B} = \mu_B \left[g (\vec{a}_j S_x + \vec{b}_j S_y + \vec{c}_j S_z) - im \sum_{\mu} \frac{\vec{\pi}_{j\mu} \times \vec{\pi}_{\mu j}}{(\varepsilon_j^{(0)} - \varepsilon_{\mu}^{(0)})} \right] \cdot \vec{B}, \quad (2.44)$$

with $\vec{S} = \vec{\sigma}/2$. Here, \vec{g}_j is the effective Landè g-factor tensor, first obtained by [Roth, Lax & Zwerdling](#).⁷⁴

In the above equations we identify that the effective mass of an electron in a crystal arises from the symmetric part of the interband coupling, whereas the orbital correction to the g-factor comes from the anti-symmetric part.

2.3.2 Degenerate bands

The set of coupled equations up to second order in $\vec{P} \cdot \vec{\pi}$, can be obtained from (2.23) and (2.24),

$$(H_{\text{eff}})_{lj} = \varepsilon_l^{(0)} \delta_{lj} + \frac{\vec{P}^2}{2m} + \vec{P} \cdot \vec{\pi}_{lj} + \sum_{\mu} \frac{\vec{\pi}_{l\mu} \cdot \vec{P} \vec{\pi}_{\mu j} \cdot \vec{P}}{(\varepsilon - \varepsilon_{\mu}^{(0)})} + g \mu_B \vec{S}_{lj} \cdot \vec{B} \quad (2.45)$$

Following the same procedure as before, we can write the product $\vec{\pi}_{l\mu} \cdot \vec{P} \vec{\pi}_{\mu j} \cdot \vec{P}$ in terms of the symmetrized and anti-symmetrized combinations as

$$\vec{\pi}_{l\mu} \cdot \vec{P} \vec{\pi}_{\mu j} \cdot \vec{P} = \frac{1}{2} \vec{P} \cdot (\vec{\pi}_{l\mu} \vec{\pi}_{\mu j} + \vec{\pi}_{\mu j} \vec{\pi}_{l\mu}) \cdot \vec{P} + \frac{1}{2} \vec{P} \cdot (\vec{\pi}_{l\mu} \vec{\pi}_{\mu j} - \vec{\pi}_{\mu j} \vec{\pi}_{l\mu}) \cdot \vec{P} \quad (2.46)$$

therefore, Eq. (2.45) becomes

$$(H_{\text{eff}})_{lj} = \varepsilon_l^{(0)} \delta_{lj} + \vec{P} \cdot \vec{\pi}_{lj} + \sum_{\xi, \eta}^{x, y, z} D_{ij}^{\xi, \eta} P_{\xi} P_{\eta} - \vec{\mu}_{lj} \cdot \vec{B}, \quad (2.47)$$

where

$$D_{ij}^{\xi, \eta} = \frac{1}{2} \sum_{\mu} \left(\frac{\pi_{l\mu}^{\xi} \pi_{\mu j}^{\eta} + \pi_{l\mu}^{\eta} \pi_{\mu j}^{\xi}}{\varepsilon - \varepsilon_{\mu}^{(0)}} \right) + \frac{\delta_{lj} \delta_{\xi\eta}}{2m}, \quad (2.48)$$

is the effective mass tensor, and

$$\vec{\mu}_{lj} = -\mu_B \left\{ g S_{lj} - im \sum_{\mu} \frac{\vec{\pi}_{l\mu} \times \vec{\pi}_{\mu j}}{\varepsilon - \varepsilon_{\mu}^{(0)}} \right\}, \quad (2.49)$$

is the Landè g-factor tensor.

In Eq. (2.47) the term $\vec{P} \cdot \vec{\pi}_{lj}$ is zero if we are dealing with the bands inside the same representation, as is the case of the valence bands. Nevertheless, it is non zero when j and l belongs to bands with different representations. Hence, if we are treating conduction and valence band as the full basis set, the term $\vec{P} \cdot \vec{\pi}_{lj} \rightarrow \vec{P} \cdot \vec{\pi}_{cv}$ where c belongs to the conduction band basis states and v to the valence band basis states. This term gives the explicit interband coupling and in the zinc-blende crystal phase it is known as the Kane matrix element.¹²⁴

2.4 Bulk $\mathbf{k} \cdot \mathbf{p}$ matrices

We can classify the various crystal phases by its symmetry group. Using Group Theory, one can find the symmetries of the basis states of each crystal phase and, therefore, determine the non-zero elements. An example of such calculations is found in the MasterThesis of a former student of the LFC group (P. E. Faria Junior). The process of defining the energy bands we want to describe and subsequently devising a parametrized $\mathbf{k} \cdot \mathbf{p}$ Hamiltonian is a semi-empirical method because one ends up with the zeros and non-zero elements without knowing their values.

Historically, the $\mathbf{k} \cdot \mathbf{p}$ Hamiltonians have been derived to describe the very vicinity of some high symmetry \vec{k}_0 point, therefore, simplifying the Hamiltonian to only a few parameters such as the electron effective mass and the inter band coupling, also known as the Kane parameter or the optical matrix element.¹²⁴ Effective mass parameters can be obtained by standard experimental techniques such as cyclotron resonance^{155,156} or optical measurements^{157,158} to cite a few, or theoretically, by fitting a parabolic dispersion^{159,160} very close to a high symmetry point, like the Γ -point. A problem with these techniques is that they only work for the inner energy bands, i. e., the ones closest to the Fermi level, usually the first conduction band and the heavy- and light-hole bands. Another problem is that the coupling parameters, like the Kane parameter, cannot be directly determined by those aforementioned techniques.⁷⁵ Recently, the LFC group and colleagues have proposed a general method in which all the parameters, inter band coupling inclusive, can be determined through a fitting of the $\mathbf{k} \cdot \mathbf{p}$ Hamiltonians to a pre-established band structure.¹¹⁹ This technique was latter applied to determine the parameters of a new wurtzite $\mathbf{k} \cdot \mathbf{p}$ Hamiltonian, also developed by the LFC group and colleagues,¹⁴⁴ using *ab initio* band structure.¹⁰⁹

2.4.1 Extended Kane model

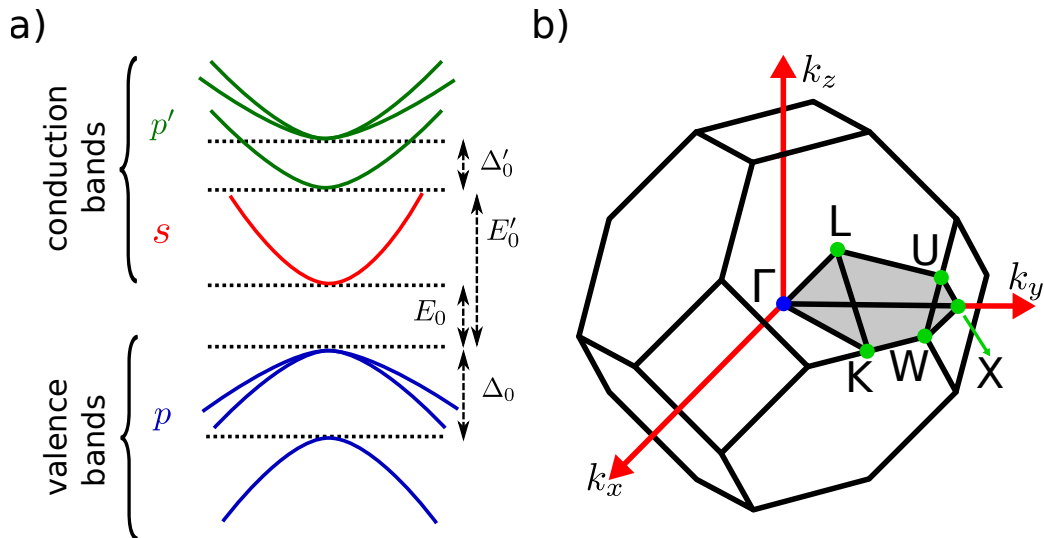


Figure 4: Bulk band scheme and first Brillouin zone for a zinc-blende crystal. In a) we depict the 14 bands taken into account in the Extended Kane model. In b) we show the Brillouin zone and its high symmetry points.

Source: By the author.

The standard 8-band Luttinger-Kohn and/or Kane^{54,123,124,161–164} description of the zinc-blende crystal have successfully explained and predicted a variety of experimental results for both narrow- and wide-gap nanostructures. However, zinc-blende is a non centro-symmetric crystal which implies that the Krammers degeneracy should be lifted, effect not captured by the aforementioned $\mathbf{k} \cdot \mathbf{p}$ methods in general. A natural extension of these methods is the explicit inclusion of extra, higher in energy, conduction bands, and its explicit couplings with the previous ones, as seen in Fig. 4a). This extension is known as the five level or extended Kane model^{75,165,166} and in view of Löwdin partitioning it is composed by 14 states in the class A, $\{\phi_{\alpha\vec{k}} \mid \alpha = 1, \dots, 14\}$.

In a tight-binding point of view, the standard 8-band $\mathbf{k} \cdot \mathbf{p}$ model describes the antibonding s and the three bonding p orbitals. The zinc-blende crystal phase belongs to the T_d simple group representation which means that the standard 8-band $\mathbf{k} \cdot \mathbf{p}$ model describes the first conduction band (with Γ_6 symmetry) and the three topmost valence bands: heavy- and light-hole (Γ_8) and split-off hole, (Γ_7).^{123,124,161,163,164,167} On the other hand, the 14-band $\mathbf{k} \cdot \mathbf{p}$ model also take into consideration the three antibonding p orbitals, as seen in Fig. 4a).

Table 1: Basis set, in the angular momentum representation, for the 14-band $\mathbf{k} \cdot \mathbf{p}$ model. We denote the antibonding s and p orbitals as $\Gamma_i^c, i = 6, 7, 8$ and the bonding p orbitals $\Gamma_i^v, i = 7, 8$.

Γ_8^c	$\left \frac{3}{2}, \frac{3}{2} \right\rangle_{c'} = -\frac{1}{\sqrt{2}} (X' + iY') \uparrow\rangle$	$\left \frac{3}{2}, \frac{1}{2} \right\rangle_{c'} = -\frac{1}{\sqrt{6}} (X' + iY') \downarrow\rangle + \frac{2}{\sqrt{6}} Z' \uparrow\rangle$
	$\left \frac{3}{2}, -\frac{1}{2} \right\rangle_{c'} = \frac{1}{\sqrt{6}} (X' - iY') \uparrow\rangle + \frac{2}{\sqrt{6}} Z' \downarrow\rangle$	$\left \frac{3}{2}, -\frac{3}{2} \right\rangle_{c'} = \frac{1}{\sqrt{2}} (X' - iY') \downarrow\rangle$
Γ_7^c	$\left \frac{1}{2}, \frac{1}{2} \right\rangle_{c'} = -\frac{1}{\sqrt{3}} (X' + iY') \downarrow\rangle - \frac{1}{\sqrt{3}} Z' \uparrow\rangle$	$\left \frac{1}{2}, -\frac{1}{2} \right\rangle_{c'} = -\frac{1}{\sqrt{3}} (X' - iY') \uparrow\rangle + \frac{1}{\sqrt{3}} Z' \downarrow\rangle$
Γ_6^c	$\left \frac{1}{2}, \frac{1}{2} \right\rangle_c = S \uparrow\rangle$	$\left \frac{1}{2}, -\frac{1}{2} \right\rangle_c = S \downarrow\rangle$
Γ_8^v	$\left \frac{3}{2}, \frac{3}{2} \right\rangle_v = -\frac{1}{\sqrt{2}} (X + iY) \uparrow\rangle$	$\left \frac{3}{2}, \frac{1}{2} \right\rangle_v = -\frac{1}{\sqrt{6}} (X + iY) \downarrow\rangle + \frac{2}{\sqrt{6}} Z \uparrow\rangle$
	$\left \frac{3}{2}, -\frac{1}{2} \right\rangle_v = \frac{1}{\sqrt{6}} (X - iY) \uparrow\rangle + \frac{2}{\sqrt{6}} Z \downarrow\rangle$	$\left \frac{3}{2}, -\frac{3}{2} \right\rangle_v = \frac{1}{\sqrt{2}} (X - iY) \downarrow\rangle$
Γ_7^v	$\left \frac{1}{2}, \frac{1}{2} \right\rangle_v = -\frac{1}{\sqrt{3}} (X + iY) \downarrow\rangle - \frac{1}{\sqrt{3}} Z \uparrow\rangle$	$\left \frac{1}{2}, -\frac{1}{2} \right\rangle_v = -\frac{1}{\sqrt{3}} (X - iY) \uparrow\rangle + \frac{1}{\sqrt{3}} Z \downarrow\rangle$

Source: Adapted from WINKLER,¹³² FABIAN et al.⁶⁷

The total $\mathbf{k} \cdot \mathbf{p}$ Hamiltonian, in the basis given in Table 1, reads as

$$H_{AM}^{ZB} = \begin{pmatrix} H_v & H_{vc} & H_{vc'} \\ H_{cv} & H_c & H_{cc'} \\ H_{c'v} & H_{c'c} & H_{c'} \end{pmatrix} + \begin{pmatrix} H_{SO} & 0 & H_{SO}'' \\ 0 & 0 & 0 \\ H_{SO}''^\dagger & 0 & H_{SO}' \end{pmatrix}. \quad (2.50)$$

the specific terms follow. Here and throughout the text we will use the following notation, $k^2 = k_x^2 + k_y^2 + k_z^2$ and $k_{\pm} = k_x \pm ik_y$.

The quadratic dispersion of the Γ_6^c band is given by

$$H_c = \text{diag} [E_0 + Fk^2, E_0 + Fk^2], \quad (2.51)$$

F being the effective mass parameter and E_0 its energy at Γ -point, measured from the top of the valence Γ_8^v band.

The quadratic dispersion of the Γ_8^c and Γ_7^c bands is given by

$$H'_c = \text{diag} [E'_0 + Ak^2, E'_0 + Ak^2], \quad (2.52)$$

where A its effective mass parameter (the inverse of the free electron mass in this approximation) and E'_0 its energy at Γ -point, measured from the top of the valence Γ_8^v band.

The first order interaction term between Γ_6^c with Γ_8^c and Γ_7^c conduction bands is

$$H_{cc'} = P_1 \begin{pmatrix} -\frac{ik_+}{\sqrt{2}} & i\sqrt{\frac{2}{3}}k_z & \frac{ik_-}{\sqrt{6}} & 0 & -\frac{ik_z}{\sqrt{3}} & -\frac{ik_-}{\sqrt{3}} \\ 0 & -\frac{ik_+}{\sqrt{6}} & i\sqrt{\frac{2}{3}}k_z & \frac{ik_-}{\sqrt{2}} & -\frac{ik_+}{\sqrt{3}} & \frac{ik_z}{\sqrt{3}} \end{pmatrix} \quad (2.53)$$

The first order interaction term between Γ_6^c with Γ_8^v and Γ_7^v valence bands is

$$H_{cv} = P_0 \begin{pmatrix} -\frac{k_+}{\sqrt{2}} & \sqrt{\frac{2}{3}}k_z & \frac{k_-}{\sqrt{6}} & 0 & -\frac{k_z}{\sqrt{3}} & -\frac{k_-}{\sqrt{3}} \\ 0 & -\frac{k_+}{\sqrt{6}} & \sqrt{\frac{2}{3}}k_z & \frac{k_-}{\sqrt{2}} & -\frac{k_+}{\sqrt{3}} & \frac{k_z}{\sqrt{3}} \end{pmatrix}, \quad (2.54)$$

and the first order interaction term between Γ_8^c and Γ_7^c conduction bands with Γ_8^v and Γ_7^v valence bands is

$$H_{c'v} = Q_0 \begin{pmatrix} 0 & \frac{ik_+}{\sqrt{3}} & \frac{ik_z}{\sqrt{3}} & 0 & -\frac{ik_+}{\sqrt{6}} & -i\sqrt{\frac{2}{3}}k_z \\ -\frac{ik_-}{\sqrt{3}} & 0 & 0 & \frac{ik_z}{\sqrt{3}} & 0 & \frac{ik_+}{\sqrt{2}} \\ -\frac{ik_z}{\sqrt{3}} & 0 & 0 & -\frac{ik_+}{\sqrt{3}} & -\frac{ik_-}{\sqrt{2}} & 0 \\ 0 & -\frac{ik_z}{\sqrt{3}} & \frac{ik_-}{\sqrt{3}} & 0 & -i\sqrt{\frac{2}{3}}k_z & \frac{ik_-}{\sqrt{6}} \\ \frac{ik_-}{\sqrt{6}} & 0 & \frac{ik_+}{\sqrt{2}} & i\sqrt{\frac{2}{3}}k_z & 0 & 0 \\ i\sqrt{\frac{2}{3}}k_z & -\frac{ik_-}{\sqrt{2}} & 0 & -\frac{ik_+}{\sqrt{6}} & 0 & 0 \end{pmatrix}. \quad (2.55)$$

The first order spin-orbit coupling for the Γ_8^c and Γ_7^c conduction bands is

$$H'_{SO} = \text{diag} (\Delta'_0, \Delta'_0, \Delta'_0, \Delta'_0, 0, 0), \quad (2.56)$$

for the Γ_8^v and Γ_7^v is

$$H_{SO} = \text{diag} (0, 0, 0, 0, -\Delta_0, -\Delta_0), \quad (2.57)$$

and the spin-orbit coupling between Γ_8^c and Γ_7^c conduction bands and Γ_8^v and Γ_7^v valence bands is

$$H''_{SO} = \text{diag} \left(-\frac{i}{3}\Delta_-, -\frac{1}{3}\Delta_-, \frac{i}{3}\Delta_-, \frac{1}{3}\Delta_-, \frac{2i}{3}\Delta_-, -\frac{2}{3}\Delta_- \right). \quad (2.58)$$

Finally, the second order $\mathbf{k} \cdot \mathbf{p}$ interaction on the Γ_8^v and Γ_7^v valence bands is

$$H_{vv} = \begin{pmatrix} Q & S & R & 0 & -\frac{S}{\sqrt{2}} & -\sqrt{2}R \\ S^\dagger & T & 0 & R & \frac{Q-T}{\sqrt{2}} & \sqrt{\frac{3}{2}}S \\ R^\dagger & 0 & T & -S & \sqrt{\frac{3}{2}}S^\dagger & \frac{T-Q}{\sqrt{2}} \\ 0 & R^\dagger & -S^\dagger & Q & \sqrt{2}R^\dagger & -\frac{S^\dagger}{\sqrt{2}} \\ -\frac{S^\dagger}{\sqrt{2}} & \frac{Q-T}{\sqrt{2}} & \sqrt{\frac{3}{2}}S & \sqrt{2}R & \frac{(Q+T)}{2} & 0 \\ -\sqrt{2}R^\dagger & \sqrt{\frac{3}{2}}S^\dagger & \frac{T-Q}{\sqrt{2}} & -\frac{S}{\sqrt{2}} & 0 & \frac{(Q+T)}{2} \end{pmatrix}, \quad (2.59)$$

whose terms are

$$\begin{aligned} Q &= -(k_x^2 + k_y^2)(\gamma_1 + \gamma_2) - k_z^2(\gamma_1 - 2\gamma_2) \\ T &= -(k_x^2 + k_y^2)(\gamma_1 - \gamma_2) - k_z^2(\gamma_1 + 2\gamma_2) \\ R &= \sqrt{3}[\gamma_2(k_x^2 - k_y^2) - 2i\gamma_3k_xk_y] \\ S &= 2\sqrt{3}\gamma_3k_-k_z, \end{aligned} \quad (2.60)$$

$\gamma_1, \gamma_2, \gamma_3$ being the effective mass parameters for the Γ_8^v and Γ_7^v valence bands.

The parameters $E_0, E'_0, P_0, P_1, Q_0, \Delta_0, \Delta_-, \Delta'_0, F, A$ and $\gamma_1, \gamma_2, \gamma_3$ are specific for each semiconductor material and its values have to be filled in by external sources. ^{168, 169}

Also, with the explicit inclusion of the $\mathbf{k} \cdot \mathbf{p}$ couplings in the 14-band Hamiltonian the effective mass parameters are modified as following

$$\gamma_1 = \gamma_1^L - \frac{1}{3} \left(\frac{P_0^2}{E_0} + \frac{Q_0^2}{\Delta'_0 + E'_0} + \frac{Q_0^2}{E'_0} \right), \quad (2.61)$$

$$\gamma_2 = \gamma_2^L - \frac{1}{6} \left(\frac{P_0^2}{E_0} - \frac{Q_0^2}{E_0'} \right), \quad (2.62)$$

$$\gamma_3 = \gamma_3^L - \frac{1}{6} \left(\frac{P_0^2}{E_0} + \frac{Q_0^2}{E_0'} \right), \quad (2.63)$$

the electron effective mass becomes

$$\frac{m_0}{m^*} - 1 = -\frac{1}{3} \left(\frac{P_0^2}{\Delta_0 + E_0} + 2\frac{P_0^2}{E_0} + 2\frac{P_1^2}{E_0 - E_0' - \Delta_0'} + \frac{P_1^2}{E_0 - E_0'} \right), \quad (2.64)$$

and the g-factor becomes

$$\frac{g^*}{g_0} - 1 = -\frac{1}{3} \left(\frac{P_0^2}{E_0 + \Delta_0} - \frac{P_0^2}{E_0} + \frac{P_1^2}{E_0 - E_0'} - \frac{P_1^2}{E_0 - E_0' - \Delta_0'} \right) \quad (2.65)$$

where γ_1^L , γ_2^L , γ_3^L are the Luttinger parameters,¹²³ m^* the electron effective mass parameter and g^* the effective Landè g-factor.^{75, 132, 149}

In bulk systems, if one wants to obtain the dispersion relation along another direction they only have to vary the wave-vector k accordingly. For the [110] direction we make the following substitutions $k_x \rightarrow k \cos \phi$ and $k_y \rightarrow k \sin \phi$ where ϕ is the polar angle (the angle with the \hat{z} axis). For the [111] direction we make $k_x \rightarrow k \sin \theta \cos \phi$, $k_y \rightarrow k \sin \theta \sin \phi$ and $k_z \rightarrow k \cos \theta$ where θ is the azimuthal angle (the xy -plane angle). These directions can be visualized in Fig. 4b), the [110] direction is the line connecting the points Γ and K . The [111] direction is the line connecting the points Γ and L .

What about if one wants to obtain the energy dispersion of confined systems, like quantum wells, wires or dots, along these directions? In the next subsection we show how to perform a matrix rotation which will transform the coordinate system to the desired orientation.

2.4.1.1 [110] direction

To derive the $\mathbf{k} \cdot \mathbf{p}$ Hamiltonian in a new growth direction we need to both rotate the coordinate axis as well as the spin axis from the old direction to the new one. Consider two coordinate systems x, y, z and $\tilde{x}, \tilde{y}, \tilde{z}$, the matrix that performs the rotation from one

frame to the other is given by

$$U = \begin{bmatrix} \cos \theta \cos \phi & \cos \theta \sin \phi & -\sin \theta \\ -\sin \phi & \cos \phi & 0 \\ \sin \theta \cos \phi & \sin \theta \sin \phi & \cos \theta \end{bmatrix}, \quad (2.66)$$

and the matrix that rotates the spin degree of freedom from one frame to the other is given by

$$M_s = \begin{bmatrix} e^{-i\frac{\phi}{2}} \cos \frac{\theta}{2} & e^{i\frac{\phi}{2}} \sin \frac{\theta}{2} \\ -e^{-i\frac{\phi}{2}} \sin \frac{\theta}{2} & e^{i\frac{\phi}{2}} \cos \frac{\theta}{2} \end{bmatrix}. \quad (2.67)$$

Therefore the complete rotation matrix is obtained by making the direct product of the spinorial and spatial rotation matrices, $M_s \otimes U$.

To rotate the 14-band $\mathbf{k} \cdot \mathbf{p}$ Hamiltonian from the [001] coordinate system to the [110] and write the final Hamiltonian in the basis set given in Table 1, in the new coordinate system $|\langle \tilde{X}', \tilde{Y}', \tilde{Z}', \tilde{X}, \tilde{Y}, \tilde{Z} \rangle (\uparrow, \downarrow)\rangle$, we do

$$\tilde{H}_{ZB,AM}^{[110]} = U_{ZB}^{\dagger,14} M_c^* U_{ZB}^{14} H_{AM}^{ZB} U_{ZB}^{14,\dagger} M_c^T U_{ZB}^{14}, \quad (2.68)$$

where

$$M_c = \begin{pmatrix} M_s \otimes U & 0 & 0 \\ 0 & M_s & 0 \\ 0 & 0 & M_s \otimes U \end{pmatrix}, \quad (2.69)$$

with $\theta = \pi/2$ and $\phi = \pi/4$. The coordinate system rotation is depicted in Fig. 5.

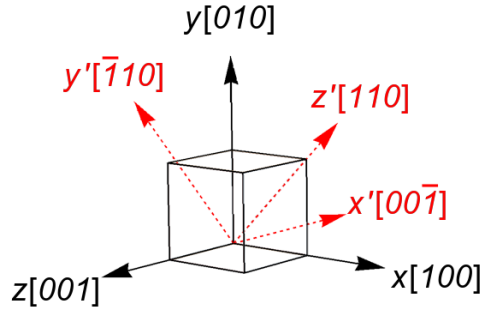


Figure 5: Representation of the new coordinate axis in the old frame of reference. We are rotating the $[001]$ to the $[110]$, i. e., we want the \hat{z} to be transformed to \hat{z}' .

Source: By the author.

The matrix, U_{ZB}^{14} , which writes the angular momentum basis in the orbital basis is

$$U_{ZB}^{14} = \begin{pmatrix} -\frac{1}{\sqrt{2}} & 0 & \frac{1}{\sqrt{6}} & 0 & 0 & -\frac{1}{\sqrt{3}} & 0 & 0 & 0 & 0 & 0 & 0 & 0 & 0 & 0 \\ -\frac{i}{\sqrt{2}} & 0 & -\frac{i}{\sqrt{6}} & 0 & 0 & \frac{i}{\sqrt{3}} & 0 & 0 & 0 & 0 & 0 & 0 & 0 & 0 & 0 \\ 0 & \frac{2}{\sqrt{6}} & 0 & 0 & -\frac{1}{\sqrt{3}} & 0 & 0 & 0 & 0 & 0 & 0 & 0 & 0 & 0 & 0 \\ 0 & -\frac{1}{\sqrt{6}} & 0 & \frac{1}{\sqrt{2}} & -\frac{1}{\sqrt{3}} & 0 & 0 & 0 & 0 & 0 & 0 & 0 & 0 & 0 & 0 \\ 0 & -\frac{i}{\sqrt{6}} & 0 & -\frac{i}{\sqrt{2}} & -\frac{i}{\sqrt{3}} & 0 & 0 & 0 & 0 & 0 & 0 & 0 & 0 & 0 & 0 \\ 0 & 0 & \frac{2}{\sqrt{6}} & 0 & 0 & \frac{1}{\sqrt{3}} & 0 & 0 & 0 & 0 & 0 & 0 & 0 & 0 & 0 \\ 0 & 0 & 0 & 0 & 0 & 0 & 1 & 0 & 0 & 0 & 0 & 0 & 0 & 0 & 0 \\ 0 & 0 & 0 & 0 & 0 & 0 & 0 & 1 & 0 & 0 & 0 & 0 & 0 & 0 & 0 \\ 0 & 0 & 0 & 0 & 0 & 0 & 0 & 0 & -\frac{1}{\sqrt{2}} & 0 & \frac{1}{\sqrt{6}} & 0 & 0 & -\frac{1}{\sqrt{3}} & 0 \\ 0 & 0 & 0 & 0 & 0 & 0 & 0 & 0 & -\frac{i}{\sqrt{2}} & 0 & -\frac{i}{\sqrt{6}} & 0 & 0 & \frac{i}{\sqrt{3}} & 0 \\ 0 & 0 & 0 & 0 & 0 & 0 & 0 & 0 & 0 & \frac{2}{\sqrt{6}} & 0 & 0 & -\frac{1}{\sqrt{3}} & 0 & 0 \\ 0 & 0 & 0 & 0 & 0 & 0 & 0 & 0 & 0 & -\frac{1}{\sqrt{6}} & 0 & \frac{1}{\sqrt{2}} & -\frac{1}{\sqrt{3}} & 0 & 0 \\ 0 & 0 & 0 & 0 & 0 & 0 & 0 & 0 & 0 & -\frac{i}{\sqrt{6}} & 0 & -\frac{i}{\sqrt{2}} & -\frac{i}{\sqrt{3}} & 0 & 0 \\ 0 & 0 & 0 & 0 & 0 & 0 & 0 & 0 & 0 & 0 & \frac{2}{\sqrt{6}} & 0 & 0 & \frac{1}{\sqrt{3}} & 0 \end{pmatrix}. \quad (2.70)$$

The final step is to rewrite the old wave vector \vec{k} with respect to the new ones: $k_x = -\frac{1}{\sqrt{2}}\tilde{k}_y + \frac{1}{\sqrt{2}}\tilde{k}_z$, $k_y = \frac{1}{\sqrt{2}}\tilde{k}_y + \frac{1}{\sqrt{2}}\tilde{k}_z$ and $k_z = -\tilde{k}_x$. Computing eq. (2.68), and making the wave vectors substitutions, we realize that only two blocks are different from the $[001]$ direction: the $H_{vc'}$ and H_{vv} .

The spin-orbit coupling between Γ_8^c and Γ_7^c conduction bands with Γ_8^v and Γ_7^v

valence bands now reads as

$$H_{vc'} = Q_0 \begin{pmatrix} 2k_x & \frac{k_z}{\sqrt{3}} & \frac{k'_+}{2\sqrt{3}} & 0 & -\frac{k_z}{\sqrt{6}} & -\frac{k'_+}{\sqrt{6}} \\ \frac{k_z}{\sqrt{3}} & -2k_x & 0 & \frac{k'_+}{2\sqrt{3}} & \frac{k_x}{\sqrt{2}} & \frac{k_z}{\sqrt{2}} \\ \frac{k'_-}{2\sqrt{3}} & 0 & -2k_x & -\frac{k_z}{\sqrt{3}} & \frac{k_z}{\sqrt{2}} & -\frac{k_x}{\sqrt{2}} \\ 0 & \frac{k'_-}{2\sqrt{3}} & -\frac{k_z}{\sqrt{3}} & 2k_x & \frac{k'_-}{\sqrt{6}} & -\frac{k_z}{\sqrt{6}} \\ -\frac{k_z}{\sqrt{6}} & \frac{k_x}{\sqrt{2}} & \frac{k_z}{\sqrt{2}} & \frac{k'_+}{\sqrt{6}} & 0 & 0 \\ -\frac{k'_-}{\sqrt{6}} & \frac{k_z}{\sqrt{2}} & -\frac{k_x}{\sqrt{2}} & -\frac{k_z}{\sqrt{6}} & 0 & 0 \end{pmatrix}, \quad (2.71)$$

and the terms of H_{vv} becomes

$$\begin{aligned} Q &= -k_x^2 (\gamma_1 + \gamma_2) - k_y^2 \left(\gamma_1 - \frac{\gamma_2}{2} + \frac{3\gamma_3}{2} \right) - k_z^2 \left(\gamma_1 - \frac{\gamma_2}{2} - \frac{3\gamma_3}{2} \right) \\ T &= -k_x^2 (\gamma_1 - \gamma_2) - k_y^2 \left(\gamma_1 + \frac{\gamma_2}{2} + \frac{3\gamma_3}{2} \right) - k_z^2 \left(\gamma_1 + \frac{\gamma_2}{2} - \frac{3\gamma_3}{2} \right) \\ R &= \frac{\sqrt{3}}{2} [2\gamma_2 k_x^2 - 4i\gamma_3 k_x k_y - k_y^2 (\gamma_2 + \gamma_3) + k_z^2 (\gamma_3 - \gamma_2)] \\ S &= 2\sqrt{3} k_z (\gamma_3 k_x - i\gamma_2 k_y). \end{aligned} \quad (2.72)$$

To simplify the notation we already dropped the wave-vector tilde.

2.4.1.2 [111] direction

Using the same methodology as in the section before, we can also rotate the [001] 14-band $\mathbf{k} \cdot \mathbf{p}$ Hamiltonian to the [111] direction. The matrix that rotates the coordinate axis is given by

$$U = \begin{bmatrix} \frac{1}{\sqrt{6}} & \frac{1}{\sqrt{6}} & -\frac{2}{\sqrt{6}} \\ -\frac{1}{\sqrt{2}} & \frac{1}{\sqrt{2}} & 0 \\ \frac{1}{\sqrt{3}} & \frac{1}{\sqrt{3}} & \frac{1}{\sqrt{3}} \end{bmatrix}, \quad (2.73)$$

with the coordinate system rotation represented in Fig. (6).

The trigonometric relations used in the spin-rotation matrix, M_s , are: $\sin \frac{\theta}{2} = \sqrt{\frac{3-\sqrt{3}}{6}}$, $\cos \frac{\theta}{2} = \sqrt{\frac{3+\sqrt{3}}{6}}$, $\sin \frac{\phi}{2} = \sqrt{\frac{2-\sqrt{2}}{4}}$ and $\cos \frac{\phi}{2} = \sqrt{\frac{2+\sqrt{2}}{4}}$. Also, the wave-vector transforms as $k_x = \frac{1}{\sqrt{6}} \tilde{k}_x - \frac{1}{\sqrt{2}} \tilde{k}_y + \frac{1}{\sqrt{3}} \tilde{k}_z$, $k_y = \frac{1}{\sqrt{6}} \tilde{k}_x + \frac{1}{\sqrt{2}} \tilde{k}_y + \frac{1}{\sqrt{3}} \tilde{k}_z$ and $k_z = -\sqrt{\frac{2}{3}} \tilde{k}_x - \frac{1}{\sqrt{3}} \tilde{k}_z$.

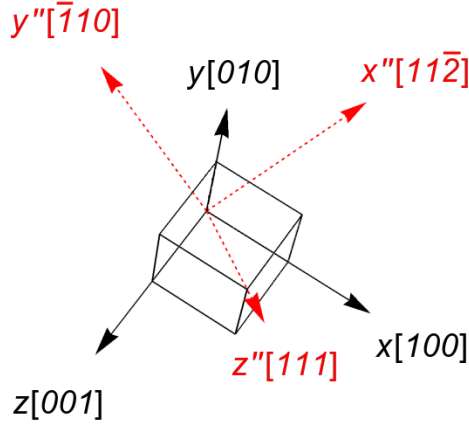


Figure 6: Representation of the new coordinate axis in the old frame of reference. We are rotating the $[001]$ to the $[111]$, i. e., we want the \hat{z} direction to be transformed to \hat{z}' .

Source: By the author.

Expliciting this rotation we end up (again only showing the modified terms), with:

$$H_{vc'} = Q_0 \begin{pmatrix} -\frac{k_z}{\sqrt{3}} & \frac{k_-}{3} & \frac{\sqrt{2}}{3}k_+ & 0 & -\frac{k_-}{3\sqrt{2}} & -\frac{2}{3}k_+ \\ \frac{k_+}{3} & \frac{k_z}{\sqrt{3}} & 0 & \frac{\sqrt{2}}{3}k_+ & -\sqrt{\frac{2}{3}}k_z & \frac{k_-}{\sqrt{6}} \\ \frac{\sqrt{2}}{3}k_- & 0 & \frac{k_z}{\sqrt{3}} & -\frac{1}{3}k_- & \frac{k_+}{\sqrt{6}} & \sqrt{\frac{2}{3}}k_z \\ 0 & \frac{\sqrt{2}}{3}k_- & -\frac{1}{3}k_+ & -\frac{k_z}{\sqrt{3}} & \frac{2k_-}{3} & -\frac{k_+}{3\sqrt{2}} \\ -\frac{k_+}{3\sqrt{2}} & -\sqrt{\frac{2}{3}}k_z & \frac{k_-}{\sqrt{6}} & \frac{2k_+}{3} & 0 & 0 \\ -\frac{2}{3}k_- & \frac{k_+}{\sqrt{6}} & \sqrt{\frac{2}{3}}k_z & -\frac{k_-}{3\sqrt{2}} & 0 & 0 \end{pmatrix} \quad (2.74)$$

and the terms of H_{vv} transforms to

$$\begin{aligned} Q &= -\gamma_1 k^2 + \gamma_3 (2k_z^2 - k_x^2 - k_y^2) \\ T &= -\gamma_1 k^2 - \gamma_3 (2k_z^2 - k_x^2 - k_y^2) \\ R &= \frac{k_-^2 (\gamma_2 + 2\gamma_3) + 2\sqrt{2}k_+ k_z (\gamma_3 - \gamma_2)}{\sqrt{3}} \\ S &= \sqrt{\frac{2}{3}} \left[\sqrt{2}k_- k_z (2\gamma_2 + \gamma_3) + k_+^2 (\gamma_3 - \gamma_2) \right]. \end{aligned} \quad (2.75)$$

To simplify the notation we also dropped the wave-vector tilde.

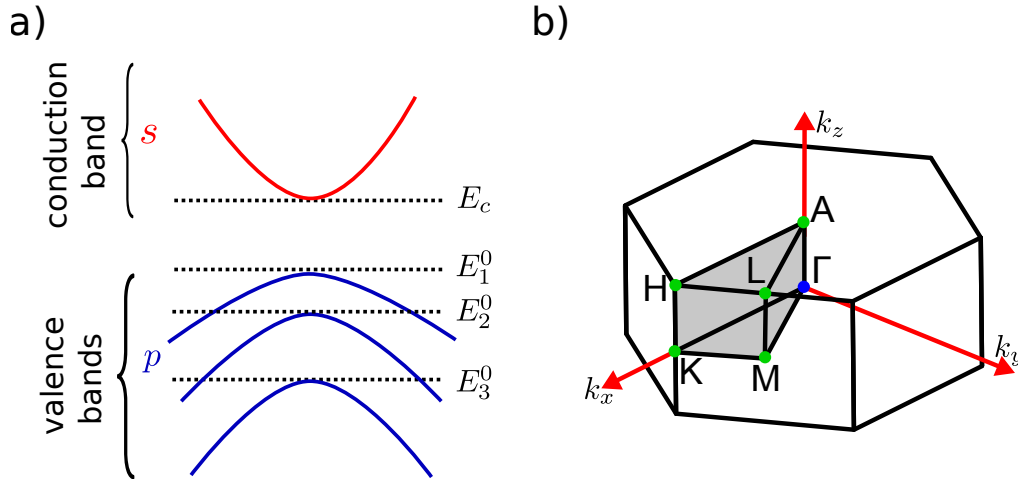


Figure 7: Bulk band scheme and first Brillouin zone for a wurtzite crystal. In a) we depict the 8 bands taken into account in the wurtzite model. In b) we show the Brillouin zone with the high symmetry points. The energy labels are, in the [Chuang & Chang¹⁴⁵](#) notation: $E_c = E_g + \Delta_1 + \Delta_2$, $E_1^0 = \Delta_1 + \Delta_2$, $E_2^0 = \frac{\Delta_1 - \Delta_2}{2} + \sqrt{\left(\frac{\Delta_1 - \Delta_2}{2}\right)^2 + 2\Delta_3^2}$ and $E_3^0 = \frac{\Delta_1 - \Delta_2}{2} - \sqrt{\left(\frac{\Delta_1 - \Delta_2}{2}\right)^2 + 2\Delta_3^2}$, where E_g is the gap energy, Δ_1 is the crystal field splitting (due to the distinction between z and xy) and Δ_2 and Δ_3 are the spin-orbit coupling energies.

Source: By the author.

2.4.2 Wurtzite model

Another very important crystal phase is the Wurtzite. Unlike zinc-blende, wurtzite has hexagonal symmetry, less symmetric than the cubic one, and therefore it will have more non-zero matrix elements in its description. The Kane-like 8-band $\mathbf{k} \cdot \mathbf{p}$ Hamiltonian which describes wurtzite was developed by [Chuang & Chang¹⁴⁵](#) in 1997, its scheme is depicted in Fig. 7a).

Usually III-V nitride compounds are the only ones that crystallizes as wurtzite in bulk form. However, with the appearance of a new type of nanostructure known as polytypical nanowires (or nanowiskers),^{107,170,171} large diameter nanowires where the heterostructure is formed along the wire's growth direction by changing the crystal phase (keeping the same compound) instead of changing the compound itself, it was possible to obtain other III-V compounds in the wurtzite crystal phase. To describe these polytypical nanowires, a hybrid $\mathbf{k} \cdot \mathbf{p}$ model was developed by the LFC group¹⁵¹ and later applied¹⁷² to accurately explain the absorption polarization in InP polytypical nanowires.¹⁷³

To improve upon the standard Kane-like description of wurtzite the LFC group

and colleagues¹⁴⁴ devised an extension of the 8-band $\mathbf{k} \cdot \mathbf{p}$ Hamiltonian which includes the often neglected^{108, 145–152} k dependent spin-orbit coupling term. Although this term slight modifies the energies at Γ , the general picture presented in Fig. 7a) still holds.

Table 2: Basis set, in the quasi-angular momentum representation, for the 8-band wurtzite $\mathbf{k} \cdot \mathbf{p}$ model.

Γ_9^v	$ c_1\rangle = -\frac{1}{\sqrt{2}} (X+iY)\uparrow\rangle$	$ c_4\rangle = \frac{1}{\sqrt{2}} (X-iY)\downarrow\rangle$
Γ_7^v	$ c_2\rangle = \frac{1}{\sqrt{2}} (X-iY)\uparrow\rangle$	$ c_5\rangle = -\frac{1}{\sqrt{2}} (X+iY)\downarrow\rangle$
$\Gamma_7^{\prime v}$	$ c_3\rangle = Z\uparrow\rangle$	$ c_6\rangle = Z\downarrow\rangle$
Γ_7^c	$ c_7\rangle = iS\uparrow\rangle$	$ c_8\rangle = iS\downarrow\rangle$

Source: Adapted from [FARIA JUNIOR et al.](#)¹⁴⁴

Using the basis set described in Table 2, the 8-band $\mathbf{k} \cdot \mathbf{p}$ Hamiltonian reads $H^{WZ} = H_0 + H_{SO}^{(1)} + H_{kp}^{(1)} + H_{kSO}^{(1)} + H_{kp}^{(2)}$. A more detailed description of the Hamiltonian can be found in Ref. 144, here we only show the matrix representation of each term.

H_0 is given by

$$H_0 = \text{diag} [\Delta_1, \Delta_1, 0, \Delta_1, \Delta_1, 0, E_c, E_c], \quad (2.76)$$

where Δ_1 is the crystal field splitting energy due to the anisotropy between the xy plane and the z direction and E_c is the energy of the conduction band.

The first order spin-orbit term is

$$H_{SO}^{(1)} = \begin{pmatrix} \Delta_1 + \Delta_2 & 0 & 0 & 0 & 0 & 0 & 0 & 0 \\ 0 & \Delta_1 - \Delta_2 & 0 & 0 & 0 & \sqrt{2}\Delta_3 & 0 & i\sqrt{2}\Delta_4 \\ 0 & 0 & 0 & 0 & \sqrt{2}\Delta_3 & 0 & 0 & 0 \\ 0 & 0 & 0 & \Delta_1 + \Delta_2 & 0 & 0 & 0 & 0 \\ 0 & 0 & \sqrt{2}\Delta_3 & 0 & \Delta_1 - \Delta_2 & 0 & i\sqrt{2}\Delta_4 & 0 \\ 0 & \sqrt{2}\Delta_3 & 0 & 0 & 0 & 0 & 0 & 0 \\ 0 & 0 & 0 & 0 & -i\sqrt{2}\Delta_4 & 0 & 0 & 0 \\ 0 & -i\sqrt{2}\Delta_4 & 0 & 0 & 0 & 0 & 0 & 0 \end{pmatrix}. \quad (2.77)$$

The first order $\mathbf{k} \cdot \mathbf{p}$ term is

$$H_{kp}^{(1)} = \begin{pmatrix} 0 & 0 & -iA_7k_- & 0 & 0 & 0 & -\frac{P_2k_-}{\sqrt{2}} & 0 \\ 0 & 0 & iA_7k_+ & 0 & 0 & 0 & \frac{P_2k_+}{\sqrt{2}} & 0 \\ iA_7k_+ & -iA_7k_- & 0 & 0 & 0 & 0 & P_1k_z & 0 \\ 0 & 0 & 0 & 0 & 0 & iA_7k_+ & 0 & \frac{P_2k_+}{\sqrt{2}} \\ 0 & 0 & 0 & 0 & 0 & -iA_7k_- & 0 & -\frac{P_2k_-}{\sqrt{2}} \\ 0 & 0 & 0 & -iA_7k_- & iA_7k_+ & 0 & 0 & P_1k_z \\ -\frac{P_2k_+}{\sqrt{2}} & \frac{P_2k_-}{\sqrt{2}} & P_1k_z & 0 & 0 & 0 & 0 & 0 \\ 0 & 0 & 0 & \frac{P_2k_-}{\sqrt{2}} & -\frac{P_2k_+}{\sqrt{2}} & P_1k_z & 0 & 0 \end{pmatrix}. \quad (2.78)$$

The k dependent spin-orbit interaction is

$$H_{kSO}^{(1)} = \begin{pmatrix} 0 & 0 & -\frac{i\alpha_1k_-}{\sqrt{2}} & 0 & -i\alpha_2k_- & 0 & \frac{\beta_1k_-}{\sqrt{2}} & 0 \\ 0 & 0 & -\frac{i\alpha_1k_+}{\sqrt{2}} & -i\alpha_2k_- & 0 & i\sqrt{2}\alpha_1k_z & \frac{\beta_1k_+}{\sqrt{2}} & -\sqrt{2}\beta_1k_z \\ \frac{i\alpha_1k_+}{\sqrt{2}} & \frac{i\alpha_1k_-}{\sqrt{2}} & 0 & 0 & -i\sqrt{2}\alpha_1k_z & -i\alpha_3k_- & 0 & \beta_2k_- \\ 0 & i\alpha_2k_+ & 0 & 0 & 0 & \frac{i\alpha_1k_+}{\sqrt{2}} & 0 & -\frac{\beta_1k_+}{\sqrt{2}} \\ i\alpha_2k_+ & 0 & i\sqrt{2}\alpha_1k_z & 0 & 0 & \frac{i\alpha_1k_-}{\sqrt{2}} & -\sqrt{2}\beta_1k_z & -\frac{\beta_1k_-}{\sqrt{2}} \\ 0 & -i\sqrt{2}\alpha_1k_z & i\alpha_3k_+ & -\frac{i\alpha_1k_-}{\sqrt{2}} & -\frac{i\alpha_1k_+}{\sqrt{2}} & 0 & -\beta_2k_+ & 0 \\ \frac{\beta_1k_+}{\sqrt{2}} & \frac{\beta_1k_-}{\sqrt{2}} & 0 & 0 & -\sqrt{2}\beta_1k_z & -\beta_2k_- & 0 & -i\gamma_1k_- \\ 0 & -\sqrt{2}\beta_1k_z & \beta_2k_+ & -\frac{\beta_1k_-}{\sqrt{2}} & -\frac{\beta_1k_+}{\sqrt{2}} & 0 & i\gamma_1k_+ & 0 \end{pmatrix}, \quad (2.79)$$

and the second order $\mathbf{k} \cdot \mathbf{p}$ term,

$$H_{kp}^{(2)} = \begin{pmatrix} \lambda + \theta & -K^* & -H^* & 0 & 0 & 0 & T^\dagger & 0 \\ -K & \lambda + \theta & H & 0 & 0 & 0 & T & 0 \\ -H & H^* & \lambda & 0 & 0 & 0 & U & 0 \\ 0 & 0 & 0 & \lambda + \theta & -K & H & 0 & T \\ 0 & 0 & 0 & -K^* & \lambda + \theta & -H^* & 0 & T^\dagger \\ 0 & 0 & 0 & H^* & -H & \lambda & 0 & U \\ T & T^\dagger & U^\dagger & 0 & 0 & 0 & V & 0 \\ 0 & 0 & 0 & T^\dagger & T & U^\dagger & 0 & V \end{pmatrix}, \quad (2.80)$$

with them matrix elements given by

$$\begin{aligned}
\lambda &= A_1 k_z^2 + A_2 (k_x^2 + k_y^2) \\
\theta &= A_3 k_z^2 + A_4 (k_x^2 + k_y^2) \\
K &= A_5 k_+^2 \\
H &= A_6 k_+ k_z \\
V &= e_1 k_z^2 + e_2 (k_x^2 + k_y^2) \\
T &= i B_3 k_+ k_z \\
U &= i [B_1 k_z^2 + B_2 (k_x^2 + k_y^2)].
\end{aligned} \tag{2.81}$$

Unlike zinc-blend, wurtzite has two effective masses, one in the z direction and other in the xy plane, given by

$$\begin{aligned}
m_z &= e_1 + \frac{P_1^2}{E_c} - \frac{2\beta_1^2}{\Delta_1 - \Delta_2 - E_c} + \frac{2\Delta_2^4 (A_1 + A_3)}{(\Delta_1 - \Delta_2 - E_c)^2} \\
&\quad - \frac{4B_1 \Delta_3 \Delta_4}{E_c (\Delta_1 - \Delta_2 - E_c)} + \frac{4\beta_1 \Delta_3 P_1}{E_c (\Delta_1 - \Delta_2 - E_c)} + \frac{4\alpha_1 \Delta_4 P_1}{E_c (\Delta_1 - \Delta_2 - E_c)} \tag{2.82}
\end{aligned}$$

and

$$\begin{aligned}
m_{xy} &= e_2 + \frac{(P_2 + \beta_1)^2}{2(E_c - \Delta_1 + \Delta_2)} + \frac{(P_2 - \beta_1)^2}{2(E_c - \Delta_1 - \Delta_2)} + \frac{\beta_2^2}{E_c} \frac{2\Delta_2^4 (A_2 + A_4)}{(\Delta_1 - \Delta_2 - E_c)^2} \\
&\quad + \frac{2\alpha_2 \beta_1 \Delta_4}{(\Delta_1 - \Delta_2 - E_c)(\Delta_1 + \Delta_2 - E_c)} + \frac{2\beta_1 \beta_2 \Delta_3}{E_c (\Delta_1 - \Delta_2 - E_c)} + \frac{2\alpha_1 \beta_2 \Delta_4}{E_c (\Delta_1 - \Delta_2 - E_c)} \\
&\quad + \frac{2\sqrt{2} A_7 \beta_2 \Delta_4}{E_c (\Delta_1 - \Delta_2 - E_c)} - \frac{4B_2 \Delta_3 \Delta_4}{E_c (\Delta_1 - \Delta_2 - E_c)} + \frac{2\beta_1 \Delta_4 \gamma_1}{(\Delta_1 - \Delta_2 - E_c)^2} \\
&\quad - \frac{2\alpha_2 \Delta_4 P_2}{(\Delta_1 + \Delta_2 - E_c)(\Delta_1 - \Delta_2 - E_c)} + \frac{2\beta_2 \Delta_3 P_2}{E_c (\Delta_1 - \Delta_2 - E_c)} + \frac{2\Delta_4 \gamma_1 P_2}{(\Delta_1 - \Delta_2 - E_c)^2} \tag{2.83}
\end{aligned}$$

Since the basis set for wurtzite does not diagonalize the spin-orbit coupling at $\vec{k} = 0$, the Landè g-factor does not have a nice formula like in zinc-blend and the best way is to compute it numerically by the Hamiltonian, nevertheless in Refs. 75 and 149 they provide a formula for the g-factor in both directions, z and xy plane, which depends on the off-diagonal spin-orbit coupling parameters.

2.4.2.1 $[11\bar{2}0]$ and $[10\bar{1}0]$ directions

Following the same prescription as in subsections 2.4.1.1 and 2.4.1.2, we now rotate the wurtzite Hamiltonian from the $[0001]$ to the $[11\bar{2}0]$ and $[10\bar{1}0]$ directions.¹³⁹ In Fig. 7b) we presented the first Brillouin zone for wurtzite with the high symmetry points. The rotation to $[11\bar{2}0]$ aims to point the \hat{z} axis along $\Gamma - M$ direction, and the rotation to $[10\bar{1}0]$ along the $\Gamma - K$ direction. One peculiarity of this Hamiltonians is that since we are treating points very near the Γ -point and both and despite being distinct directions, the final rotated Hamiltonian, however, is equal for both directions.

The angles that rotates from the $[0001]$ to the $[11\bar{2}0]$ direction are $\theta = \frac{\pi}{2}$ and $\phi = 0$. Therefore the rotation matrix is given by

$$U = \begin{bmatrix} 0 & 0 & -1 \\ 0 & 1 & 0 \\ 1 & 0 & 0 \end{bmatrix} \quad (2.84)$$

with the coordinate axis given in Fig. 8.

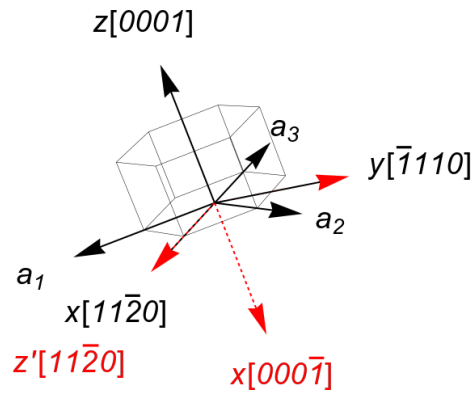


Figure 8: Representation of the new coordinate axis in the old frame of reference. We are rotating the $[0001]$ to the $[11\bar{2}0]$, i. e., we want the \hat{z} direction to be transformed to \hat{z}' .

Source: By the author.

The angles that rotates from the $[0001]$ to the $[10\bar{1}0]$ direction are $\theta = \frac{\pi}{2}$ and

and the wave-vector transformation are $k_x \rightarrow \tilde{k}_z$, $k_y \rightarrow \tilde{k}_y$ and $k_z \rightarrow -\tilde{k}_x$ for the $[11\bar{2}0]$ direction; and $k_x \rightarrow -\frac{\tilde{k}_y}{2} + \frac{\sqrt{3}}{2}\tilde{k}_y$, $k_y \rightarrow \frac{\sqrt{3}}{2}\tilde{k}_y + \frac{\tilde{k}_z}{2}$ and $k_z \rightarrow -\tilde{k}_x$ for the $[10\bar{1}0]$ direction.

The terms to construct of the rotate wurtzite Hamiltonian \tilde{H}_{WZ} will follow. The band edge energies are given by

$$\tilde{H}_0 = \text{diag} \left[\frac{\Delta_1}{2} + \Delta_3, \frac{\Delta_1}{2} - \Delta_3, \Delta_1, \frac{\Delta_1}{2} + \Delta_3, \frac{\Delta_1}{2} - \Delta_3, \Delta_1, E_c, E_c \right], \quad (2.88)$$

and the first order spin-orbit coupling by

$$\tilde{H}_{SO}^{(1)} = \begin{pmatrix} 0 & \frac{\Delta_1}{2} & 0 & 0 & 0 & \frac{\Delta_2 - \Delta_3}{\sqrt{2}} & \frac{i\Delta_4}{\sqrt{2}} & 0 \\ \frac{\Delta_1}{2} & 0 & 0 & 0 & 0 & \frac{\Delta_2 + \Delta_3}{\sqrt{2}} & \frac{i\Delta_4}{\sqrt{2}} & 0 \\ 0 & 0 & 0 & \frac{\Delta_2 - \Delta_3}{\sqrt{2}} & \frac{\Delta_2 + \Delta_3}{\sqrt{2}} & 0 & 0 & i\Delta_4 \\ 0 & 0 & \frac{\Delta_2 - \Delta_3}{\sqrt{2}} & 0 & 0 & 0 & 0 & -\frac{i\Delta_4}{\sqrt{2}} \\ 0 & 0 & \frac{\Delta_2 + \Delta_3}{\sqrt{2}} & 0 & 0 & 0 & 0 & -\frac{i\Delta_4}{\sqrt{2}} \\ \frac{\Delta_2 - \Delta_3}{\sqrt{2}} & \frac{\Delta_2 + \Delta_3}{\sqrt{2}} & 0 & 0 & 0 & 0 & -i\Delta_4 & 0 \\ -\frac{i\Delta_4}{\sqrt{2}} & -\frac{i\Delta_4}{\sqrt{2}} & 0 & 0 & 0 & i\Delta_4 & 0 & 0 \\ 0 & 0 & -i\Delta_4 & \frac{i\Delta_4}{\sqrt{2}} & \frac{i\Delta_4}{\sqrt{2}} & 0 & 0 & 0 \end{pmatrix}, \quad (2.89)$$

and the first order $\mathbf{k} \cdot \mathbf{p}$ term by

$$\tilde{H}_{kp}^{(1)} = \begin{pmatrix} -\sqrt{2}A_7k_y & 0 & -iA_7k_z & 0 & 0 & 0 & \frac{-k_xP_1 + ik_yP_2}{\sqrt{2}} & 0 \\ 0 & \sqrt{2}A_7k_y & iA_7k_z & 0 & 0 & 0 & i\frac{(-ik_xP_1 + k_yP_2)}{\sqrt{2}} & 0 \\ iA_7k_z & -iA_7k_z & 0 & 0 & 0 & 0 & k_zP_2 & 0 \\ 0 & 0 & 0 & \sqrt{2}A_7k_y & 0 & 0 & \frac{-i(ik_xP_1 - k_yP_2)}{\sqrt{2}} & 0 \\ 0 & 0 & 0 & 0 & -\sqrt{2}A_7k_y & -iA_7k_z & \frac{-i(ik_xP_1 + k_yP_2)}{\sqrt{2}} & 0 \\ 0 & 0 & 0 & -iA_7k_z & iA_7k_z & 0 & 0 & k_zP_2 \\ \frac{i(ik_xP_1 - k_yP_2)}{\sqrt{2}} & \frac{-i(ik_xP_1 + k_yP_2)}{\sqrt{2}} & P_2k_z & 0 & 0 & 0 & 0 & 0 \\ 0 & 0 & 0 & \frac{i(-ik_xP_1 - k_yP_2)}{\sqrt{2}} & -\frac{k_xP_1 + ik_yP_2}{\sqrt{2}} & k_zP_2 & 0 & 0 \end{pmatrix}, \quad (2.90)$$

and the k -dependent spin-orbit coupling term by

$$\tilde{H}_{kSO}^{(1)} = \begin{pmatrix} -\frac{k_y}{2}(\alpha_2 + \alpha_3) & -\frac{k_y}{2}(\alpha_2 - \alpha_3) + ik_x\alpha_1 & 0 & -\frac{1}{2}ik_z(2\alpha_1 + \alpha_2 - \alpha_3) & -\frac{1}{2}ik_z(\alpha_2 + \alpha_3) & \frac{-i\alpha_1k_x - \alpha_1k_y}{\sqrt{2}} & \frac{\beta_1k_x - i\beta_2k_y}{\sqrt{2}} & \frac{k_z(\beta_2 - \beta_1)}{\sqrt{2}} \\ -\frac{k_y}{2}(\alpha_2 - \alpha_3) - ik_x\alpha_1 & -\frac{k_y}{2}(\alpha_2 + \alpha_3) & 0 & -\frac{1}{2}ik_z(\alpha_2 + \alpha_3) & \frac{1}{2}ik_z(2\alpha_1 - \alpha_2 + \alpha_3) & \frac{i\alpha_1k_x - \alpha_1k_y}{\sqrt{2}} & \frac{\beta_1k_x + i\beta_2k_y}{\sqrt{2}} & -\frac{k_z(\beta_1 + \beta_2)}{\sqrt{2}} \\ \frac{i}{2}(2\alpha_1 + \alpha_2 - \alpha_3)k_z & \frac{i}{2}(\alpha_2 + \alpha_3)k_z & -\alpha_2k_y & \frac{i\alpha_1k_x}{\sqrt{2}} & 0 & -i\alpha_2k_z & 0 & \beta_1k_- \\ \frac{i}{2}(\alpha_2 + \alpha_3)k_z & -\frac{i}{2}(2\alpha_1 - \alpha_2 + \alpha_3)k_z & -\frac{i\alpha_1k_x + \alpha_1k_y}{\sqrt{2}} & \frac{k_y}{2}(\alpha_2 + \alpha_3) & i\alpha_1k_x + \frac{k_y}{2}(\alpha_2 - \alpha_3) & 0 & \frac{k_z(\beta_2 - \beta_1)}{\sqrt{2}} & -\frac{\beta_1k_x - i\beta_2k_y}{\sqrt{2}} \\ \frac{\alpha_1(i k_x - k_y)}{\sqrt{2}} & -\frac{i\alpha_1k_x}{\sqrt{2}} & i\alpha_2k_z & 0 & \frac{k_y}{2}(\alpha_2 - \alpha_3) & \alpha_2k_y & -\beta_1k_+ & 0 \\ \frac{\beta_1k_x + i\beta_2k_y}{\sqrt{2}} & \frac{\beta_1k_x - i\beta_2k_y}{\sqrt{2}} & 0 & \frac{k_z(\beta_2 - \beta_1)}{\sqrt{2}} & -\frac{k_z(\beta_1 + \beta_2)}{\sqrt{2}} & -\beta_1k_+ & \gamma_1k_y & -i\gamma_1k_z \\ \frac{(\beta_2 - \beta_1)k_z}{\sqrt{2}} & -\frac{(\beta_1 + \beta_2)k_z}{\sqrt{2}} & \beta_1k_+ & -\frac{\beta_1k_x + i\beta_2k_y}{\sqrt{2}} & -\frac{\beta_1k_x + i\beta_2k_y}{\sqrt{2}} & P_2k_z & i\gamma_1k_z & -\gamma_1k_y \end{pmatrix}, \quad (2.91)$$

and the second order $\mathbf{k} \cdot \mathbf{p}$ term by

$$\tilde{H}_{kp}^{(2)} = \begin{pmatrix} H_{11} & -H_{21}^* & -H_{23}^* & 0 & 0 & 0 & T^* & 0 \\ -H_{21} & H_{22} & H_{23} & 0 & 0 & 0 & T & 0 \\ -H_{23} & H_{23}^* & H_{33} & 0 & 0 & 0 & U & 0 \\ 0 & 0 & 0 & H_{11} & -H_{21} & H_{23} & 0 & T \\ 0 & 0 & 0 & -H_{21}^* & H_{22} & -H_{23}^* & 0 & T^* \\ 0 & 0 & 0 & H_{23}^* & -H_{23} & H_{33} & 0 & U \\ T & T^* & U^* & 0 & 0 & 0 & V & 0 \\ 0 & 0 & 0 & T^* & T & U^* & 0 & V \end{pmatrix}, \quad (2.92)$$

with the matrix elements given by

$$\begin{aligned} H_{11} &= \lambda + \frac{\theta}{2} + \frac{K}{2} \\ H_{22} &= \lambda + \frac{\theta}{2} + \frac{K}{2} \\ H_{33} &= \lambda + \theta - K \\ H_{21} &= -\frac{\theta}{2} - \frac{K}{2} + i\sqrt{2}A_6k_xk_y \\ H_{23} &= i\sqrt{2}A_5k_yk_z + A_6k_xk_z \\ \lambda &= A_1k_x^2 + A_2(k_y^2 + k_z^2) \\ \theta &= A_3k_x^2 + A_4(k_y^2 + k_z^2) \\ K &= A_5(k_y^2 - k_z^2) \\ T &= \frac{-i[B_1k_x^2 + B_2(k_y^2 + k_z^2)] + \sqrt{2}B_3k_xk_y}{\sqrt{2}} \\ U &= -i\sqrt{2}B_3k_xk_z \\ E_c &= e_1k_x^2 + e_2(k_y^2 + k_z^2). \end{aligned} \quad (2.93)$$

To simplify the notation we dropped the wave-vector tilde.

2.5 Plane wave expansion

Going back to the problem described by Eq. (2.25), we can expand it carrying on the perturbation up to second order in the $\vec{P} \cdot \vec{\pi}$ and write its general form like

$$\sum_{\alpha}^A [K_{\alpha'\alpha}(\vec{r}) + V_{\alpha'\alpha}(\vec{r})] f_{\alpha}(\vec{r}) = E f_{\alpha'}(\vec{r}) \quad (2.94)$$

where

$$K_{\alpha'\alpha}(\vec{r}) = \frac{1}{2} \left[\vec{P} \cdot \vec{\pi}_{\alpha'\alpha}(\vec{r}) + \vec{\pi}_{\alpha'\alpha}(\vec{r}) \cdot \vec{P} \right] + \sum_{i,j}^{x,y,z} P_i D_{\alpha'\alpha}^{ij}(\vec{r}) P_j, \quad (2.95)$$

and

$$V_{\alpha'\alpha}(\vec{r}) = \delta_{\alpha'\alpha} \left[E_{\alpha}^{(0)}(\vec{r}) + V(\vec{r}) \right] + h_{\alpha'\alpha}^{\text{SO}}(\vec{r}) + H_{\alpha'\alpha}^{\text{Z}}(\vec{r}). \quad (2.96)$$

The effective mass tensor is

$$D_{ij}^{\xi,\eta}(\vec{r}) = \frac{1}{2} \sum_{\mu}^B \left(\frac{\pi_{l\mu}^{\xi} \pi_{\mu j}^{\eta} + \pi_{l\mu}^{\eta} \pi_{\mu j}^{\xi}}{\varepsilon - \varepsilon_{\mu}^{(0)}} \right) + \frac{\delta_{ij} \delta_{\xi\eta}}{2m}, \quad (2.97)$$

the spin-orbit coupling matrix element is

$$h_{\alpha'\alpha}^{\text{SO}}(\vec{r}) = \left[\frac{\hbar}{4m^2 c^2} (\nabla V(\vec{r}) \times \vec{p}) \cdot \sigma \right]_{\alpha'\alpha}, \quad (2.98)$$

the Zeeman spin-splitting is

$$H_{\alpha'\alpha}^{\text{Z}}(\vec{r}) = -\vec{\mu}_{\alpha'\alpha}(\vec{r}) \cdot \vec{B}, \quad (2.99)$$

with the effective Landè g-factor tensor given by

$$\vec{\mu}_{l_j}(\vec{r}) = -\mu_B \left\{ g S_{l_j} - im \sum_{\mu}^B \frac{\vec{\pi}_{l\mu} \times \vec{\pi}_{\mu j}}{\varepsilon - \varepsilon_{\mu}^{(0)}} \right\}. \quad (2.100)$$

In the above equations, we explicitly wrote all terms with a spatial dependence. The total wave function of the system is written as

$$\psi = \sum_n \frac{1}{\sqrt{N}} f_n(\vec{r}) u_{n,0}(\vec{r}), \quad (2.101)$$

where N is some normalization constant. We also should remember that for the general formulation, $\vec{P} = \vec{p} + e\vec{A}$ and $\vec{\pi} = \frac{\vec{p}}{m} - \frac{\hbar}{2m^2 c^2} \nabla V_0 \times \vec{S}$.

The system of coupled differential equations we have obtained, Eq. (2.94), does not have a general analytical solution. There are a lot of numerical methods capable

of solving this type of equation such as finite differences,^{174,175} finite elements¹⁷⁶ and spectral methods^{126,172,177–180} to cite a few. The solution of equations like Eq. (2.94) in real space could lead to spurious solutions.^{181–184} To avoid cumbersome fixes to the real space solvers, apply plane wave expansion, or the Fourier transformations, a spectral method. Plane waves form a closed basis set and, specially, its derivatives are also contained in the set itself. Since we are dealing with a set of coupled partial differential equations with second order derivatives the use of plane waves decouples the equations simplifying our calculations.

Given any spatial varying quantity, $O(\vec{r})$, its discrete Fourier transformation is written as

$$O(\vec{r}) = \sum_{K'} e^{i\vec{K}' \cdot \vec{r}} O_{\vec{K}'}. \quad (2.102)$$

Analyzing Eq. (2.94), we see that there are at least three terms to be expanded: $V^{\alpha'\alpha}(\vec{r})$, $\vec{\pi}^{\alpha'\alpha}(\vec{r})$ and $D_{\alpha'\alpha}^{ij}(\vec{r})$. Besides those, the envelope function also has to be expanded.¹²⁵ To expand it we introduce the super-cell concept. As the Bloch functions are periodic in the crystal lattice, the envelope functions will be in the new unitary cell defined by the heterostructure. Hence

$$\begin{aligned} f_{\alpha\vec{k}}(\vec{r}) &= e^{i\vec{k} \cdot \vec{r}} g_{\alpha}(\vec{r}) \\ &= e^{i\vec{k} \cdot \vec{r}} \sum_{\vec{K}} e^{i\vec{K} \cdot \vec{r}} g_{\alpha\vec{K}}(\vec{k}) \\ &= \sum_{\vec{K}} e^{i(\vec{k} + \vec{K}) \cdot \vec{r}} g_{\alpha\vec{K}}(\vec{k}). \end{aligned} \quad (2.103)$$

To fully consider the magnetic field effects one should consider from the beginning that $\vec{P} = \vec{p} + e\vec{A}$ and derive a system of equations describing both Landau levels and the orbital correction to the g-factor. In this thesis I'll be concerned with the g-factor for small enough magnetic fields where the Landau levels can be neglected. Therefore, the orbital corrections to the g-factor, see Eq. (2.99), can be calculated from perturbation theory.¹³² Nevertheless, applying (2.102) and (2.103) into (2.25), we get

$$\begin{aligned} E(\vec{k}) g_{\alpha\vec{K}}(\vec{k}) &= \sum_{\alpha}^A \sum_{\vec{K}'} \left\{ V_{\Delta\vec{K}}^{\alpha'\alpha} + \frac{\hbar}{2m_0} \vec{P}_{\Delta\vec{K}}^{\alpha'\alpha} \cdot [(\vec{k} + \vec{K}') + (\vec{k} + \vec{K})] \right. \\ &\quad + \sum_{l,m}^{x,y,z} \left[\hbar^2 (k_l + K_l) (k_m + K'_m) \gamma_{lm,\Delta\vec{K}}^{\alpha'\alpha} - i\hbar (k_l + K_l) R_{lm,\Delta\vec{K}}^{\alpha'\alpha} \right. \\ &\quad \left. \left. - i\hbar (k_m + K'_m) S_{lm,\Delta\vec{K}}^{\alpha'\alpha} + T_{lm,\Delta\vec{K}}^{\alpha'\alpha} \right] \right\} g_{\alpha\vec{K}'}(\vec{k}) \end{aligned} \quad (2.104)$$

with $V_{\Delta\vec{K}}^{\alpha'\alpha} = \delta_{\alpha'\alpha} E_{0,\Delta\vec{K}}^\alpha + \delta_{\alpha'\alpha} V_{\Delta\vec{K}} + h_{SO,\Delta\vec{K}}^{\alpha'\alpha} + H_{Z,\Delta\vec{K}}^{\alpha'\alpha}$, $R_{ij}^{\alpha'\alpha}(\vec{r}) = e D_{ij}^{\alpha'\alpha}(\vec{r}) A_j(\vec{r})$, $S_{ij}^{\alpha'\alpha}(\vec{r}) = e A_i(\vec{r}) D_{ij}^{\alpha'\alpha}(\vec{r})$ and $T_{ij}^{\alpha'\alpha}(\vec{r}) = e^2 A_i(\vec{r}) D_{ij}^{\alpha'\alpha}(\vec{r}) A_j(\vec{r})$

In its final form the expanded Hamiltonian, given by Eq. (2.104), is constructed using the $\Delta\vec{K} = \vec{K} - \vec{K}'$, where \vec{K} varies according to Eq. (2.105). Hence, for a given number of plane waves, (NPW), our potential in the real space will be discretized using $4 \times \text{NPW} + 1$ and the envelope functions using $2 \times \text{NPW} + 1$. The Fourier expansion coefficients and the momenta relates to the size of the system as given bellow

$$\{K_j, K'_j\} = n_j \frac{2\pi}{L_j}, \quad -\frac{\pi}{L_j} \leq k_j \leq \frac{\pi}{L_j}, \quad j = x, y, z. \quad (2.105)$$

2.5.1 g-factor in the envelope function approximation and plane wave expansion

Now that we know how the g-factor appear in the $\mathbf{k} \cdot \mathbf{p}$ formalism, lets further generalize it and show how to compute the g-factors in a generic heterostructure under the envelope function approximation and the plane wave expansion.

Suppose the following Schrödinger equation

$$(H_C + H_B) \Psi(\vec{r}) = E \Psi(\vec{r}) \quad (2.106)$$

with

$$H_C = \frac{p^2}{2m_0} + V(\vec{r}) + \frac{\hbar}{4m_0^2 c^2} [\vec{\nabla} V(\vec{r}) \times \vec{p}] \cdot \vec{\sigma} \quad (2.107)$$

and

$$H_B = \frac{\mu_B}{2} \vec{B} \cdot \left[\frac{2}{\hbar} (\vec{r} \times \vec{\pi}) + g_0 \vec{\sigma} \right] \quad (2.108)$$

where H_C is the crystal Hamiltonian with spin-orbit coupling and H_B is the magnetic field Hamiltonian. Latter in this section we show that the Eq. (2.108) leads into Eq. (2.49).

Suppose now that we know the solutions to the problem without magnetic field, i. e., $H_C |n, \vec{k}\rangle = E_n(\vec{k}) |n, \vec{k}\rangle$. Specifically, lets assume that we are only interested in the solution at Γ -point. Therefore we shorten out notatio to $H_C |n\rangle = E_n |n\rangle$. Since we are dealing with confined systems in general, being quantum wells, wires or dots, we can write

$|n\rangle$ as

$$\begin{aligned} |n\rangle &= \sum_{\alpha} |F_{\alpha,n}, \alpha\rangle \\ \langle \vec{r} | F_l, l \rangle &= f_{l,n}(\vec{r}) u_{l,\Gamma}(\vec{r}) \end{aligned} \quad (2.109)$$

Let's then write H_B in the basis of the diagonalized problem, i. e., the set of $|F_{\alpha,n}, \alpha\rangle$ functions

$$\begin{aligned} \langle F_{n,\alpha}, \alpha | H_B | F_{m,\beta}, \beta \rangle &= \left\langle F_{n,\alpha}, \alpha \left| \frac{\mu_B}{2} \vec{B} \cdot \left[\frac{2}{\hbar} (\vec{r} \times \vec{\pi}) + g_0 \vec{\sigma} \right] \right| F_{m,\beta}, \beta \right\rangle \\ &= \frac{\mu_B}{2} \vec{B} \cdot \left[g_0 \langle F_{n,\alpha}, \alpha | \vec{\sigma} | F_{m,\beta}, \beta \rangle \right. \\ &\quad \left. + \frac{2}{\hbar} \langle F_{n,\alpha}, \alpha | (\vec{r} \times \vec{\pi}) | F_{m,\beta}, \beta \rangle \right] \end{aligned} \quad (2.110)$$

We have now to consider the following matrix elements: $\langle F_{n,\alpha}, \alpha | (\vec{r} \times \vec{\pi}) | F_{m,\beta}, \beta \rangle$ and $\langle F_{n,\alpha}, \alpha | \vec{\sigma} | F_{m,\beta}, \beta \rangle$. The second matrix element expands to:

$$\begin{aligned} \langle F_{n,\alpha}, \alpha | \vec{\sigma} | F_{m,\beta}, \beta \rangle &= \sum_{\alpha,\beta}^{\text{basiset}} \int d^3r f_{n,\alpha}^*(\vec{r}) u_{\alpha,\Gamma}^*(\vec{r}) \vec{\sigma} f_{m,\beta}(\vec{r}) u_{\beta,\Gamma}(\vec{r}) \\ &= \sum_{\alpha,\beta} \int d^3r f_{n,\alpha}^*(\vec{r}) f_{m,\beta}(\vec{r}) u_{\alpha,\Gamma}^*(\vec{r}) \vec{\sigma} u_{\beta,\Gamma}(\vec{r}) \\ &= \sum_{\alpha,\beta} \left[\int d^3r f_{n,\alpha}^*(\vec{r}) f_{m,\beta}(\vec{r}) \right] \langle \alpha | \vec{\Sigma} | \beta \rangle \\ &= \sum_{\alpha,\beta} M_{n,m,\vec{k}}^{\alpha,\beta} \langle \alpha | \vec{\Sigma} | \beta \rangle \end{aligned} \quad (2.111)$$

where $M_{n,m,\vec{k}}^{\alpha,\beta} = \int d^3r f_{n,\alpha}^*(\vec{r}) f_{m,\beta}(\vec{r})$ is the overlap integral between the envelope functions of states n and m for different basis states α and β .

Remember that, or, using Heisenberg equation of motion,

$$\begin{aligned} [\vec{r}, H_C] &= i\hbar \left\{ \frac{1}{m_0} \vec{p} + \frac{\hbar}{4m_0^2 c^2} [\vec{\sigma} \times \vec{\nabla} V(\vec{r})] \right\} \\ &= \frac{i\hbar}{m_0} \vec{\pi} \end{aligned} \quad (2.112)$$

Therefore,

$$\begin{aligned} \langle F_{n,\alpha}, \alpha | [\vec{r}, H_C] | F_{m,\beta}, \beta \rangle &= \langle F_{n,\alpha}, \alpha | \vec{r} H_C - H_C \vec{r} | F_{m,\beta}, \beta \rangle \\ &= (E_m - E_n) \langle F_{n,\alpha}, \alpha | \vec{r} | F_{m,\beta}, \beta \rangle \\ &= \frac{i\hbar}{m_0} \langle F_{n,\alpha}, \alpha | \vec{\pi} | F_{m,\beta}, \beta \rangle \end{aligned} \quad (2.113)$$

which gives us

$$\langle F_{n,\alpha}, \alpha | \vec{r} | F_{m,\beta}, \beta \rangle = \frac{\hbar}{im_0} \frac{\langle F_{n,\alpha}, \alpha | \vec{\pi} | F_{m,\beta}, \beta \rangle}{(E_n - E_m)} \quad (2.114)$$

and if we substitute back into Eq. (2.110) we recover the expression given by Eq. (2.49), but in the envelope function approximation.

Finally, we can write a term, labeled here as a were $a, b, c \in x, y, z$, of the matrix element $\langle F_{n,\alpha}, \alpha | (\vec{r} \times \vec{\pi})_a | F_{m,\beta}, \beta \rangle$, as

$$\begin{aligned} \langle F_{n,\alpha}, \alpha | (\vec{r} \times \vec{\pi})_a | F_{m,\beta}, \beta \rangle &= \langle F_{n,\alpha}, \alpha | b\pi_c - c\pi_b | F_{m,\beta}, \beta \rangle \\ &= \langle F_{n,\alpha}, \alpha | b\pi_c | F_{m,\beta}, \beta \rangle - \langle F_{n,\alpha}, \alpha | c\pi_b | F_{m,\beta}, \beta \rangle \\ &= \left\langle F_{n,\alpha}, \alpha \left| b \left(\sum_l |F_{l,\gamma}, \gamma\rangle \langle F_{l,\gamma}, \gamma| \right) \pi_c \right| F_{m,\beta}, \beta \right\rangle \\ &\quad - \left\langle F_{n,\alpha}, \alpha \left| c \left(\sum_l |F_{l,\gamma}, \gamma\rangle \langle F_{l,\gamma}, \gamma| \right) \pi_b \right| F_{m,\beta}, \beta \right\rangle \\ &= \sum_l (\langle F_{n,\alpha}, \alpha | b | F_{l,\gamma}, \gamma\rangle \langle F_{l,\gamma}, \gamma | \pi_c | F_{m,\beta}, \beta \rangle \\ &\quad - \langle F_{n,\alpha}, \alpha | c | F_{l,\gamma}, \gamma\rangle \langle F_{l,\gamma}, \gamma | \pi_b | F_{m,\beta}, \beta \rangle) \\ &= \frac{\hbar}{im_0} \sum_l' \frac{1}{E_n - E_l} (\langle F_{n,\alpha}, \alpha | \pi_b | F_{l,\gamma}, \gamma\rangle \langle F_{l,\gamma}, \gamma | \pi_c | F_{m,\beta}, \beta \rangle \\ &\quad - \langle F_{n,\alpha}, \alpha | \pi_c | F_{l,\gamma}, \gamma\rangle \langle F_{l,\gamma}, \gamma | \pi_b | F_{m,\beta}, \beta \rangle) \end{aligned} \quad (2.115)$$

where the $'$ means that the energy denominator cannot be zero.

We also can write

$$\begin{aligned} \langle F_{n,\alpha}, \alpha | (\vec{r} \times \vec{\pi})_a | F_{m,\beta}, \beta \rangle &= \frac{\hbar}{im_0} \sum_l' \frac{1}{E_l - E_m} (\langle F_{n,\alpha}, \alpha | \pi_c | F_{l,\gamma}, \gamma\rangle \langle F_{l,\gamma}, \gamma | \pi_b | F_{m,\beta}, \beta \rangle \\ &\quad - \langle F_{n,\alpha}, \alpha | \pi_b | F_{l,\gamma}, \gamma\rangle \langle F_{l,\gamma}, \gamma | \pi_c | F_{m,\beta}, \beta \rangle) \end{aligned} \quad (2.116)$$

hence, putting both together, we get

$$\begin{aligned} \langle F_{n,\alpha}, \alpha | (\vec{r} \times \vec{\pi})_a | F_{m,\beta}, \beta \rangle &= \frac{\hbar}{im_0} \frac{1}{2} \sum_l' (\langle F_{n,\alpha}, \alpha | \pi_b | F_{l,\gamma}, \gamma\rangle \langle F_{l,\gamma}, \gamma | \pi_c | F_{m,\beta}, \beta \rangle \\ &\quad - \langle F_{n,\alpha}, \alpha | \pi_c | F_{l,\gamma}, \gamma\rangle \langle F_{l,\gamma}, \gamma | \pi_b | F_{m,\beta}, \beta \rangle \times) \\ &\quad \left(\frac{1}{E_n - E_l} + \frac{1}{E_m - E_l} \right) \end{aligned} \quad (2.117)$$

Now we still have to substitute back the $\vec{\pi}$ operator to get a complete expression to the matrix element.

2.5.1.1 $\vec{\pi}$ matrix element

We have compute matrix elements of the form $\langle F_{n,\alpha}, \alpha | \vec{\pi} | F_{m,\beta}, \beta \rangle$, with $\vec{\pi} = \vec{p} + \frac{\hbar}{4m_0c^2} [\vec{\sigma} \times \vec{\nabla} V(\vec{r})]$. We begin by writing it as

$$\begin{aligned} \langle F_{n,\alpha}, \alpha | \vec{\pi} | F_{m,\beta}, \beta \rangle &= \left\langle F_{n,\alpha}, \alpha \left| \vec{p} + \frac{\hbar}{4m_0c^2} [\vec{\sigma} \times \vec{\nabla} V(\vec{r})] \right| F_{m,\beta}, \beta \right\rangle \\ &= \langle F_{n,\alpha}, \alpha | \vec{p} | F_{m,\beta}, \beta \rangle \\ &\quad + \left\langle F_{n,\alpha}, \alpha \left| \frac{\hbar}{4m_0c^2} [\vec{\sigma} \times \vec{\nabla} V(\vec{r})] \right| F_{m,\beta}, \beta \right\rangle \end{aligned} \quad (2.118)$$

First lets calculate $\langle F_{n,\alpha}, \alpha | \vec{p} | F_{m,\beta}, \beta \rangle$

$$\begin{aligned} \langle F_{n,\alpha}, \alpha | \vec{p} | F_{m,\beta}, \beta \rangle &= \sum_{\alpha,\beta}^{\text{basiset}} \int d^3r f_{n,\alpha}^*(\vec{r}) u_{\alpha,\Gamma}^*(\vec{r}) [(-i\hbar\vec{\nabla}) f_{m,\beta}(\vec{r}) u_{\beta,\Gamma}(\vec{r})] \\ &= -i\hbar \sum_{\alpha,\beta}^{\text{basiset}} \int d^3r [f_{n,\alpha}^*(\vec{r}) \vec{\nabla} f_{m,\beta}(\vec{r}) u_{\alpha,\Gamma}^*(\vec{r}) u_{\beta,\Gamma}(\vec{r}) \\ &\quad + f_{n,\alpha}^*(\vec{r}) f_{m,\beta}(\vec{r}) u_{\alpha,\Gamma}^*(\vec{r}) \vec{\nabla} u_{\beta,\Gamma}(\vec{r})] \\ &= -i\hbar \langle F_{n,\alpha} | \vec{\nabla} | F_{m,\alpha} \rangle + \sum_{\alpha,\beta} M_{n,m,\vec{k}}^{\alpha,\beta} P^{\alpha,\beta}(\vec{r}) \end{aligned} \quad (2.119)$$

Substituting back Eq. (2.119) into Eq. (2.117), we get

$$\begin{aligned} \langle F_{n,\alpha}, \alpha | (\vec{r} \times \vec{\pi})_a | F_{m,\beta}, \beta \rangle &= \frac{\hbar}{im_0} \frac{1}{2} \sum_l' [(\langle F_{n,\alpha}, \alpha | (\vec{r} \times \vec{\pi})_a | F_{m,\beta}, \beta \rangle \\ &\quad + \left\langle F_{n,\alpha}, \alpha \left| \frac{\hbar}{4m_0c^2} [\vec{\sigma} \times \vec{\nabla} V(\vec{r})] \right| F_{m,\beta}, \beta \right\rangle) \times \\ &\quad \left(-i\hbar\delta_{\gamma\beta} \langle F_{l,\gamma} | \partial_c | F_{m,\beta} \rangle + \sum_{\gamma,\beta} M_{l,m,\vec{k}}^{\gamma,\beta} P^{\gamma,\beta}(\vec{r}) \right. \\ &\quad \left. + \left\langle F_{n,\alpha}, \alpha \left| \frac{\hbar}{4m_0c^2} [\vec{\sigma} \times \vec{\nabla} V(\vec{r})] \right| F_{m,\beta}, \beta \right\rangle \right) \\ &\quad - \left(-i\hbar\delta_{\alpha\gamma} \langle F_{n,\alpha} | \partial_c | F_{l,\gamma} \rangle + \sum_{\alpha,\gamma} M_{n,l,\vec{k}}^{\alpha,\gamma} P^{\alpha,\gamma}(\vec{r}) \right. \\ &\quad \left. + \left\langle F_{n,\alpha}, \alpha \left| \frac{\hbar}{4m_0c^2} [\vec{\sigma} \times \vec{\nabla} V(\vec{r})] \right| F_{m,\beta}, \beta \right\rangle \right) \times \\ &\quad \left(-i\hbar\delta_{\gamma\beta} \langle F_{l,\gamma} | \partial_b | F_{m,\beta} \rangle + \sum_{\gamma,\beta} M_{l,m,\vec{k}}^{\gamma,\beta} P^{\gamma,\beta}(\vec{r}) \right. \\ &\quad \left. + \left\langle F_{n,\alpha}, \alpha \left| \frac{\hbar}{4m_0c^2} [\vec{\sigma} \times \vec{\nabla} V(\vec{r})] \right| F_{m,\beta}, \beta \right\rangle \right) \\ &\quad \times \left(\frac{1}{E_n - E_l} + \frac{1}{E_m - E_l} \right) \end{aligned} \quad (2.120)$$

Numerically, the terms $\sum_{\alpha,\gamma} M_{n,l,\vec{k}}^{\alpha,\gamma} P^{\alpha,\gamma}(\vec{r}) + \left\langle F_{n,\alpha}, \alpha \left| \frac{\hbar}{4m_0c^2} [\vec{\sigma} \times \vec{\nabla} V(\vec{r})] \right| F_{m,\beta}, \beta \right\rangle$ are computed by constructing the (Fourier) expanded Hamiltonian, with the interband

coupling parameters and spin-orbit coupling, setting $\vec{k} = 1$ and multiplying the n, m, l states.

Now, what is left to do is to compute the matrix elements of the form $-i\hbar \langle F_{n,\alpha} | \vec{\nabla} | F_{m,\alpha} \rangle$. To numerically achieve this, we recall that $\langle \vec{r} | F_{m,\alpha} \rangle = f_{m,\alpha}(\vec{r})$ and it is expressed as the Fourier transformed function, see Eq. (2.103),

$$f_{m,\alpha}(\vec{r}) = \sum_{\vec{K}} e^{i(\vec{k}+\vec{K})\cdot\vec{r}} g_{m,\alpha}^{\vec{K}}(\vec{k}) \quad (2.121)$$

Therefore, the derivative becomes

$$\begin{aligned} -i\hbar \vec{\nabla} f_{m,\alpha}(\vec{r}) |_{\vec{k}=0} &= -i\hbar \vec{\nabla} \left(\sum_{\vec{K}} e^{i\vec{K}\cdot\vec{r}} g_{m,\alpha}^{\vec{K}} \right) \\ &= \hbar \vec{K} \sum_{\vec{K}} e^{i\vec{K}\cdot\vec{r}} g_{m,\alpha}^{\vec{K}} \\ &= \hbar \vec{K} f_{m,\alpha}(\vec{r}) \end{aligned} \quad (2.122)$$

and the matrix element is written as

$$\begin{aligned} -i\hbar \langle F_{n,\alpha} | \vec{\nabla} | F_{m,\alpha} \rangle &= \hbar \vec{K} \langle F_{n,\alpha} | F_{m,\alpha} \rangle \\ &= \hbar \vec{K} \sum_{\alpha} \int d^3r f_{n,\alpha}^*(\vec{r}) f_{m,\alpha}(\vec{r}) \\ &= \hbar \vec{K} M_{n,m,\vec{k}}^{\alpha,\alpha} \end{aligned} \quad (2.123)$$

Substituting back into Eq. (2.120), we get

$$\begin{aligned}
\langle F_{n,\alpha}, \alpha | (\vec{r} \times \vec{\pi})_a | F_{m,\beta}, \beta \rangle = & \frac{\hbar}{im_0} \frac{1}{2} \sum_l' \left[\left(\hbar K_b M_{n,m,\vec{k}}^{\alpha,\alpha} + \sum_{\alpha,\gamma} M_{n,l,\vec{k}}^{\alpha,\gamma} P^{\alpha,\gamma}(\vec{r}) \right. \right. \\
& + \left. \left. \left\langle F_{n,\alpha}, \alpha \left| \frac{\hbar}{4m_0c^2} [\vec{\sigma} \times \vec{\nabla} V(\vec{r})] \right| F_{m,\beta}, \beta \right\rangle \right) \times \right. \\
& \left(\hbar K_c M_{n,m,\vec{k}}^{\gamma,\gamma} + \sum_{\gamma,\beta} M_{l,m,\vec{k}}^{\gamma,\beta} P^{\gamma,\beta}(\vec{r}) \right. \\
& + \left. \left. \left\langle F_{n,\alpha}, \alpha \left| \frac{\hbar}{4m_0c^2} [\vec{\sigma} \times \vec{\nabla} V(\vec{r})] \right| F_{m,\beta}, \beta \right\rangle \right) \\
& - \left(\hbar K_c M_{n,m,\vec{k}}^{\alpha,\alpha} + \sum_{\alpha,\gamma} M_{n,l,\vec{k}}^{\alpha,\gamma} P^{\alpha,\gamma}(\vec{r}) \right. \\
& + \left. \left. \left\langle F_{n,\alpha}, \alpha \left| \frac{\hbar}{4m_0c^2} [\vec{\sigma} \times \vec{\nabla} V(\vec{r})] \right| F_{m,\beta}, \beta \right\rangle \right) \times \\
& \left(\hbar K_b M_{n,m,\vec{k}}^{\gamma,\gamma} + \sum_{\gamma,\beta} M_{l,m,\vec{k}}^{\gamma,\beta} P^{\gamma,\beta}(\vec{r}) \right. \\
& + \left. \left. \left\langle F_{n,\alpha}, \alpha \left| \frac{\hbar}{4m_0c^2} [\vec{\sigma} \times \vec{\nabla} V(\vec{r})] \right| F_{m,\beta}, \beta \right\rangle \right) \Big] \\
& \times \left(\frac{1}{E_n - E_l} + \frac{1}{E_m - E_l} \right) \tag{2.124}
\end{aligned}$$

Summarizing, the g-factor tensor at a given set of states n, m can be computed via Eq. (2.110) using expressions (2.111) and (2.117) with the last one being further expanded to Eq. (2.124).

2.6 Effective spin-orbit coupling model

Focusing on the conduction band, we can derive an effective two band $\mathbf{k} \cdot \mathbf{p}$ model that captures the effects of the coupling with the remote bands. Such model is easy to understand and solve giving a fairly accurate description of the system. However some of its parameters are not easy readable from fitting ab initio band structures and have to be extracted from convoluted experiments. On the other hand, one could carry out Löwding partitioning but now with the conduction band as the class A and the rest of the bands (of the specific $\mathbf{k} \cdot \mathbf{p}$ model) as class B.

The effective 2×2 Hamiltonian for the CB band for bulk like systems is written as

$$H = H_0 + H_{\text{BIA}} + H_{\text{SIA}}. \tag{2.125}$$

Further details of its derivation can be found in Refs. 132 and 67. Here, H_0 is the effective mass Hamiltonian, expressing the parabolic dispersion near Γ -point. The remaining

two terms express the bulk-inversion (BIA) and structure-inversion (SIA) asymmetry induced spin-orbit couplings. For conduction electrons, these spin-orbit Hamiltonians are conventionally written as

$$H_{\text{BIA}} = \frac{\hbar}{2} \vec{\Omega}_{\text{BIA}} \cdot \vec{\sigma}, \quad (2.126)$$

and

$$H_{\text{SIA}} = \frac{\hbar}{2} \vec{\Omega}_{\text{SIA}} \cdot \vec{\sigma}. \quad (2.127)$$

Here, $\vec{\Omega}$ is the corresponding momentum-dependent spin-orbit field. Time reversal symmetry requires it to be an odd function of momentum, $\vec{\Omega}(\vec{k}) = -\vec{\Omega}(-\vec{k})$. Otherwise, the functional form of the spin-orbit field is restricted by the crystal and confinement symmetry. Each structure has its own functional form of the effective mass and spin-orbit fields, based on symmetry.

2.6.1 Zinc-blende BIA fields

The spin-orbit splitting of the conduction bands in zinc-blende InSb nanowires can be qualitatively discussed using the Dresselhaus results for spin-orbit coupling in zinc-blende III-V semiconductors. For this case, Dresselhaus found that

$$\vec{\Omega}_{\text{BIA}} = \gamma \left[k_x (k_y^2 - k_z^2), k_y (k_z^2 - k_x^2), k_z (k_x^2 - k_y^2) \right], \quad (2.128)$$

meaning that the spin-orbit splitting of conduction band is increasing as a cubic power of the momentum, away from Γ -point. There is no linear in momentum splitting for bulk III-V's. Next we analyze the specifics for each growth direction.

In Fig. 10a) we show the spherical plot of Eq. (2.128), and in Fig. 10b) its vector field representation. We see that field vanished for [001] and [111] directions (and their equivalents). In the vector field representation we clearly see the vortices along [111], and saddle points along [001], indicating the spin-orbit fields in the quantum well grown along these orientations.^{9,67,185}

Applying the rotation described in previous section, we obtain the spin-orbit field for [001] and [111] direction.¹⁸⁶ For [001], it is written as

$$\vec{\Omega}_{\text{BIA}} = \frac{\gamma}{2} \left[-4k_x k_y k_z, k_z (2k_x^2 - k_z^2 + k_y^2), k_y (2k_x^2 + k_z^2 - k_y^2) \right], \quad (2.129)$$

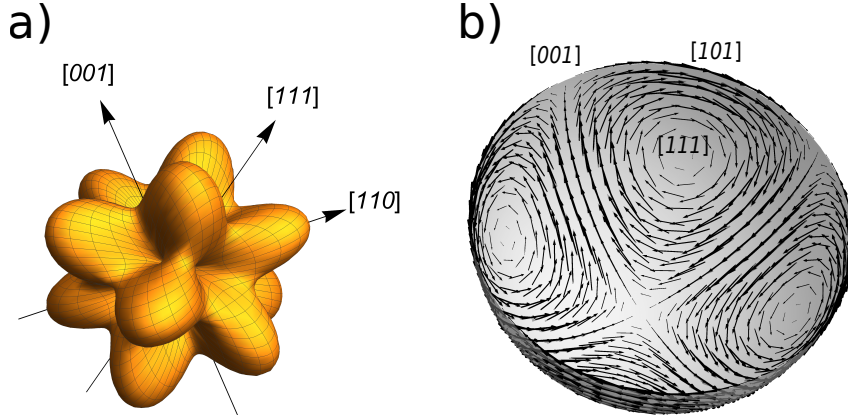


Figure 10: Spin-orbit coupling field. a) Spherical plot of the magnitude of the Dresselhaus spin-orbit field in the momentum space. b) Dresselhaus vector field over the Fermi sphere.

Source: By the author.

whereas for [111] it is written as

$$\vec{\Omega}_{\text{BIA}} = \frac{\gamma}{\sqrt{6}} \left[-\frac{k_y (k_x^2 + k_y^2 + 2\sqrt{2}k_x k_z - 4k_z^2)}{\sqrt{2}}, \frac{k_y^2 (k_x + \sqrt{2}k_z) + k_x (k_x^2 - \sqrt{2}k_x k_z - 4k_z^2)}{\sqrt{2}}, -k_y (k_y^2 - 3k_x^2) \right], \quad (2.130)$$

2.6.2 Wurtzite BIA fields

The spin-orbit splitting of the conduction electrons in a bulk wurtzite III-V semiconductor is^{109,144,148,187}

$$\vec{\Omega}_{\text{BIA}} = \left[\alpha + \gamma (b k_z^2 - k_x^2 - k_y^2) \right] (k_y, -k_x, 0). \quad (2.131)$$

Hence the spin-orbit coupling is increasing as a linear and a cubic power of the momentum away from Γ -point.

In Fig. 11a) and 11c) we show the spherical plot of Eq. (2.131), and in Fig. 11b) and 11d) its vector field representation. The field vanishes for momenta along the hexagonal axis, [0001], that is for $k_x = k_y = 0$, as well as for momenta in the hyperboloid, $b k_z^2 = (k_x^2 + k_y^2 - \frac{\alpha}{\gamma})$, as seen in Fig. 11c). The spin-orbit field has cylindrical symmetry as shown in Fig. 11b) and 11d).

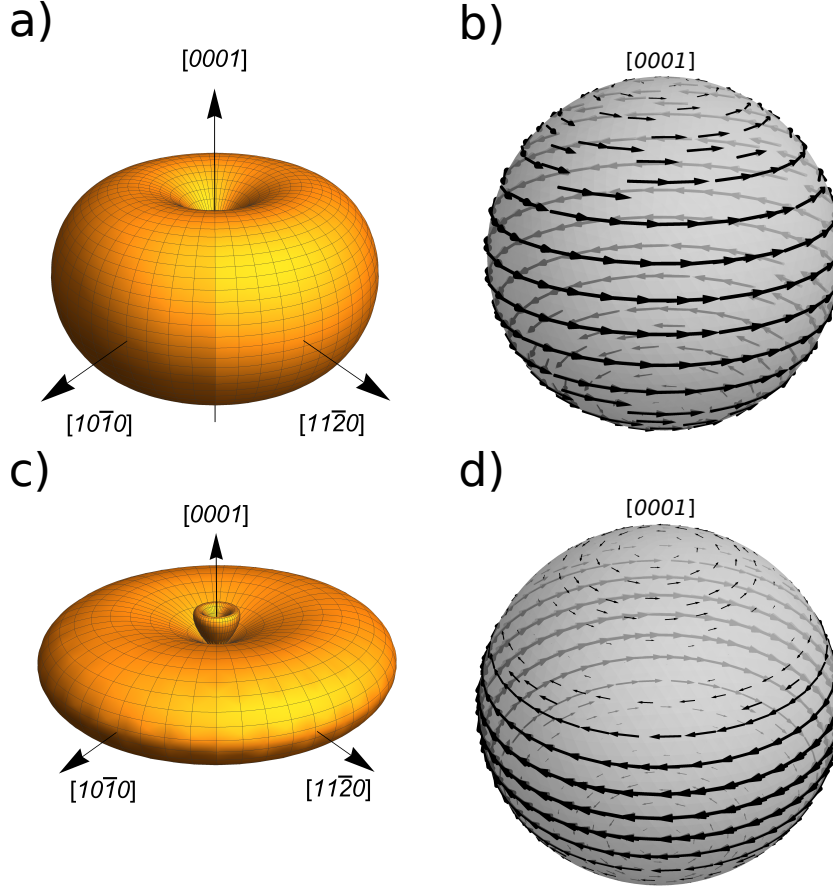


Figure 11: Spin-orbit coupling field. a,c) Spherical plot of the magnitude of the spin-orbit field in the momentum space for two distinct momenta k_a and k_c where $k_a > k_c$. b,d) Vector field over the Fermi sphere.

Source: By the author.

Applying the rotation described in previous section, we obtain the spin-orbit field for both $[11\bar{2}0]$ and $[10\bar{1}0]$ directions

$$\vec{\Omega}_{\text{BIA}} = \left[\alpha + \gamma (b k_x^2 - k_y^2 - k_z^2) \right] (0, -k_z, k_y). \quad (2.132)$$

2.6.3 Effective Hamiltonian and dispersion relation

The last term of equation (2.125) which remains to be analyzed is the H_0 , the term that describes the parabolic dispersion of the conduction electrons. For cubic crystals, as the zinc-blende, the electron effective mass is homogeneous in all directions and it is described by $\frac{1}{m^{\text{ZB}}} k^2$, therefore

$$H_{\text{M}}^{\text{ZB}} = \frac{\hbar^2}{2 m_0 \tilde{m}^{\text{ZB}}} (k_x^2 + k_y^2 + k_z^2), \quad (2.133)$$

where \tilde{m}^{ZB} is the electron effective mass, material dependent.

For wurtzite crystals the \hat{x} and \hat{y} direction are geometric distinct from \hat{z} , yielding different energy dispersions for each direction. For the perpendicular direction we get $\frac{1}{m_{\perp}^{\text{WZ}}} (k_x^2 + k_y^2)$ and for the parallel we get $\frac{1}{m_{\parallel}^{\text{WZ}}} k_z^2$, therefore

$$H_{\text{M}}^{\text{WZ}} = \left(\frac{\hbar^2}{2m_0} \right) \frac{1}{\tilde{m}_{\perp}^{\text{WZ}}} (k_x^2 + k_y^2) + \frac{1}{\tilde{m}_{\parallel}^{\text{WZ}}} k_z^2. \quad (2.134)$$

Although it is possible to devise Hamiltonians for confined systems being extreme careful to keep the operators ordering intact, one can imagine that it will be a challenging task. The principle is that one makes all the material specific parameters vary along \vec{r} and make the substitution $\vec{k} \rightarrow -i\vec{\nabla}$. The spatial variation of the gap parameters defines our confinement potential and there is also the extra external electric potential, $V_{\text{ele}}(\vec{r})$. Since we already have a powerful computational tool to obtain the energy spectrum for the full multiband Hamiltonian, instead, we chose to only care about the functional form of the H_{M} , H_{BIA} and H_{SIA} terms and apply a numerical fitting on the calculated data.

The Hamiltonian given by Eq. (2.125) is a good starting point to understand how the quantum confinement modifies the energy spectrum and ultimately the SOC of the nanowires's subbands. Modifying it to include quantum confinement is to make the terms spatially dependent and to include the indirect dependence on the external electric potential, hence

$$H(\vec{r}; V_{\text{ele}}) = H_{\text{M}}(\vec{r}; V_{\text{ele}}) + H_{\text{BIA}}(\vec{r}; V_{\text{ele}}) + H_{\text{SIA}}(\vec{r}; V_{\text{ele}}). \quad (2.135)$$

As the system is confined in the $x y$ -plane, we can write the wave function as

$$\langle \vec{r} | k_z, n, s \rangle = \frac{e^{ik_z z}}{N} \psi_{n,s}(x, y), \quad (2.136)$$

where k_z stands for the momentum in the free direction, $n = 0, 1, 2, \dots$, for the subband index and s for the pseudo-spin projection.

Focusing on the first subband, let us investigate how the quantum confinement changes the bulk parameters. We compute the matrix elements of Eq. (2.135) with respect to the first subband eigenstate $\langle \vec{r} | 0, 0, s \rangle$ at Γ -point, following similar description as Refs.

134 and 135,

$$\langle 0, 0, s | H(\vec{r}; V_{\text{ele}}) | 0, 0, s' \rangle. \quad (2.137)$$

For the BIA term, $V_{\text{ele}} = 0$, we obtain the following spin-orbit fields

$$\begin{aligned} \vec{\Omega}_{001}^{\text{ZB}} &= \gamma^{\text{ZB}} [0, 0, \beta_1^{\text{ZB}} k_z] \\ \vec{\Omega}_{110}^{\text{ZB}} &= \gamma^{\text{ZB}} \left[0, \frac{1}{2} k_z^3 - \beta_1^{\text{ZB}} k_z, 0 \right] \\ \vec{\Omega}_{111}^{\text{ZB}} &= -\sqrt{\frac{1}{6}} \gamma^{\text{ZB}} [0, \beta_1^{\text{ZB}} k_z, 0], \end{aligned} \quad (2.138)$$

for zinc-blende, where $\beta_1^{\text{ZB}} = \langle 0 | k_x^2 - k_y^2 | 0 \rangle$ for [001] oriented nanowires and $\beta_1^{\text{ZB}} = \langle 0 | k_x^2 + \frac{1}{2} k_y^2 | 0 \rangle$ for [110] oriented nanowires and $\beta_1^{\text{ZB}} = \frac{1}{2} \langle 0 | k_x^2 - k_y^2 | 0 \rangle$. For wurtzite we have,

$$\begin{aligned} \vec{\Omega}_{[0001]}^{\text{WZ}} &= 0 \\ \vec{\Omega}_{[10\bar{1}0]}^{\text{WZ}} &= k_z [0, -\alpha^{\text{WZ}} - \gamma^{\text{WZ}} (\beta_1^{\text{WZ}} - k_z^2), 0], \end{aligned} \quad (2.139)$$

where $\beta_1^{\text{WZ}} = b \langle 0 | k_x^2 | 0 \rangle + \langle 0 | k_y^2 | 0 \rangle$. Notice that, except for the zinc-blende along [001] direction, all systems have a spin texture along y due to Dresselhaus SOC.

To obtain the SIA projected Hamiltonian, we have to take into consideration the direction of the applied electric field. If E is applied along the x axis it would provide a spin texture in the yz plane. If E is applied along the y axis it would provide a spin texture in the xz plane. But since the x and y directions are confined, the remaining term that can spin split the subbands are given by

$$H_{\text{SIA}} = - \left[\alpha_{\text{ele},R}^n(\vec{r}; V_{\text{ele}}) + \alpha_{\text{bm},R}^n(\vec{r}; V_{\text{bm}}) \right] k_z \sigma_y, \quad (2.140)$$

in the case of E along the x axis providing a spin texture along the y direction, and

$$H_{\text{SIA}} = - \left[\alpha_{\text{ele},R}^n(\vec{r}; V_{\text{ele}}) + \alpha_{\text{bm},R}^n(\vec{r}; V_{\text{bm}}) \right] k_z \sigma_x, \quad (2.141)$$

in the case of E along the y axis providing a spin texture along the x direction.

Here, $\alpha_{\text{ele},R}^n(\vec{r}; V_{\text{ele}}) = \alpha_0(\vec{r})(\partial/\partial x + \partial/\partial y)V_{\text{ele}}(\vec{r})$, is the Rashba parameter for each subband due to the electric field and $\alpha_{\text{bm},R}^n(\vec{r}; V_{\text{bm}}) = \alpha_1(\vec{r})(\partial/\partial x + \partial/\partial y)V_{\text{bm}}(\vec{r})$ is the Rashba parameter for each subband due to the band mismatch, V_{bm} , i. e., is the shape of the confinement potential. The band mismatch contribution to the Rashba model arises from the fact that the wave function is not symmetric anymore and its average position is localized closer to one wall of the nanowire than the other. Therefore, the SIA projection's to the first conduction subband is written as

$$\langle 0, 0, s | H_{\text{SIA}} | 0, 0, s' \rangle = -s k_z \left(\langle \alpha_{\text{ele},R}^0 \rangle + \langle \alpha_{\text{bm},R}^0 \rangle \right), \quad (2.142)$$

where $s = \pm 1$. We further simplify the above equation identifying $\alpha_R = \langle \alpha_{\text{ele},R}^0 \rangle + \langle \alpha_{\text{bm},R}^0 \rangle$.

Considering the combined description of the system, i. e., the presence of both Rashba and Dresselhaus SOC, the total spin-splittings given by $\Delta E = \sqrt{\vec{\Omega}_x^2 + \vec{\Omega}_y^2 + \vec{\Omega}_z^2}$, are calculated on Table 3 up to the third order in k_z .

Table 3: Linear, ΔS_L , and cubic, ΔS_C , spin-splitting coefficients of the total Hamiltonian for the first subband of zinc-blende and wurtzite nanowires. Here we use the Rashba parameter $\alpha_R = \langle \alpha_{\text{ele},R}^0 \rangle + \langle \alpha_{\text{bm},R}^0 \rangle$. Since WZ $[11\bar{2}0]$ and $[10\bar{1}0]$ have the same contribution we just use one label to address it, namely WZ $[11\bar{2}0]$.

	E_x		E_y	
	ΔS_L (meV nm)	ΔS_C (meV nm ³)	ΔS_L (meV nm)	ΔS_C (meV nm ³)
ZB [001]	$\sqrt{(\gamma^{\text{ZB}}\beta_1^{\text{ZB}})^2 + \alpha_R^2}$	0	$\sqrt{(\gamma^{\text{ZB}}\beta_1^{\text{ZB}})^2 + \alpha_R^2}$	0
ZB [110]	$ \alpha_R + \gamma^{\text{ZB}}\beta_1^{\text{ZB}} $	$\frac{\gamma^{\text{ZB}}}{2}\text{sign}[\Delta S_L]$	$\sqrt{\alpha_R^2 + (\gamma^{\text{ZB}}\beta_1^{\text{ZB}})^2}$	$-\frac{(\gamma^{\text{ZB}})^2\beta_1^{\text{ZB}}}{2\sqrt{\alpha_R^2 + (\gamma^{\text{ZB}}\beta_1^{\text{ZB}})^2}}$
ZB [111]	$ \alpha_R + \frac{\gamma^{\text{ZB}}\beta_1^{\text{ZB}}}{\sqrt{6}} $	0	$\sqrt{\alpha_R^2 + \frac{1}{6}(\gamma^{\text{ZB}}\beta_1^{\text{ZB}})^2}$	0
WZ [0001]	$ \alpha_R $	0	$ \alpha_R $	0
WZ $[11\bar{2}0]$	$ \alpha_R + \alpha^{\text{WZ}} + \gamma^{\text{WZ}}\beta_1^{\text{WZ}} $	$-\gamma^{\text{WZ}}\text{sign}[\Delta S_L]$	$\sqrt{\alpha_R^2 + (\alpha^{\text{WZ}} + \gamma^{\text{WZ}}\beta_1^{\text{WZ}})^2}$	$-\gamma^{\text{WZ}}\frac{(\alpha^{\text{WZ}} + \gamma^{\text{WZ}}\beta_1^{\text{WZ}})}{\sqrt{\alpha_R^2 + (\alpha^{\text{WZ}} + \gamma^{\text{WZ}}\beta_1^{\text{WZ}})^2}}$

Source: By the author.

Finally let us discuss the effects of the confinement on the effective mass. Consider the parabolic form of the energy dispersion given by $\vec{k} \frac{1}{m(\vec{r})} \vec{k}$, with $m(\vec{r}) \propto P^{-2} [E'(\vec{r}) - E]$, where P is the dipole matrix element (Kane's parameter), $E'(\vec{r})$ is the energy variation on the region and E the state's energy. Noting that $E'(\vec{r})$ is the largest energy, we can expand

$[E'(\vec{r})]^{-1}$ in terms of $[V_{\text{ele}}(\vec{r}) - E][E'(\vec{r})]^{-1}$. Therefore, up to second order we get⁶⁷

$$\frac{1}{\tilde{m}(\vec{r}; V_{\text{ele}})} \propto P^2 \left[\frac{1}{E'(\vec{r})} + \frac{V_{\text{ele}}(\vec{r}) - E}{[E'(\vec{r})]^2} \right], \quad (2.143)$$

and the Hamiltonian H_0 for the first conduction subband of the nanowires are

$$H_M(\vec{r}; V_{\text{ele}}) = \frac{\hbar^2}{2m_0} (\nabla_{x,y} + k_z) \left[\frac{1}{\tilde{m}(\vec{r}; V_{\text{ele}})} (\nabla_{x,y} + k_z) \right], \quad (2.144)$$

with $\nabla_{x,y} = -i(\partial/\partial x + \partial/\partial y)$.

The projection of Eq. (2.144) into the first subband yields

$$\begin{aligned} \langle 0, 0, s | H_0(\vec{r}; V_{\text{ele}}) | 0, 0, s \rangle &= E(k_z) \\ &= \frac{\hbar^2}{2m_0} \frac{k_z^2}{m^{*,n}}, \end{aligned} \quad (2.145)$$

where m_n^* is the effective mass for the n -th subband already taking into account the quantum confinement.

Therefore, the Hamiltonian that describes the first subband of the nanowires is given by

$$\tilde{H}(k_z) = E(k_z) \sigma_0 + \vec{\Omega}_{ijk}(\vec{k}) \cdot \vec{\sigma} - k_z \alpha_R \sigma_x, \quad (2.146)$$

and the energy dispersion is, up to cubic-in- k terms

$$\varepsilon_{\pm}(k_z) = E(k_z) \pm (\Delta S_L k_z + \Delta S_C k_z^3), \quad (2.147)$$

where ΔS_L and ΔS_C are given in Table 3.

2.7 Superconductor proximity effects

Bardeen, Cooper & Schrieffer⁷⁰ proposed a microscopic theory to explain superconductivity where they consider only the electrons on the Fermi surface and replaced the interaction between electrons and phonons by an attraction between electrons resulting in a coupling only between electrons with opposite momenta. Bogoljubov, Tolmachov & Širkov⁷¹ proposed a more general solution to the problem where they used a canonical

transformation, based on the idea that particles with opposite momenta form bound pairs. Here, we present a general overview of how the BdG formalist is used to study the superconducting proximity effect based on the fact that electrons with opposite momenta are coupled by the pairing potential.¹⁵⁴

2.7.1 Bogoliubov-de-Gennes (BdG) formalism

Before jump into the introduction of the proximity effects into the $\mathbf{k} \cdot \mathbf{p}$ Hamiltonians, it is useful to make a historical overview of how the BdG formalism⁷¹ helped to solve the equations describing the conventional s-wave Bardeen, Cooper & Schrieffer⁷⁰ (BCS) superconductor. We start with a simple metal with spin degeneracy given by the single-particle Hamiltonian

$$H = \left(\frac{p^2}{2m} - \mu \right) I_{2 \times 2}, \quad (2.148)$$

where μ is the chemical potential defining the Fermi surface, m is the mass, $I_{2 \times 2}$ is the identity matrix in spin variables, and, assuming isotropy, $p^2 = \sum_i^{x,y,z} p_i^2$.

It is helpful to write this Hamiltonian in the second-quantization formalism

$$H = \sum_{\vec{p}, \sigma} c_{\vec{p}\sigma}^\dagger \left(\frac{p^2}{2m} - \mu \right) c_{\vec{p}\sigma} \equiv \sum_{\vec{p}, \sigma} c_{\vec{p}\sigma}^\dagger \epsilon(p) c_{\vec{p}\sigma}, \quad (2.149)$$

where $c_{\vec{p}\sigma}^\dagger$ creates a quasiparticle with momentum \vec{p} and spin σ . We can re-write this Hamiltonian as

$$\begin{aligned} H &= \frac{1}{2} \sum_{\vec{p}\sigma} \left[c_{\vec{p}\sigma}^\dagger \epsilon(p) c_{\vec{p}\sigma} - c_{\vec{p}\sigma} \epsilon(p) c_{\vec{p}\sigma}^\dagger \right] + \frac{1}{2} \sum_{\vec{p}} \epsilon(p) \\ &= \frac{1}{2} \sum_{\vec{p}\sigma} \left[c_{\vec{p}\sigma}^\dagger \epsilon(p) c_{\vec{p}\sigma} - c_{-\vec{p}\sigma} \epsilon(-p) c_{-\vec{p}\sigma}^\dagger \right] + \frac{1}{2} \sum_{\vec{p}} \epsilon(p), \end{aligned} \quad (2.150)$$

where in the first equality we have used $\{c_{\vec{p}\sigma}^\dagger, c_{\vec{p}'\sigma'}\} = \delta_{\sigma\sigma'} \delta_{\vec{p}\vec{p}'}$ and in the second equality we relabeled the sum index from \vec{p} to $-\vec{p}$. The Hamiltonian can be written in a more compact fashion in terms of the spinor $\Psi_{\vec{p}} \equiv \left(c_{p\uparrow} c_{p\downarrow} c_{-p\uparrow}^\dagger c_{-p\downarrow}^\dagger \right)^T$,

$$H = \sum_{\vec{p}} \Psi_{\vec{p}}^\dagger H_{BdG}(\vec{p}) \Psi_{\vec{p}} + \text{constant}, \quad (2.151)$$

and its matrix form is

$$H_{BdG}(\vec{p}) = \frac{1}{2} \begin{pmatrix} \epsilon(p) & 0 & 0 & 0 \\ 0 & \epsilon(p) & 0 & 0 \\ 0 & 0 & -\epsilon(-p) & 0 \\ 0 & 0 & 0 & -\epsilon(-p) \end{pmatrix}. \quad (2.152)$$

The previous Hamiltonian is invariant under $H_{BdG}(\vec{p}) = -CH_{BdG}^T(-\vec{p})C^{-1}$, where $C = \tau^x \otimes I_{2 \times 2}$ and $\tau^x = \begin{pmatrix} 0 & 1 \\ 1 & 0 \end{pmatrix}$ acts on the momentum degree of freedom. This invariance is known as the particle-hole or charge-conjugation symmetry.

Up to now the only thing we made was to double the size of our problem, from a 2×2 matrix to a 4×4 . The point here is that in doubling the problem, we write explicitly both the quasi-particles and its time-reversal counterpart, so when we introduce the pairing potential from the superconductor the coupling between them becomes explicitly.

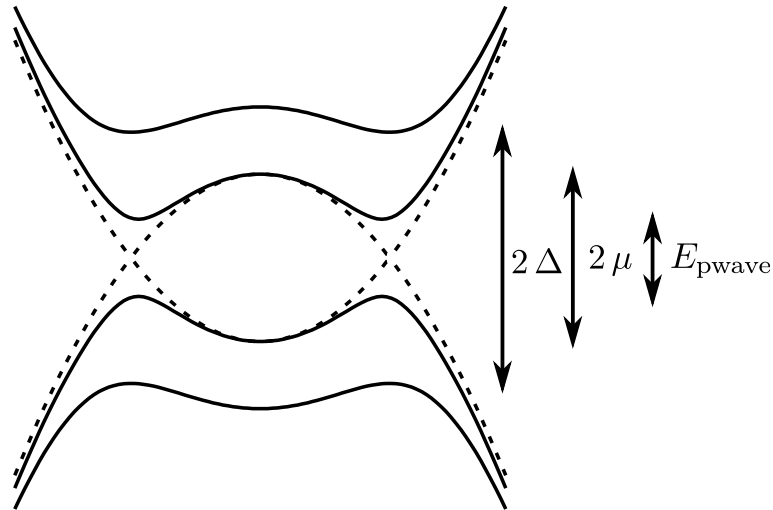


Figure 12: Energy dispersion of the BdG model. The outer solid lines corresponds to the s-wave coupling whereas the inner solid to the p-wave coupling. The inner dashed corresponds to the case where the superconducting proximity effect coupling, Δ , is turned off. The arrow on the right side indicates the main energy separation of the bands. $E_{\text{pwave}} \approx \Delta$

Source: By the author.

2.7.1.1 s-wave superconductors

Basically, s-wave superconductors corresponds to the case where the gap (or pairing) parameter is isotropic and it pairs quasi-particles in the spin-singlet configuration, therefore we can write

$$\begin{aligned} H_{\Delta} &= \Delta c_{\vec{p}\uparrow}^{\dagger} c_{-\vec{p}\downarrow}^{\dagger} + \Delta^* c_{-\vec{p}\downarrow} c_{\vec{p}\uparrow} \\ &= \frac{1}{2} \left[\Delta \left(c_{\vec{p}\uparrow}^{\dagger} c_{-\vec{p}\downarrow}^{\dagger} - c_{-\vec{p}\downarrow}^{\dagger} c_{\vec{p}\uparrow}^{\dagger} \right) + \Delta^* \left(c_{-\vec{p}\downarrow} c_{\vec{p}\uparrow} - c_{\vec{p}\uparrow} c_{-\vec{p}\downarrow} \right) \right], \end{aligned} \quad (2.153)$$

where Δ is a complex number representing the superconducting order parameter. The total Hamiltonian now reads, in the matrix representation

$$H_{BdG}(\vec{p}, \Delta) = \frac{1}{2} \begin{pmatrix} \epsilon(p) & 0 & 0 & \Delta \\ 0 & \epsilon(p) & -\Delta & 0 \\ 0 & -\Delta^* & -\epsilon(-p) & 0 \\ \Delta^* & 0 & 0 & -\epsilon(-p) \end{pmatrix} \quad (2.154)$$

and the energy spectrum is made up of two doubly degenerate bands with energies $E_{\pm} = \pm \sqrt{\epsilon(\vec{p})^2 + |\Delta|^2}$.

In Fig 12 we show, in the outer solid lines, the energy dispersion for the case of s-wave superconducting pairing. The gap between the upper and lower branches is given by 2Δ .

2.7.1.2 p-wave superconductors in one dimension

A p-wave superconductor differs from the s-wave on the fact that it now pairs quasi-particles in the spin-triplet configuration. Without loss of generality, lets write the non-superconducting 1D metal of spinless (or fully spin-polarized fermions)

$$H = \sum_p c_p^{\dagger} \left(\frac{p^2}{2m} - \mu \right) c_p. \quad (2.155)$$

but now we introduce a momentum dependent pairing potential

$$H_{\Delta} = \frac{1}{2} \left(\Delta p c_p^{\dagger} c_{-p}^{\dagger} + \Delta^* p c_{-p} c_p \right). \quad (2.156)$$

giving us the following Hamiltonian in matrix representation

$$H_{BdG} = \sum_p \frac{1}{2} \Psi_p^\dagger \begin{pmatrix} \frac{p^2}{2m} - \mu & \Delta p \\ \Delta^* p & -\frac{p^2}{2m} + \mu \end{pmatrix} \Psi_p, \quad (2.157)$$

where $\Psi_p = (c_p c_{-p}^\dagger)^T$. This Hamiltonian has two energy bands $E_\pm = \pm \sqrt{\epsilon(p)^2 + |\Delta|^2 p^2}$ and it supports a single-particle, zero-energy solution, known as the zero energy Majorana fermion bound state.²⁶ In other words, it is a fermion state, which is its own antiparticle.

In Fig 12 we show, in the inner solid lines, the energy dispersion for the case of p-wave superconducting pairing. The gap between the upper and lower branches is given by $E_{\text{pwave}} \approx \Delta$ whereas the gap at $k = 0$ is 2μ , where μ is the chemical potential.

2.7.2 Proximity effects on $\mathbf{k} \cdot \mathbf{p}$ Hamiltonians

The general BdG equation can be written as,^{32,34,188}

$$H_{\text{BdG}} = \left\{ \left[\left(\frac{\hbar^2}{2m_0} \right) \left(\frac{1}{m^*} \right) k^2 - \mu \right] \sigma_0 + \alpha_R k \sigma_i \right\} \tau_z - \frac{g^* \mu_b}{2} \vec{B} \cdot \vec{\sigma} + \Delta \sigma_0 \tau_x, \quad (2.158)$$

where Δ is the pairing potential, $\vec{\sigma}$ is a vector containing the Pauli matrices (plus the identity, σ_0) acting on the spin degree of freedom and $\vec{\tau}$ is a vector also containing the Pauli matrices but acting on the particle-hole space. The wave function is in the Nambu spinor basis, i. e., it contains both particle and antiparticle wave functions and is written as $\Psi(\vec{r}) = [u_\uparrow(\vec{r}), u_\downarrow(\vec{r}), v_\downarrow(\vec{r}), -v_\uparrow(\vec{r})]^T$. Here the Rashba term can be on x or y direction (depending on the direction of the applied electric field), and the magnetic field has to always be perpendicular to it.

Since our $\mathbf{k} \cdot \mathbf{p}$ Hamiltonians describes the crystals with both bulk inversion asymmetry and structural inversion symmetry, for instance when an external electric field is applied, its subbands are spin-split away from $\vec{k} = 0$. Especially for the conduction subbands, they have a ‘Dirac-like’ shape for very small momenta. Alicea³³ showed that the combination of this ‘Dirac-like’ shape for the conduction subbands, the presence of a magnetic field, giving a Zeeman spin-splitting, and the proximity effects of a s-wave superconductor allows for an effective p-wave pairing in the lowest branch of the conduction subband. However, in this thesis, instead of using the complete multiband

$\mathbf{k} \cdot \mathbf{p}$ Hamiltonians in a realistic configuration of the system (semiconductor- superconductor hybrid setup), we opted to use the effective two-band model, Eq. (2.125), as our $H_0(\vec{k})$ for simplicity.

With our introduction to superconducting pairing in this section, we can understand the appearance of the topological superconducting phase, and therefore, the possibility of a zero-energy Majorana bound state as: i) the spin-orbit coupling spin polarize the subbands which in turn are splitted at $\vec{k} = 0$ by the magnetic field; ii) with the Fermi level set in between the Zeeman gap, we get an effective spinless (or polarized spinful) metal; iii) the superconductor induces a p-wave pairing which is known to suport Majorana fermions.²⁶

3 RESULTS

In this chapter we present the results concerning the simulation of the nanowire systems. In the first moment we discuss the g-factors for the nanowires and, in calculating its anisotropy, see how the quantum confinement and spin-orbit coupling modifies their value. After, we present the main results of the thesis that is the modeling of nanowires through phenomenological models. We present a detailed discussion of the nanowires symmetries in their distinct configurations (crystal phase and orientation), their electronic band structure, the spin split of the lowest conduction subband, their spin-orbit coupling energy and the spin polarization. Finally, with the phenomenological model, we apply the BdG formalist to see if the nanowires can undergo a topological transition and host the zero-energy Majorana fermions.

3.1 System setup

In Fig. 13a) we show the schematics of the nanowire with hexagonal cross-section, the coordinate axis, the diameter L and the direction of the applied electric field. In Figs. 13b) and c) we show the growth planes we use for zinc-blende and wurtzite, respectively. Its worth mention that we discuss nanowires with $L = 30 \dots 100$ nm and applied electric field ranging from $E = -4 \dots 4$ mV/nm.

The $\mathbf{k} \cdot \mathbf{p}$ parameters used for zinc-blende InSb are given in Table 4 and for wurtzite InAs in Table 5. To correct account for the spin-splitting in bulk zinc-blende InSb along [110] direction, we fitted the Δ^- parameter to unpublished internal *ab-initio* calculations. We obtained that $\Delta^- = -0.37$ contrasting to $\Delta^- = 0$ ¹³² and $\Delta^- = -0.26$.¹⁶⁹ The parameters of wurtzite InAs are the same ones proposed by the authors in Ref. 144 obtained by fitting the 8-band $\mathbf{k} \cdot \mathbf{p}$ model presented in previous sections to a *ab-initio*¹⁰⁹ band structure calculation.

The in-plane quantum confinement is modeled with the envelope function approximation.^{125-128,189} Essentially, this treatment applied to the multiband $\mathbf{k} \cdot \mathbf{p}$ Hamiltonians gives rise to the substitution $k_{x(y)} \rightarrow -i \partial / \partial x(y)$ and transform the bulk Hamiltonian into a set of coupled linear differential equations. Because of the complexity of such equations, they have to be solved by appropriate numerical methods. We consider the plane wave

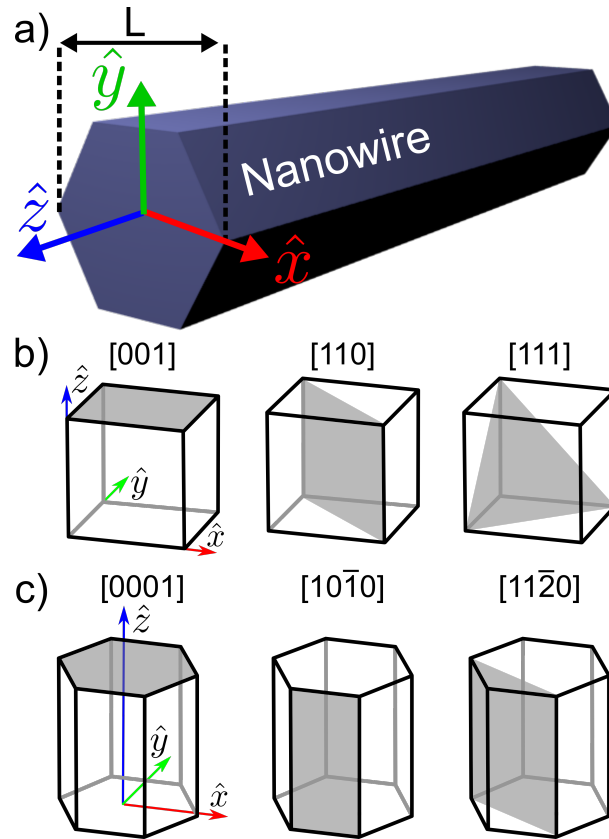


Figure 13: a) Schematics of a hexagonal NW and the coordinate axes we use in the text. The nanowire growth direction is along z , and the electric field is applied along the y -direction. The wire diameter is L , which is the distance between the opposite vertices of the hexagon. In b) and c) we show the growth planes for ZB and WZ crystals, respectively. The shaded regions inside the conventional unit cells indicate the crystal planes perpendicular to the growth directions. The coordinate axes with respect to the crystal orientations are also indicated for $[001]$ ZB and $[0001]$ WZ structures. These are the same axes as used in the confinement geometry a).

Source: By the author.

expansion,^{126,172,177–180} i. e., a Fourier transformation of the space dependent parameters. To simulate the vacuum region, we replaced the bulk parameters by a set of degenerate free electron bands with band mismatch of about 5.5 eV for conduction band and -2.5 eV for valence band, see Fig. 14.¹⁹⁰ The total system (nanowire cross section with surrounding vacuum region) is described by 81×81 points in a 2D regular square mesh, corresponding to 20 plane waves in each direction, which results in a discretization of 41×41 points to the wavefunctions which suffice to achieve energy convergence. We perform the numerical diagonalization using the MAGMA^{191–193} suite that implements the LAPACK routines in a multicore + GPU (graphical processing unit) computational environment.

Table 4: Zinc-blende InSb $\mathbf{k} \cdot \mathbf{p}$ parameters.

Parameter	Zinc-blende InSb 14-band
Lattice parameters (nm)	
a	0.64794
Energy Parameters (eV)	
E_0	0.237
E'_0	3.16
Δ_0	0.81
Δ'_0	0.33
Δ^-	-0.37
Effective mass parameters ($\hbar^2/2m_0$)	
$\tilde{\gamma}_1$	-0.7167
$\tilde{\gamma}_2$	0.2514
$\tilde{\gamma}_3$	-0.3795
F	-1.1335
A	1.0
Interband coupling parameters (eV Å)	
P_0	9.6410
P_1	6.3250
Q	8.1300

Source: Adapted from WINKLER.¹³²

When using Fourier transformation one has to be aware of two phenomena that usually occurs: i) aliasing and ii) Gibbs phenomenon.^{178,194} The former arises when the signal sampling (here signal should be interpreted as any function we are applying the Fourier transformation) is ambiguous for two (or more) distinct frequencies, as seen in Fig. 15a), and the result is that higher frequencies are folded into lower ones. The later arises when the signal has discontinuities. In the discontinuity the reconstructed signal is overshoot (or undershoot).¹⁷⁸ To mitigate both phenomena a windowing can be applied, to the Fourier transformed signal, which dumps the higher frequencies maintaining the original shape intact. The effect of such windowing can be seen in Fig. 15b), where the overshoot (or undershoot) was highly suppressed by the application of the Nuttall windowing.¹⁹⁵

Table 5: WZ InAs $\mathbf{k} \cdot \mathbf{p}$ parameters.

Parameter	WZ InAs 8-band
Lattice parameters (nm)	
a	0.42742
c	0.70250
Energy Parameters (eV)	
E_c	0.6649
E_g	0.4670
Δ_1	0.1003
Δ_2	0.1023
Δ_3	0.1041
Δ_4	0.0388
Effective mass parameters ($\hbar^2/2m_0$)	
A_1	1.5726
A_2	-1.6521
A_3	-2.6301
A_4	0.5126
A_5	0.1172
A_6	1.3103
e_1	-3.2005
e_2	0.6363
Interband coupling parameters (eV Å)	
P_1	8.3860
P_2	6.8987
A_7	-0.4907
α_1	-0.0189
α_2	-0.2892
α_3	-0.5117
β_1	-0.0695
β_2	-0.2171
γ_1	0.5306
Interband second order coupling parameters ($\hbar^2/2m_0$)	
B_1	-2.3925
B_2	2.3155
B_3	-1.7231

Source: Adapted from [FARIA JUNIOR et al.](#)¹⁴⁴

3.2 g-factor

By expanding Eq. (2.49) in terms of the wave functions we get the following expression for the g-factor

$$g_z = g_0 I_2 - 2 \frac{i}{m} \sum_{n,s} \frac{\langle \Psi_{c,s} | \hat{p}_x | \Psi_{n,s} \rangle \langle \Psi_{n,s} | \hat{p}_y | \Psi_{c,s} \rangle}{E_c - E_n} - \frac{\langle \Psi_{c,s} | \hat{p}_y | \Psi_{n,s} \rangle \langle \Psi_{n,s} | \hat{p}_x | \Psi_{c,s} \rangle}{E_c - E_n}, \quad (3.1)$$

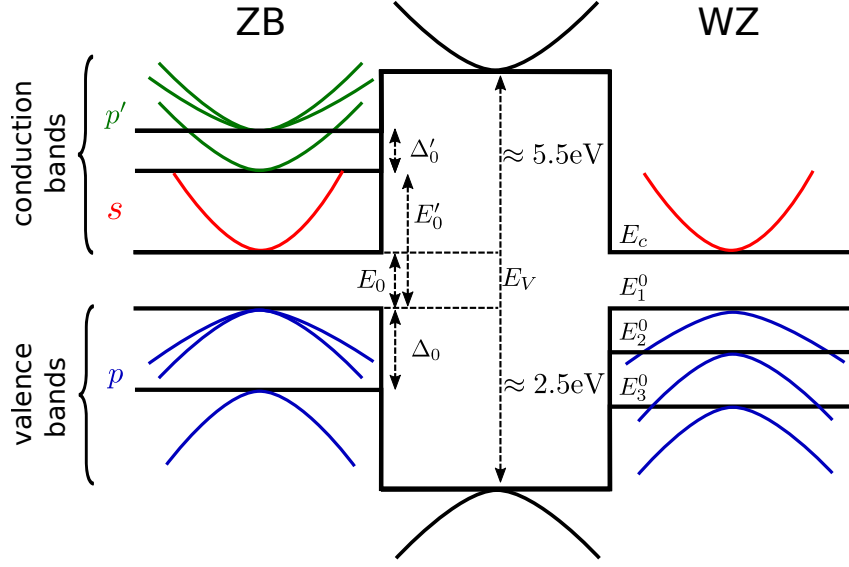


Figure 14: Schematics of the band mismatch. On the left, for the ZB 14-band model both the lowest s and the highest p conduction bands have the same mismatch to the vacuum region. On the right, for WZ 8-band model, the distinction is that, besides the lack of the highest p conduction bands, the p valence bands have an extra splitting (due to the crystal field) at Γ -point, making the p valence bands only spin degenerate. In the figure, the energy labels are, in the Ref. [145](#) notation: $E_c = E_g + \Delta_1 + \Delta_2$, $E_1^0 = \Delta_1 + \Delta_2$, $E_2^0 = \frac{\Delta_1 - \Delta_2}{2} + \sqrt{\left(\frac{\Delta_1 - \Delta_2}{2}\right)^2 + 2\Delta_3^2}$ and $E_3^0 = \frac{\Delta_1 - \Delta_2}{2} - \sqrt{\left(\frac{\Delta_1 - \Delta_2}{2}\right)^2 + 2\Delta_3^2}$, where E_g is the gap energy, Δ_1 is the crystal field splitting (due to the distinction between z and xy) and Δ_2 and Δ_3 are the spin-orbit coupling energies.

Source: By the author.

where I_2 is the identity matrix 2×2 , s is the spin component, $\Psi_{c,s}$ are the calculated wave functions for the lowest conduction subband, $\Psi_{n,s}$ the wave functions of all other states, E_c the energies of the states $\Psi_{c,s}$ and E_n the energies of the states $\Psi_{n,s}$. The components g_x and g_y are computed by cyclic permutation of the x, y, z indexes.

To find the proper value of the g -factor we have to obtain all the wave functions of the desired system, at $k = 0$. Then, by performing the calculation of Eq. (3.1) we get a 2×2 matrix that has to be diagonalized to obtain the final value of the g -factor. With the advance of heterogeneous computation and since the $\mathbf{k} \cdot \mathbf{p}$ method is not computationally demanding, the actual diagonalization of the entire Hamiltonian is performed quite fast. The most time consuming task is to perform all the vector-matrix-vector computation in

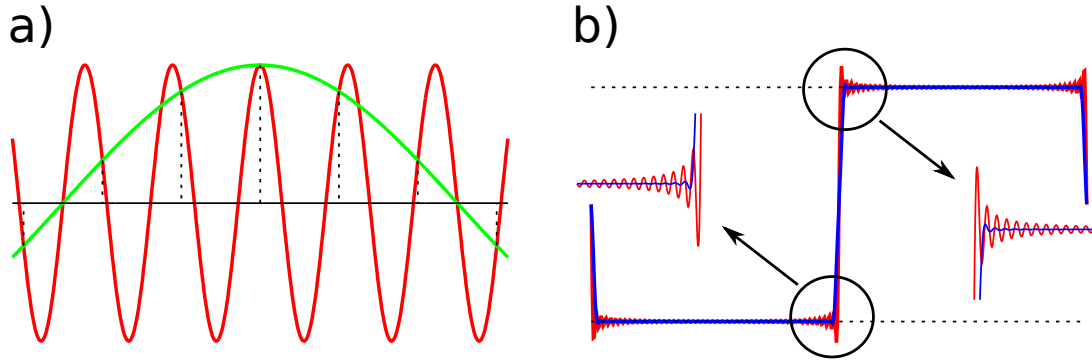


Figure 15: Aliasing and Gibbs phenomena. a) Sampling leads to ambiguous frequencies given the same value at sampling point. b) Overshoot (or undershoot) of the values of reconstructed signal at a discontinuity suppressed by application of the Nuttall window.¹⁹⁵

Source: By the author.

Eq. (3.1). The main advantage of this method is that we can compute the g -factors in all directions accounting for the microscopic description of the system, via the $\mathbf{k} \cdot \mathbf{p}$ method, including both spin-orbit coupling mechanisms.

Using Eq. (3.1) we have calculated the g -factor tensor for the conduction band of both bulk zinc-blende InSb and wurtzite InAs. Moreover, this methodology can be applied to any energy band at any k point. Since zinc-blende has cubic symmetry and it is isotropic in all directions, its g -factor is $g_{\text{InSb}}^{\text{ZB}} = -51.331$ which has been known since the 1970.⁷⁵ On the other hand, wurtzite with its hexagonal symmetry gives us distinct g -factors for the x, y -plane and the z direction as seen on Table 6. Furthermore, for the directions $[11\bar{2}0]$ and $[10\bar{1}0]$, we have that the x axis is distinct from the y, z -plane, as shown in Figs. 8 and 9. For comparison, the g -factor for zinc-blende InAs is $g_{\text{InAs}}^{\text{ZB}} = -14.8$.⁷⁵

Table 6: Bulk g -factor for wurtzite InAs.

	g_x	g_y	g_z
$[0001]$	-6.708	-6.708	-6.095
$[11\bar{2}0]$	-5.983	-7.306	-7.306
$[10\bar{1}0]$	-5.983	-7.306	-7.306

Source: By the author.

The strong deviation of the g -factor from the free-electron value is understood in

light of the Roth's formula.⁷⁴ The *g*-factor depends on the gap energy as well as the spin-orbit coupling. For instance, InSb has $\frac{E_g}{\Delta_{\text{SO}}} < 1$, whereas for InAs $\frac{E_g}{\Delta_{\text{SO}}} > 1$. In the presence of quantum confinement the *g*-factor is known to drastically change values.^{4,76,77,80,86–88,132} This dependence on the quantum confinement is due to the orbital momentum contribution represented by the matrix element $\langle \Psi_{c,s} | \hat{p} | \Psi_{n,s} \rangle$. It was predicted that in highly confined nanostructures, like quantum dots, the orbital contribution is quenched ($\langle \Psi_{c,s} | \hat{p} | \Psi_{n,s} \rangle \rightarrow 0$) and the *g*-factor asymptotically goes to the free electron value ($g_0 = 2.0023$).^{77,87} Furthermore, a universal behavior^{80,87} for the *g*-factor in certain types of nanostructures was discovered and it goes as $\propto 1/E_g^2$. Like in quantum dots, the quantum confinement in thin nanowires decreases the *g*-factor value and as we increase the nanowire diameter, its *g*-factor goes asymptotically to the bulk value.

The anisotropy of the *g*-factor, in quantum wells, is explained by the quantum confinement and SIA spin-orbit coupling mechanism.^{4,85} In asymmetric quantum wells the cyclotron orbit of the electron in-plane differs from the one along the growth direction. Fixing our referential as the center of the electron's orbit, one can imagine that, along the growth direction, the electron feels the asymmetry of the quantum well, i. e., it feels one side of the barrier more than the other; whereas the in-plane orbit is confined inside the well material and does not feel any discontinuity. In this picture, the *g*-factor in-plane is isotropic ($g_x = g_y$) because the BIA spin-orbit coupling is not taken into account. Therefore, using our realistic $\mathbf{k} \cdot \mathbf{p}$ method that has both BIA and SIA spin-orbit coupling mechanisms taking into account, we calculated the *g*-factor anisotropies of the in-plane components as well as the out-of-plane ones.

In Fig. 16 we show the calculated *g*-factors tensor for both zinc-blende InSb and wurtzite InAs nanowires without an applied electric field. Due to quantum confinement the *g*-factors of the nanowires differ from those of the bulk system. In Figs. 16a) and 16b) we show the in-plane *g*-factor values for zinc-blende InSb nanowires. One can see that the general trend is that thin nanowires have a smaller (in modules) *g*-factor and as we increase the diameter the *g*-factor tends to the bulk value $g_{\text{InSb}}^{\text{ZB}} = -51.331$. Actually, for thin nanowires we get g_x^* and $g_y^* \approx -25$ about half of the bulk value and it asymptotically grows (in absolute value) as the nanowire diameter increases. The same trend can be observed in the free direction, see Fig. 16c).

In Figs. 16d) and 16e) we show the in-plane *g*-factors for wurtzite InAs nanowires.

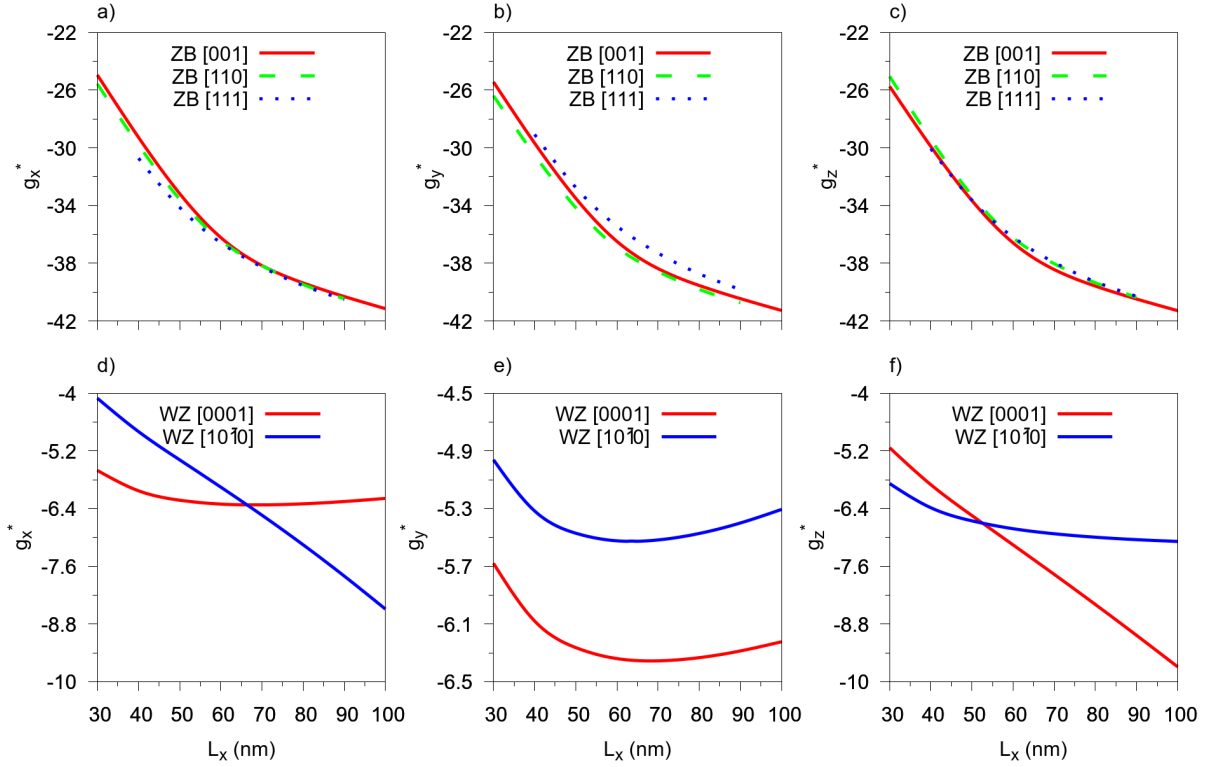


Figure 16: a), b) and c) show the g_x^* , g_y^* and g_z^* for zinc-blende InSb nanowires, respectively. d), e) and f) show the g_x^* , g_y^* and g_z^* for wurtzite InAs nanowires, respectively. The g-factors were determined without an applied electric field. In the wurtzite case, for notation simplicity, we labeled both orientations ($[10\bar{1}0]$ and $[11\bar{2}0]$) as $[10\bar{1}0]$.

Source: By the author.

Here there is a clear distinction between the nanowires orientation: for the $[0001]$ orientation the in-plane g-factor are almost constant, but with a minimum around $L = 60$ nm with g_x^* and $g_y^* \approx -6.40$ which is very close to the bulk value (see Table 6); whereas for $[10\bar{1}0]$ (or $[11\bar{2}0]$) they are distinct, with g_x^* growing (in absolute value) as the nanowire diameter increases and g_y^* having a minimum around $L \approx 60$ nm. This difference in the in-plane g-factor are also seen in their bulk. In the free direction, see Fig. 16f), the nanowires oriented along $[0001]$ direction are the ones with g_z^* growing in absolute value (like the g_x^* of $[10\bar{1}0]$) whereas the trend for the $[10\bar{1}0]$ oriented nanowires are of asymptotically saturates at around $g_z^* \approx -7$, which is close to the bulk value.

The degree of anisotropy of the g-factor can be defined by the following expression

$$\Delta g_{ij} = \frac{g_i^* - g_j^*}{g_i^* + g_j^*} \quad (3.2)$$

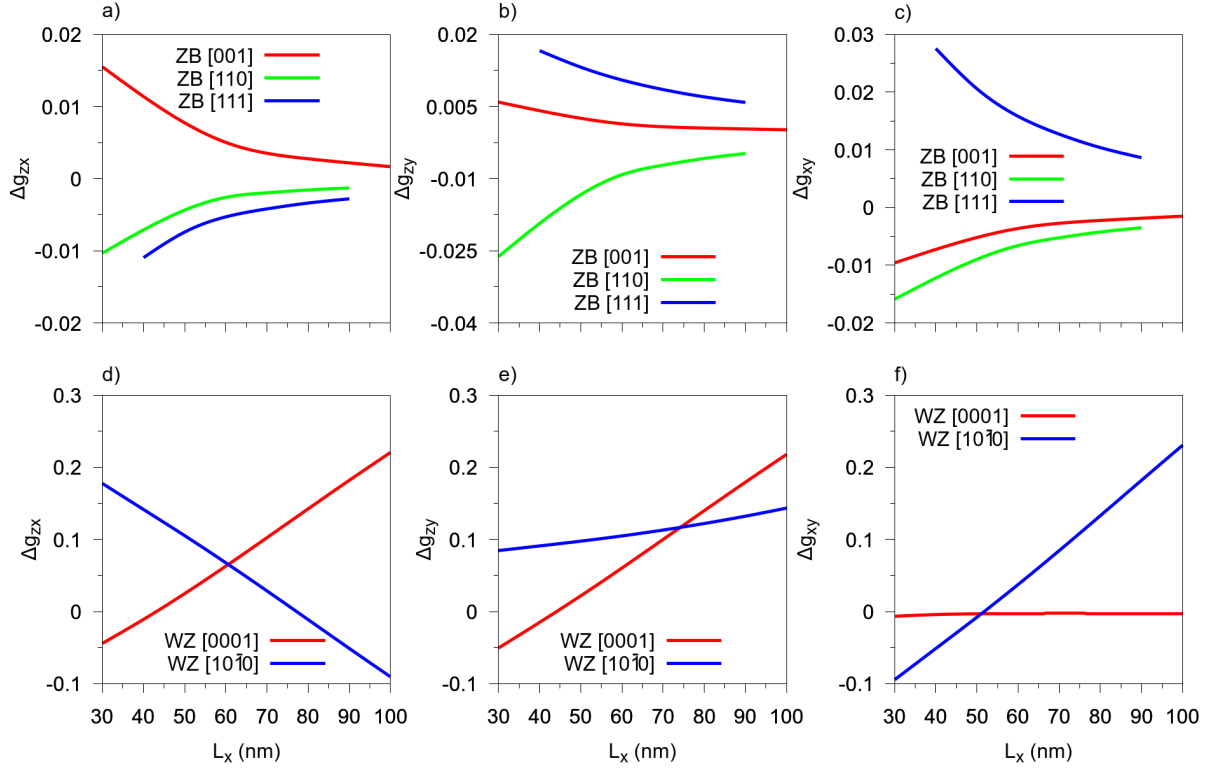


Figure 17: g -factor anisotropy, as defined in Eq. (3.2). a), b) and c) show the Δg_{zx}^* , Δg_{zy}^* and Δg_{xy}^* for zinc-blende InSb nanowires, respectively. d), e) and f) show the Δg_{zx}^* , Δg_{zy}^* and Δg_{xy}^* for wurtzite InAs nanowires, respectively. The g -factors anisotropy were determined without an applied electric field. In the wurtzite case, for notation simplicity, we labeled both orientations ($[10\bar{1}0]$ and $[11\bar{2}0]$) as $[10\bar{1}0]$.

Source: By the author.

where $i, j \in x, y, z$. In Fig. 17 we show the evaluation of the above expression for both zinc-blende InSb and wurtzite InAs nanowires.

In Fig. 17a)-c) we show the zx and zy and xy degree of anisotropy for InSb nanowires and we see that it ranges from -2% to 3% due to quantum confinement effects. Comparing the nanowires orientation we see that the zx and zy anisotropy of $[001]$ and $[110]$ oriented nanowires follows the same trend, whereas for $[111]$ the anisotropy changes from negative to positive sign. For all directions, the general trend is that as we increase the nanowires diameter the anisotropy vanishes, since we are reaching the bulk limit. To clearly see the distinctions between the in-plane g -factors, in Fig. 17c), we show the xy degree of anisotropy and we found that: for $[001]$ oriented nanowires there is about 1% of

anisotropy for thin wires; ii) for $[110]$ follows similar trends as $[001]$; and for $[111]$ oriented nanowires the anisotropy is of about 3% for thin wires, the largest anisotropy.

In Fig. 17d) and 17e) we show the zx and zy degree of anisotropy for InAs nanowires and we see that $[0001]$ they started at about -0.5% for thin nanowires reaching about 2% for thick nanowires. This is due to the behavior of the g_z^* , as seen in Fig. 16f), that always increase as we increase the nanowire diameter. For the $[10\bar{1}0]$ and $[11\bar{2}0]$ oriented nanowires the zx degree of anisotropy has the opposite behavior to the $[0001]$ case, starting at about 2% and decreasing to -1% as we increase the nanowire diameter, whereas the zy always increase for both growth directions. The in-plane anisotropy, in Fig. 17f), is absent for $[0001]$ oriented nanowires whereas it goes from -1% to about 3% in $[10\bar{1}0]$ or $[11\bar{2}0]$ oriented nanowires. These distinctions are already seen in the bulk case for wurtzite InAs and it is enhanced by the quantum confinement effects.

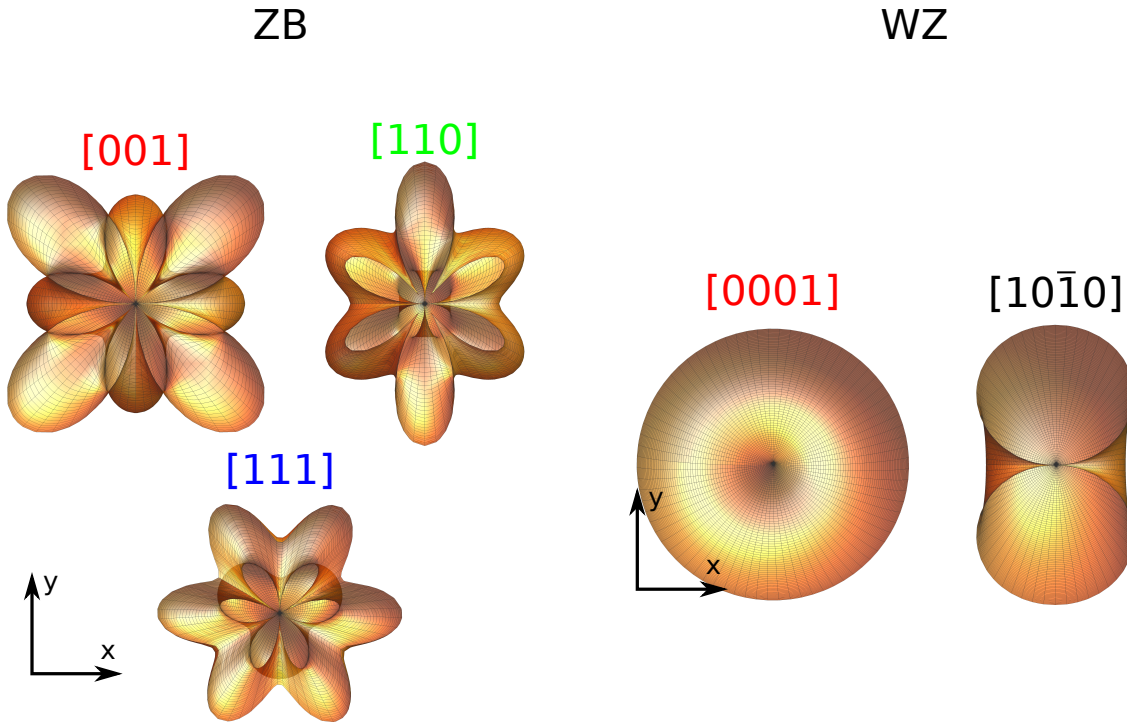


Figure 18: Crosssectional cut of the spin-orbit coupling along the growth directions for ZB and WZ.

Source: By the author.

To explain the anisotropy of the g-factor it is useful to recur to the projection of the spin-orbit coupling field along the desired direction, as shown in Fig. 18. For instance,

for ZB along [001] direction the spin-orbit coupling field has the same magnitude along the x and y direction but along the diagonals it has a larger magnitude. The quantum confinement makes these diagonal projections fold into the x and y direction, and, since the nanowires have a hexagonal cross-section, inevitably the projections are going to be different resulting in the anisotropy of the g-factor that we see. The same analysis can be carried out for the [110] oriented nanowire, but in this case the y component of the spin-orbit coupling field is already larger in the bulk resulting in a larger anisotropy, in comparison with the [001] direction. For [111] oriented nanowires, the x component is the one that is larger, resulting in a positive anisotropy as computed by Eq. (3.2).

For WZ, the [0001] projection of the spin-orbit field has cylindrical symmetry, therefore the tiny anisotropy that we see for thin wires comes only from the quantum confinement. For $[10\bar{1}0]$ or $[11\bar{2}0]$ projection, the y direction is much larger than the x resulting in the anisotropy that we see in Fig. 17f).

3.3 Spin-orbit coupling

For a crystal without inversion symmetry, being either bulk (BIA) or structural (SIA), Kramer's theorem says that the energy bands are, in general, spin split away from Γ -point due to spin orbit coupling. In Fig. 1 we show the effect of such energy split for a given electron band. In Fig. 1a), we show the general case for crystals with inversion symmetry, therefore the bands are always degenerate for a generic wave vector \vec{k} . On the other hand, in Fig. 1b), we show the effect of breaking this inversion symmetry in the presence of spin-orbit coupling. We see that for a generic wave vector, \vec{k} , the bands are spin split and we can associate a spin-orbit coupling energy, E_{SO} , being the difference in energy between the minimum of the lowest band and the energy at $\vec{k} = 0$, hence

$$E_{\text{SO}} = \left(\frac{\hbar^2}{2m_0} \right)^{-1} \Delta S_L^2 m^*. \quad (3.3)$$

In the following subsections we have analyzed the spin splitting for the first conduction subbands as well as the spin-orbit coupling energy, based on symmetry considerations. Before we turn our attention to the results itself, in Fig. 19 we show an example of how we obtain the desired parameters. Given a target subband we perform a quadratic fit on the sum of the two branches to obtain the effective mass parameters, Fig. 19a), and also a quadratic fit on the spin-orbit splitting divided by the momentum extrapolating the value

where the curve intersects the y axis to obtain the linear spin-orbit coupling parameters. The slope of the curve gives us the cubic one, Fig. 19b). With this methodology we are able to reproduce with fidelity the multiband calculated energy dispersion as well as to extract the pertinent parameters which characterizes the system.

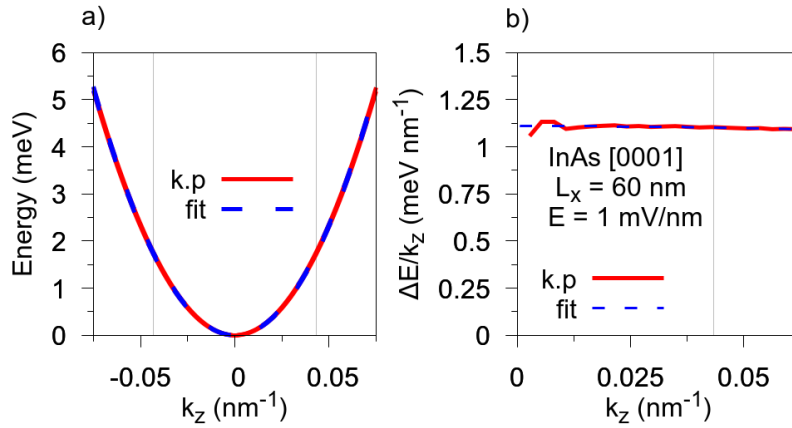


Figure 19: a) Quadratic fit to the $\mathbf{k} \cdot \mathbf{p}$ calculated lowest conduction band structure around Γ of InAs wurtzite nanowire oriented along [0001]. The wire diameter is 60 nm, and the applied electric field 1 mV/nm. b) Spin-orbit splitting of the band in a) divided by momentum. This line is fitted to obtain the linear and cubic spin-orbit coefficients.

Source: By the author.

The shape of the nanowire quantum confinement defines the energy level of each crystalline phase. The electric field, besides breaking the structural symmetry of our system, acts as an extra quantum confinement. The effect of this extra quantum confinement is to modify the energy levels of the nanowire subbands as seen in Figs. 21, 26, 31, 39 and 45. Besides changing the energy levels, it spin splits the bands according to the specific spin-orbit coupling of each crystal phase as we will discuss in the following subsections.

3.3.1 Zinc-blend InSb nanowires

Now let us discuss the effects of the quantum confinement and of the spin-orbit coupling in zinc-blende systems. We begin with zinc-blende nanowires oriented along [001], [110] and [111] direction showing the calculated subband dispersion, i. e. energy as a function of free momentum k_z . We discuss the effects of the quantum confinement taking into account the crystal symmetry in the specific orientation and then we show the

spin splitting and the spin-orbit energy changes as we modify both, the applied electric field and the nanowire diameter.

3.3.1.1 [001] oriented nanowires

We begin by showing the atomic arrangement of a zinc-blende nanowire oriented along [001] direction in Fig. 20a), and its symmetry planes in Fig. 20b). The atoms in this direction do not have the full square, C_{4v} , symmetry because they are stacked in distinct layers, therefore the xz and yz symmetry planes are broken and only the diagonal ones survives. Since the confinement have itself a hexagonal, C_{6v} , symmetry we end-up with no common symmetry plane. This mismatch allows for a confinement induced bulk inversion asymmetry which spin splits the nanowire subbands for small diameters and generates a spin orientation along the z axis.

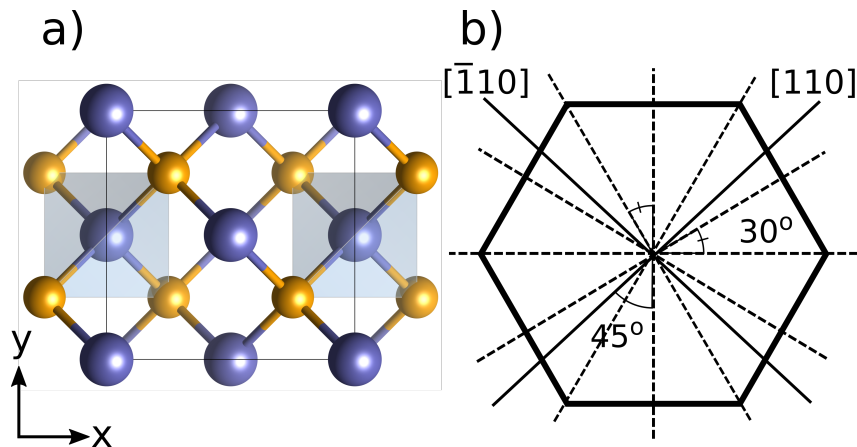


Figure 20: a) Atomic arrangement along [001] orientation of a zinc-blende structure with indicated x and y axis. b) Mirror symmetry planes of the atomic structure (solid) and of the hexagonal confinement (dashed).

Source: By the author.

In Fig. 21a) we show the subband dispersion of a zinc-blende InSb nanowire oriented along [001] direction with $L = 60$ nm for the case with applied electric field, $|E_x| = 4$ mv/nm, along the x axis and on Fig. 21b) for a field, $|E_y| = 4$ mv/nm, along the y axis. For the case without electric field, the subbands are degenerate in spin but when the electric field is present the electronic subbands are spin split due to the SIA spin-orbit coupling.

In Fig. 22 we show a zoom of the first subband of Fig. 21 to explicitly see the spin

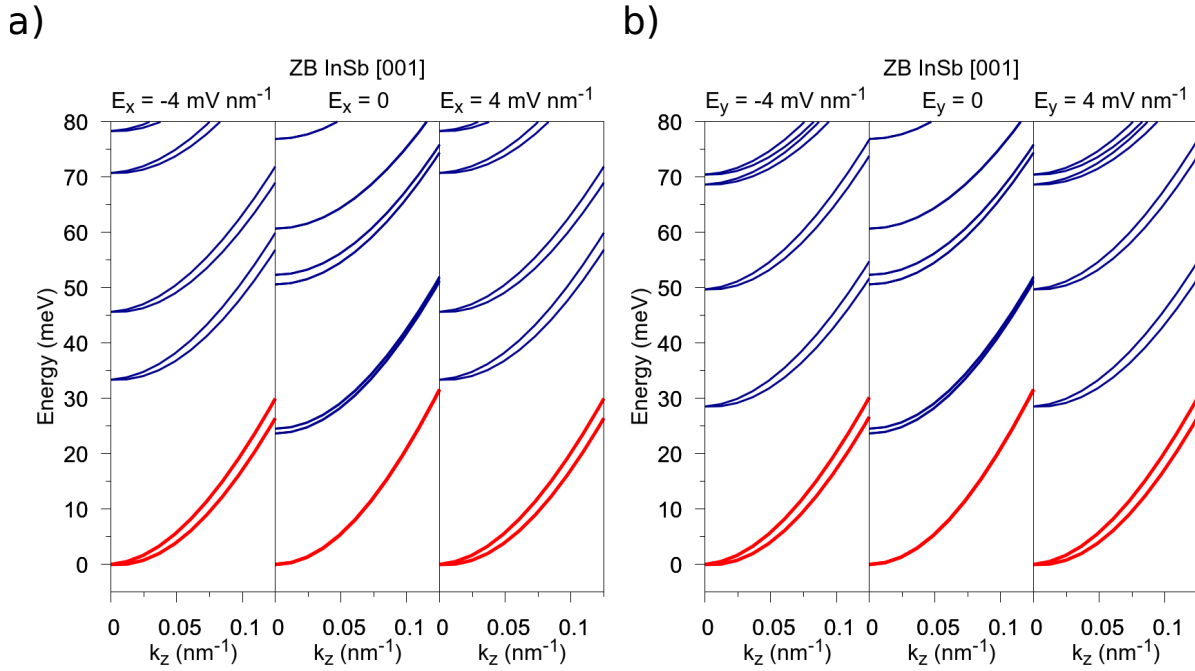


Figure 21: Calculated electronic subband dispersion for a zinc-blende InSb hexagonal nanowire of 60 nm diameter oriented along [001] direction. a) With applied electric field along x axis and b) along y axis. In each subfigure the left most spectrum corresponds to an electric field of $E = -4$ mV/nm, the central panel to zero applied electric field and the right most spectrum is for an electric field $E = 4$ mV/nm.

Source: By the author.

split. In Fig. 22a) we show the case without electric field and we can see that indeed there is no split of the bands for this nanowire diameter. In Figs. 22a) and 22b) we show the zoom of the first subband for the case of an electric field applied along the x and y axis, respectively. In the insets we see the spin splitting of the subband, which is linear with respect to the momentum. This linear behavior is characteristic of a SIA related spin-orbit coupling.

Given the first conduction subband, as in Fig. 22, we apply the numerical fitting method to obtain the effective masses, linear in momentum and cubic in momentum spin splitting parameters. In Fig. 23 we show the spin splitting parameters for three specific nanowire diameters, $L = 30$ nm, $L = 60$ nm and $L = 100$ nm, varying the applied electric field $E = -4, \dots, 4$ mV/nm along the x axis in panels a) and b), and along the y axis in panels c) and d). For this nanowire orientation we see that the spin splitting parameters are symmetric with respect to both orientations of the applied electric field. For small

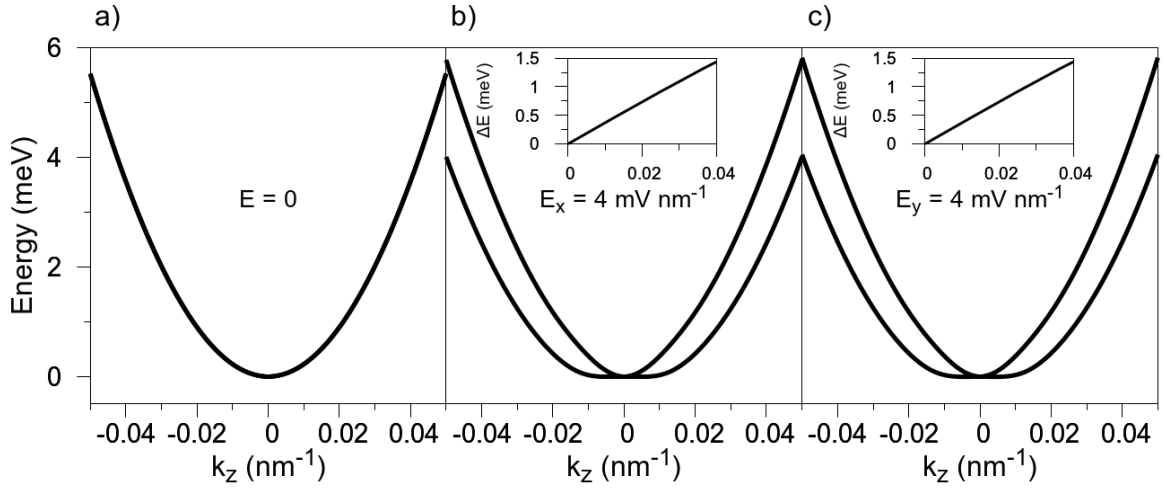


Figure 22: Zoom of the calculated first conduction subband of [001] oriented InSb zinc-blende nanowire at: a) zero; b) finite electric field, $E_x = 4$ mV/nm, along the x axis; and c) finite electric field, $E_y = 4$ mV/nm, along the y axis. In b) and c) we show, in the insets, the SIA induced spin-orbit splitting of the first conduction subband.

Source: By the author.

diameters both linear and cubic spin splitting parameters have a linear dependence with the electric field and as the diameter increase this dependence deviates from the linearity for large enough fields.

In Fig. 24 we show the density maps of the spin-orbit energy (see Eq. (3.3)) calculated for the first conduction subband using the fitted parameters shown in Fig. 23. In a) we show the case of applied electric field along the x axis and in b) along the y axis. Since the linear parameter, ΔS_L , shown in Fig. 23, is symmetric with respect to the applied electric field so is the spin-orbit coupling energy. For [001] oriented zinc-blende nanowires the general trend is that large values of E_{SO} come from large values of applied electric field.

3.3.1.2 [110] oriented nanowires

We begin by showing the atomic arrangement, in Fig. 25a), of a zinc-blende nanowire oriented along [110] direction, and in Fig. 25b) its symmetry planes. The atoms in this direction have a C_2 symmetry, i. e. they are invariant by an inversion $y \rightarrow -y$. Since the confinement has itself a hexagonal, C_{6v} , symmetry we end-up with only the xz symmetry plane in common. This mismatch allows for a confinement induced bulk inversion

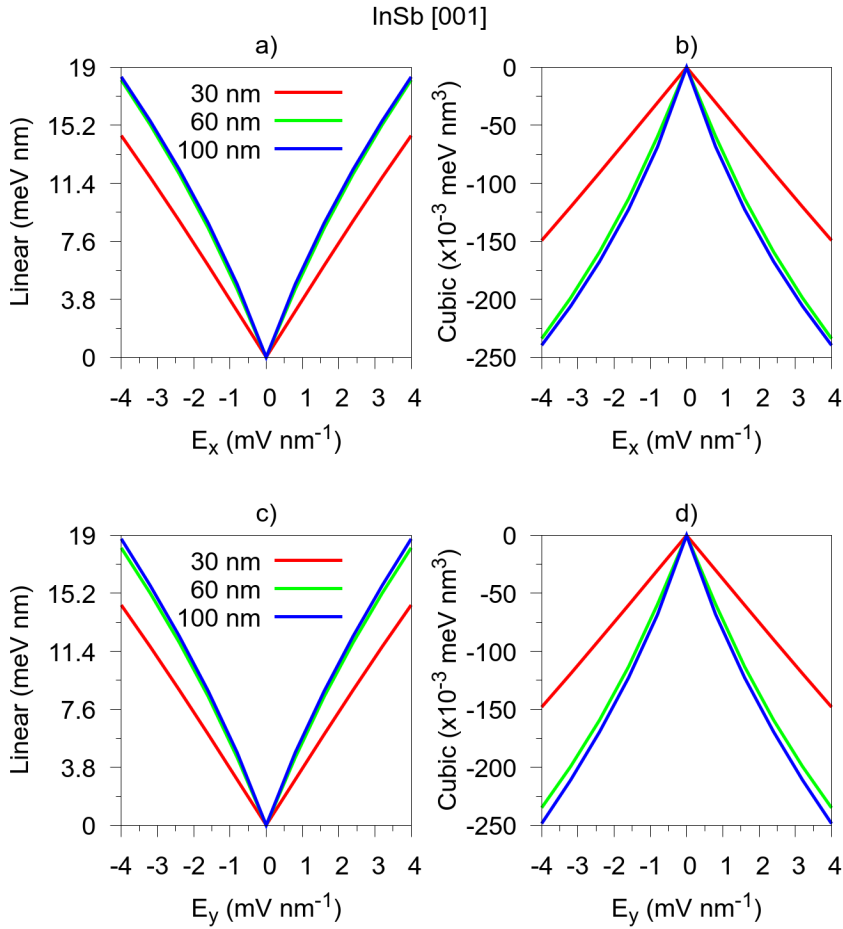


Figure 23: a) and c), linear spin-orbit splitting coefficients, ΔS_L ; b) and d) cubic spin-orbit splitting coefficients, ΔS_C , for different diameters L , for InSb zincblende nanowires oriented along [001]. In a) and b), the applied electric field goes along the x axis and in c) and d) along the y axis.

Source: By the author.

asymmetry which spin splits the nanowire subbands and generates a spin orientation along the y axis.

In Fig. 26a) we show the subband dispersion of a zinc-blende InSb nanowire oriented along [110] direction with $L = 60$ nm for the case with applied electric field, $|E_x| = 4$ mv/nm, along the x axis and, on Fig. 26b) for a field, $|E_y| = 4$ mv/nm, along the y axis. For the case without electric field, the subbands are have a small, but not zero, spin splitting due to BIA spin-orbit coupling and when the electric field is present the electronic subbands becomes more spin split due to the SIA spin-orbit coupling.

In Fig. 27 we show a zoom of the first subband of Fig. 26 to explicitly see the spin

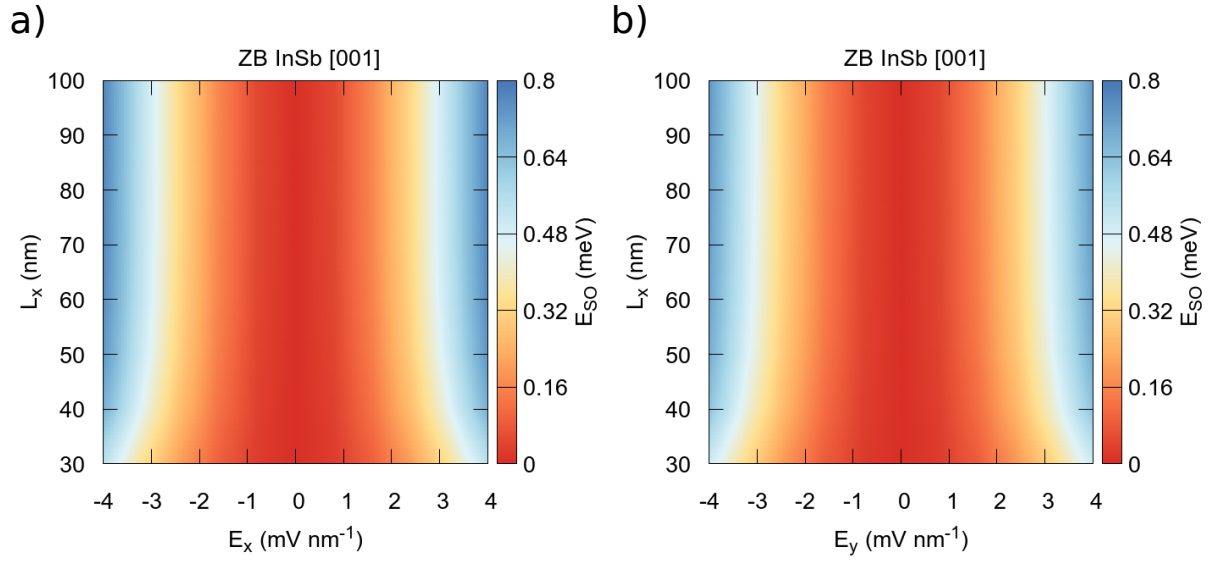


Figure 24: Calculated spin-orbit energy, for different diameters L_x and different transverse electric fields E , for InSb zincblende nanowires oriented along $[001]$. a) applied electric field along x axis and b) along y axis.

Source: By the author.

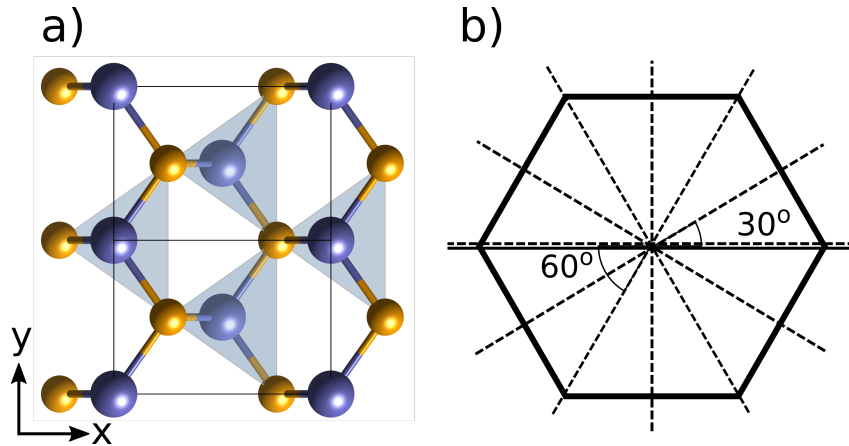


Figure 25: a) Atomic arrangement along $[110]$ orientation of a zinc-blende structure with indicated x and y axis. b) Mirror symmetry planes of the atomic structure (solid) and of the hexagonal confinement (dashed).

Source: By the author.

split. In a) we show the case with an negative electric field along the x axis, in b) the case without electric field and in c) and d) the case with an positive applied electric field along the x and y axis, respectively. Here, contrary to the $[001]$ case, we see in the inset of panel b) that the subband is spin split due to confinement induced by the BIA spin-orbit

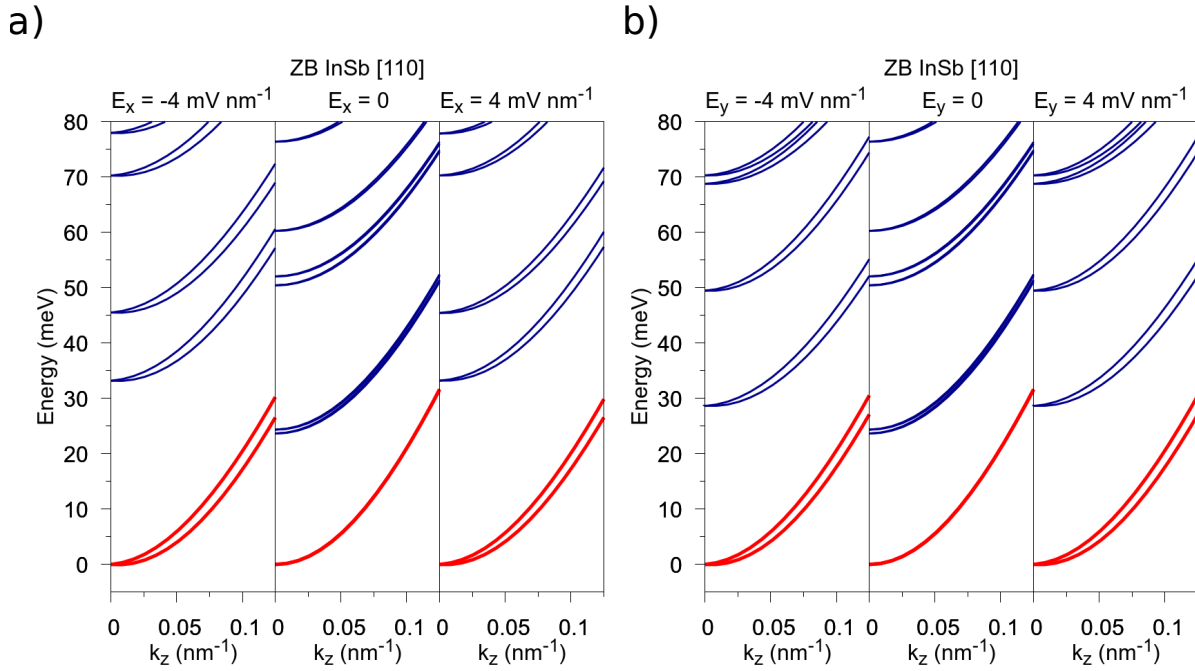


Figure 26: Calculated electronic subband dispersion for a zinc-blende InSb hexagonal nanowire of 60 nm diameter oriented along [110] direction. a) With applied electric field along x axis and b) along y axis. In each subfigure the left most spectrum corresponds to an electric field of $E = -4$ mV/nm, the central panel to zero applied electric field and the right most spectrum is for an electric field $E = 4$ mV/nm.

Source: By the author.

coupling. In the insets of panels a), b) and d) we see the linear behavior of the spin split due to the SIA spin-orbit coupling.

Given the first conduction subband, as in Fig. 27, we apply the numerical fitting method to obtain the effective masses, linear in momentum and cubic in momentum spin splitting parameters. In Fig. 28 we show the spin splitting parameters for three specific nanowire diameters, $L = 30$ nm, $L = 60$ nm and $L = 100$ nm, varying the applied electric field $E = -4, \dots, 4$ mV/nm along the x axis in panels a) and b), and along the y axis in panels c) and d). For this nanowire orientation we see that the spin splitting parameters, for electric field along x axis are not symmetric but for electric field along y axis they are. This asymmetry arises from the interplay between the BIA and SIA spin-orbit couplings. The BIA spin-orbit coupling is maximum for [110] oriented zinc-blende nanostructures, therefore the competition between BIA and SIA shifts the degeneracy case away from zero electric field.

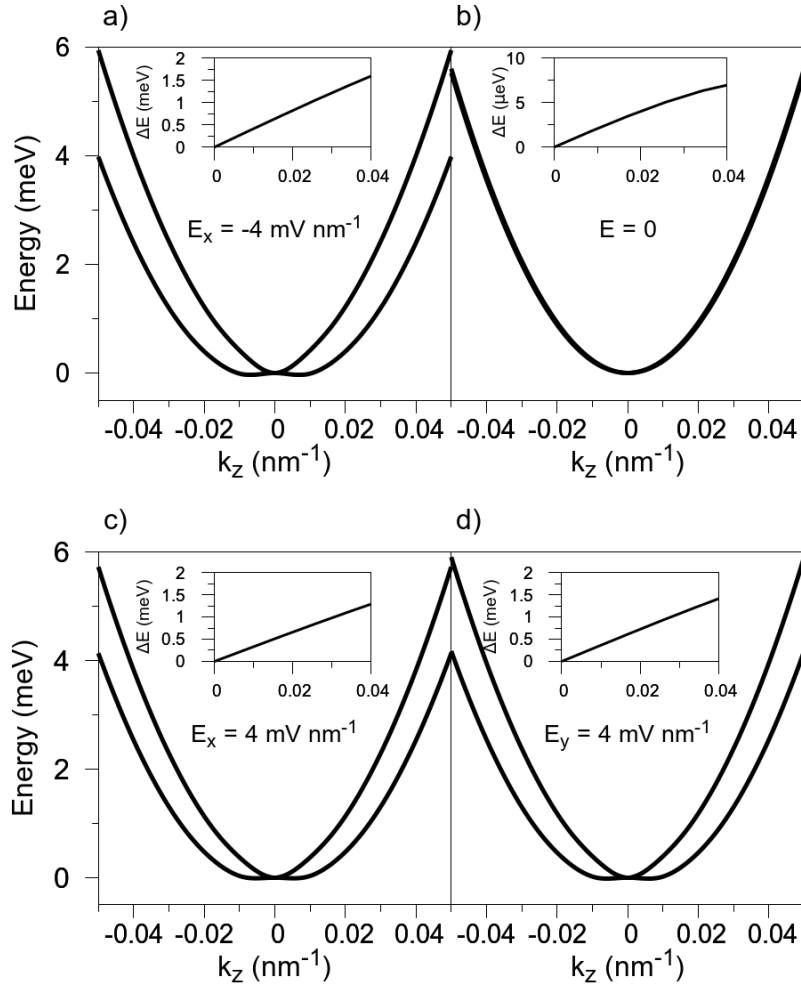


Figure 27: Zoom of the calculated first conduction subband of [110] oriented InSb zinc-blende nanowire at: a) finite electric field, $E_x = -4 \text{ mV/nm}$, along the x axis; b) zero field; c) finite electric field, $E_x = 4 \text{ mV/nm}$, along the x axis; and d) finite electric field, $E_y = 4 \text{ mV/nm}$, along the y axis. In b), in the inset, we show the confinement BIA induced spin-orbit splitting and in a), c) and d), the SIA induced spin-orbit splitting of the first conduction subband.

Source: By the author.

In Fig. 29 we show the density maps of the spin-orbit energy (see Eq. (3.3)) calculated for the first conduction subband using the fitted parameters shown in Fig. 28. In a) we show the case of applied electric field along the x axis and in b) along the y axis. Since the linear parameter, ΔS_L , shown in Fig. 28, presents an asymmetry with respect to the applied electric field along the x axis, we see that E_{SO} also presents such asymmetry. This is not the case for the electric field along y axis. For [110] oriented zinc-blende nanowires the general trend is that large values of E_{SO} come from large values of applied electric field, but for E along the x axis is better to use a negative electric field

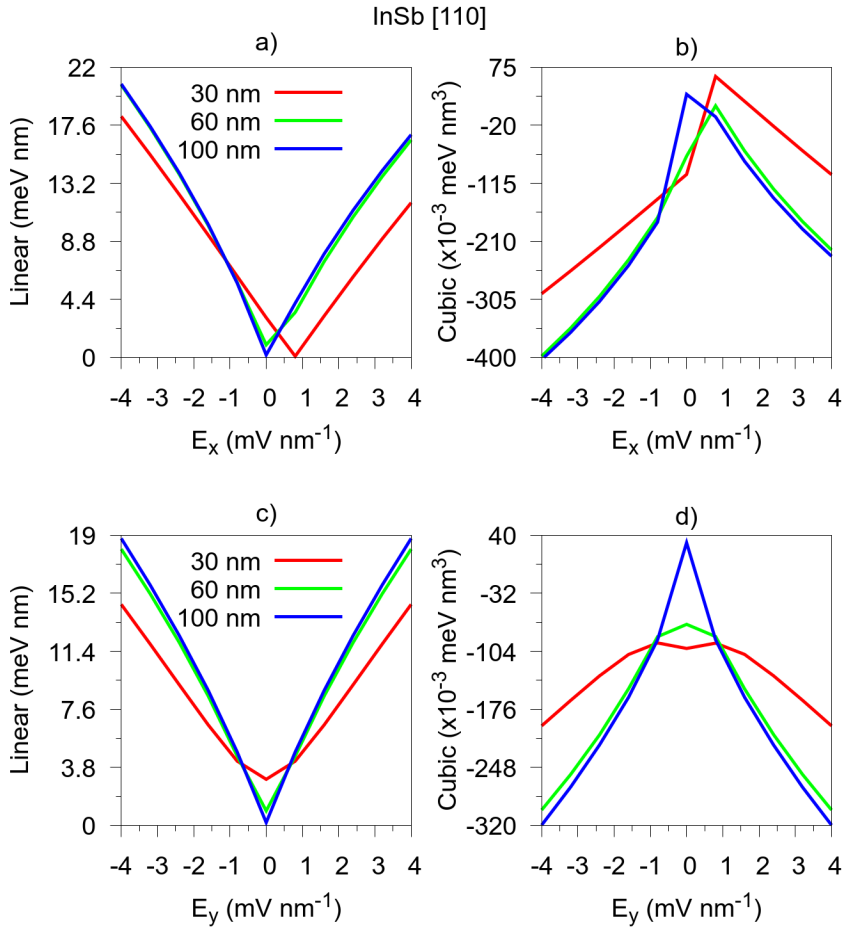


Figure 28: a) and c), linear spin-orbit splitting coefficients, ΔS_L ; b) and d) cubic spin-orbit splitting coefficients, ΔS_C , for different diameters L , for InSb zincblende nanowires oriented along [110]. In a) and b), the applied electric field goes along the x axis and in c) and d) along the y axis.

Source: By the author.

due to the interplay between BIA and SIA.

3.3.1.3 [111] oriented nanowires

We begin by showing the atomic arrangement, in Fig. 30a), of a zinc-blende nanowire oriented along [111] direction, and in Fig. 30b) its symmetry planes. The atoms in this direction do not have a complete C_{6v} symmetry. Since the confinement have itself a hexagonal, C_{6v} , symmetry we end-up with some symmetry planes in common. This mismatch allows for a confinement induced bulk inversion asymmetry which spin splits the nanowire subbands of small diameters and generates a spin orientation along the y axis.

In Fig. 31a) we show the subband dispersion of a zinc-blende InSb nanowire

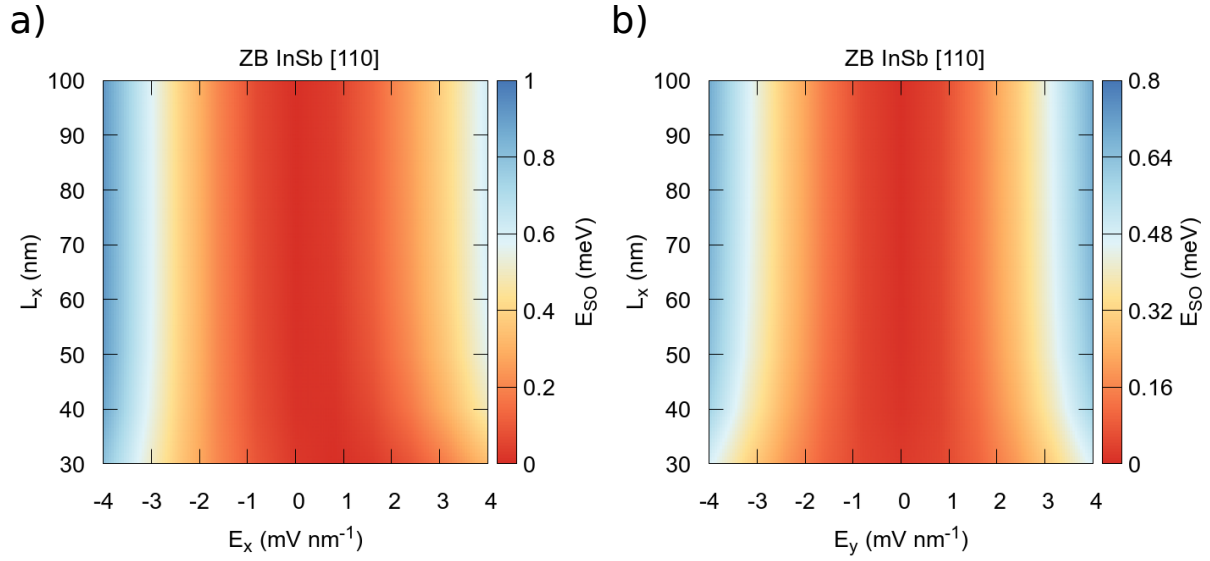


Figure 29: Calculated spin-orbit energy, for different diameters L_x and different transverse electric fields E , for InSb zincblende nanowires oriented along [110]. a) applied electric field along x axis and b) along y axis.

Source: By the author.

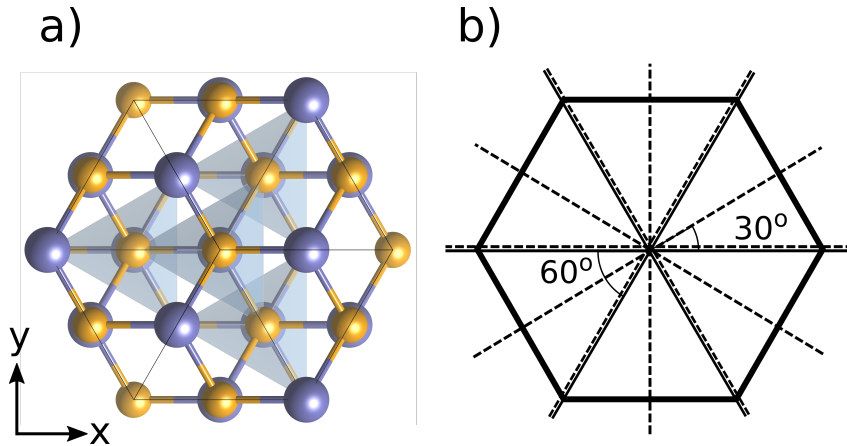


Figure 30: a) Atomic arrangement along [111] orientation of a zinc-blende structure with indicated x and y axis. b) Mirror symmetry planes of the atomic structure (solid) and of the hexagonal confinement (dashed).

Source: By the author.

oriented along [111] direction with $L = 60$ nm for the case with applied electric field, $|E_x| = 4$ mV/nm, along the x axis and on Fig. 31b) for a field, $|E_y| = 4$ mV/nm, along the y axis. In this orientation the subbands are similar to the [001] oriented case. The difference is that for high quantum confinement there is a small BIA related spin splitting

and when the electric field is present the electronic subbands becomes more spin split due to the SIA spin-orbit coupling.

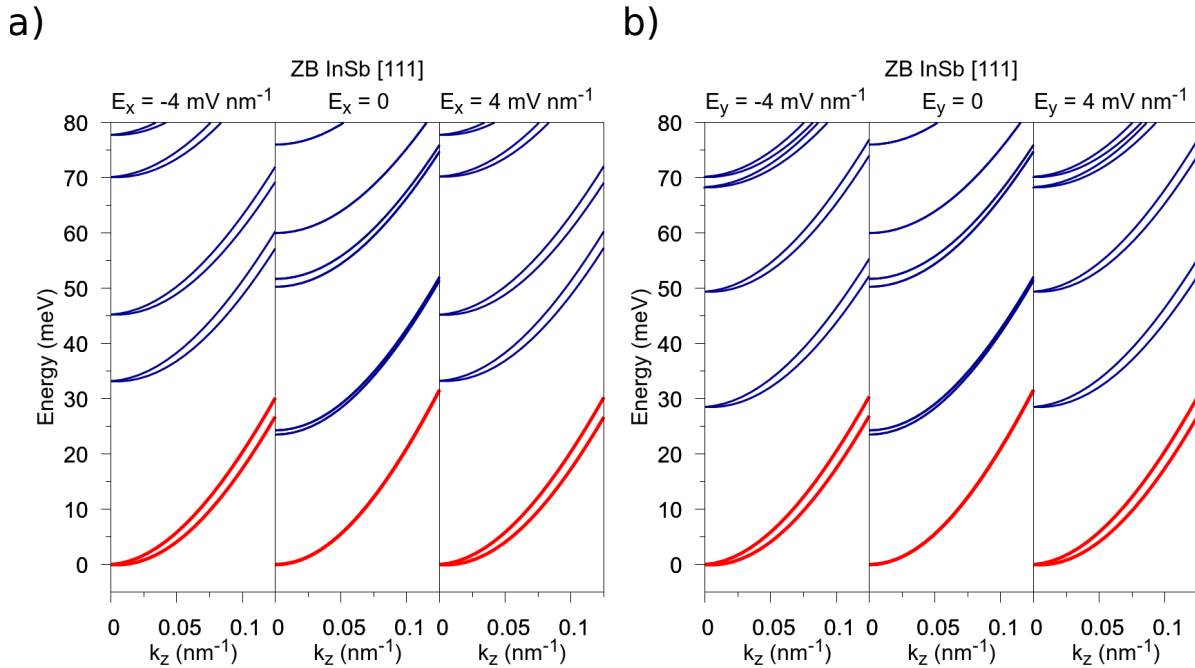


Figure 31: Calculated electronic subband dispersion for a zinc-blende InSb hexagonal nanowire of 60 nm diameter oriented along [111] direction. a) With applied electric field along x axis and b) along y axis. In each subfigure the left most spectrum corresponds to an electric field of $E = -4$ mV/nm, the central panel to zero applied electric field and the right most spectrum is for an electric field $E = 4$ mV/nm.

Source: By the author.

In Fig. 32 we show a zoom of the first subband of Fig. 31 to explicitly see the spin split. In a) we show the case with an negative electric field along the x axis, in b), the case without electric field and, in c) and d), the case with a positive applied electric field along the x and y axis, respectively. Here, as in the [110] case, there is no spin splitting for this specific nanowire diameter without an applied electric field. In the insets of panels a), b) and d) we see the linear behavior of the spin splitting due to the SIA spin-orbit coupling.

Given the first conduction subband, as in Fig. 32, we apply the numerical fitting method to obtain the effective masses, linear in momentum and cubic in momentum spin splitting parameters. In Fig. 33 we show the spin splitting parameters for three specific nanowire diameters, $L = 30$ nm, $L = 60$ nm and $L = 100$ nm, varying the applied electric field $E = -4, \dots, 4$ mV/nm along the x axis in panels a) and b), and along the y axis in

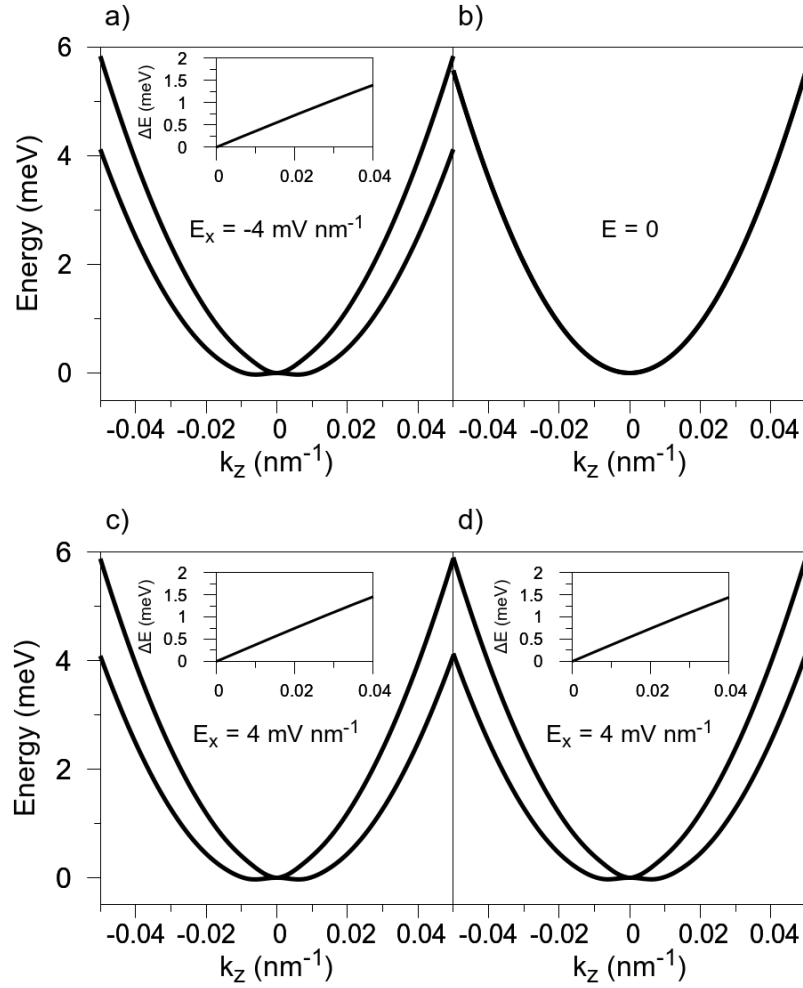


Figure 32: Zoom of the calculated first conduction subband of [111] oriented InSb zincblende nanowire at: a) finite electric field, $E_x = -4 \text{ mV/nm}$, along the x axis; b) zero field; c) finite electric field, $E_x = 4 \text{ mV/nm}$, along the x axis; and d) finite electric field, $E_y = 4 \text{ mV/nm}$, along the y axis. In the insets of a), c) and d) we show the SIA induced spin-orbit splitting of the first conduction subband.

Source: By the author.

panels c) and d). For this nanowire orientation we see that the spin splitting parameters, for electric field along x axis have a slight asymmetry but for electric field along y axis they are symmetric with respect to the applied electric field. Contrary to the [110] case, here the BIA spin-orbit coupling is not the maximum but is not also zero. Therefore the competition between BIA and SIA spin-orbit couplings accounts for the asymmetry but the BIA is not large enough to shift the degeneracy away from zero applied electric field. As in the other cases, for small diameters both linear and cubic spin splitting parameters have a linear dependence with the electric field and as the diameter increase this dependence

deviates from the linearity for large enough fields.

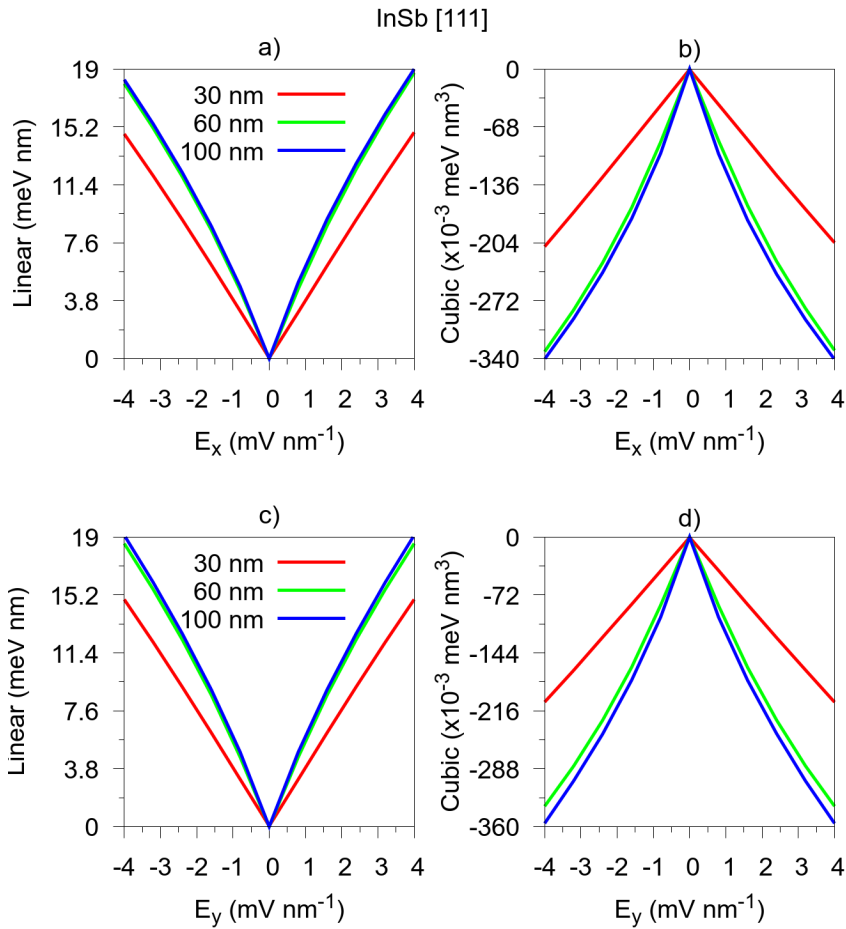


Figure 33: a) and c), linear spin-orbit splitting coefficients, ΔS_L ; b) and d) cubic spin-orbit splitting coefficients, ΔS_C , for different diameters L , for InSb zincblende nanowires oriented along [111]. In a) and b), the applied electric field goes along the x axis and in c) and d) along the y axis.

Source: By the author.

In Fig. 34 we show the density maps of the spin-orbit energy (see Eq. (3.3)) calculated for the first conduction subband using the fitted parameters shown in Fig. 33. In a) we show the case of applied electric field along the x axis and in b) along the y axis. The linear parameter, ΔS_L , shown in Fig. 33, presents a slight asymmetry with respect to large applied electric fields along the x axis, therefore we also see that E_{SO} presents such slight asymmetry. This is not the case for the electric field along y axis. As is the case of zinc-bende nanowires the general trend is that large values of E_{SO} come from large values of applied electric field.

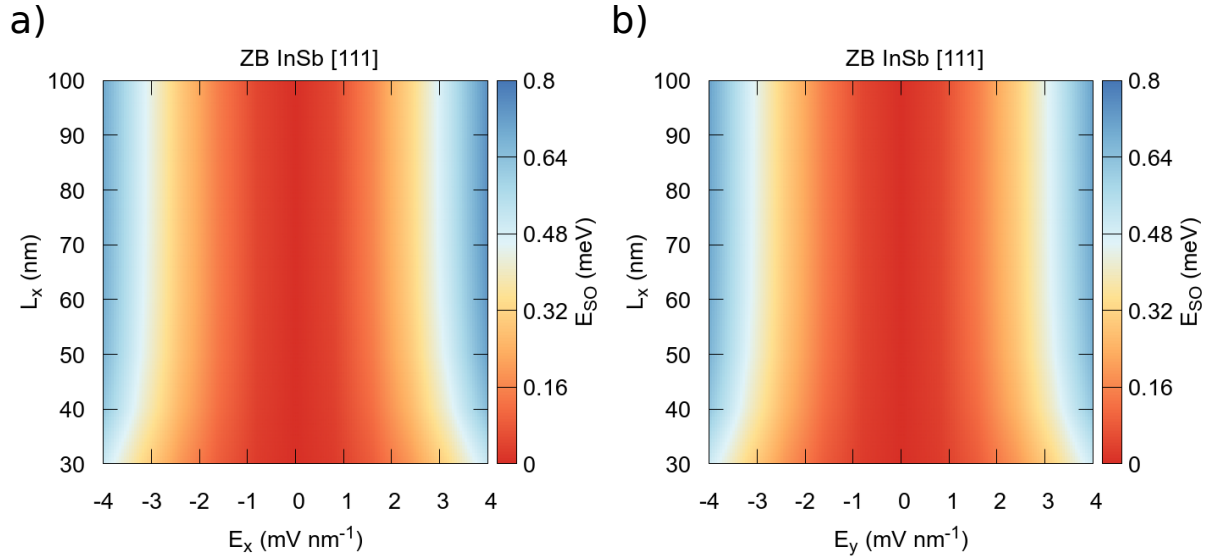


Figure 34: Calculated spin-orbit energy, for different diameters L_x and different transverse electric fields E , for InSb zincblende nanowires oriented along $[111]$. a) applied electric field along x axis and b) along y axis.

Source: By the author.

3.3.1.4 Discussion

The electronic band structure presented in Figs. 21, 26 and 31 have some interesting features. In the absence of applied electric fields we see that the second and third conduction subbands are almost degenerate, this effect arises from the hexagonal confinement. In our hexagonal confinement, the size along the x direction is larger than the size along y direction, therefore the wave functions that spread more along the x direction are energetically favorable to the more confined y direction. This effect is also seen in more energetic subbands, but it becomes less pronounced as we go to higher subbands since their wave functions spread more uniformly on the nanowire cross section, we found that our results are in qualitative agreement with tight-binding calculations reported on Ref. 116. Also, comparing the band structure with electric field applied along x or y direction we see that, depending on the orientation of the electric field, the subbands' energy values at Γ -point, vary accordingly to the combined effect of the hard wall hexagonal confinement profile and the electric field confinement. We found that for electric field along y direction, the difference in energy between second and third subbands is larger than the case for electric field along x , the opposite behavior was observed for the fourth and fifth subbands.

To further analyze the effects of the spin-orbit coupling let us take into consideration the intrinsic BIA related coupling present in bulk zinc-blende nanostructures. In Eq. (2.128) we see that the functional form of the BIA have a cubic momentum dependence, also preserved when we explicit write the BIA spin-orbit field along [110] and [111] directions (see Eqs. (2.129) and Eqs. (2.130) respectively). But what happens to the BIA spin-orbit coupling when we confine, with a hard wall, in the xy plane making a free-standing nanowire?

To answer this question taking into consideration only the first conduction subband, we projected^{134,135} the BIA Hamiltonian and found that, for nanowires oriented along [001] direction the BIA spin-orbit coupling gives us a linear in momentum spin split contribution (see Eq. (2.138)). Analyzing the atomic arrangement and symmetry planes of this orientation (see Fig. 20), we notice that the only allowed direction for spin polarization is z . Furthermore, for nanowires oriented along [111] direction we also get a linear in momentum spin splitting, but now its atomic arrangement and symmetries allows a spin polarization along y , because we have a matching symmetry plane leaving invariant changes like $y \rightarrow -y$, see Fig. 20. In both cases, [001] and [111], the bulk formalism predict the absence of BIA spin-orbit fields. In the confined case, due to the projection, the more confined the system the larger the BIA contribution. Hence, for large wires oriented along [001] and [111] direction we recover the bulk case (showing the absence of spin-orbit field). Moreover, nanowires oriented along [110] direction have, in the confined regime, a linear and cubic in momentum contributions to the spin splitting with spin polarization along y direction, contrasting with the bulk formalism that predicts only a cubic in momentum contribution to the spin splitting with the spin polarization in the xy plane. Analyzing Fig. 25, we see that the only matching symmetry between the atomic arrangement and the confining shape is the one that leaves invariant the mirror $y \rightarrow -y$, therefore allowing spin polarization along y direction.

We have seen that the BIA spin-orbit coupling drastically changes in the confined regimes if compared to the bulk case. Physically, the changes in BIA term for confined systems can be understood as an interfacing effect with the vacuum. If, in the bulk, the inversion asymmetry arises from the presence of two different atoms in the base of the Bravais lattice, when confined the atoms in the interface lose their neighbors, the asymmetry increases. The ratio of edge atom to bulk atoms increases as we decrease the

nanowire diameter, hence, increasing the contribution of this interface asymmetry to the BIA term.¹⁹⁶ Therefore, when we induce a structural asymmetry via the electric field, we have at least two cases: i) the application of $E = E_0\hat{x}$ induces a SIA spin-orbit coupling with spin polarization along the y direction and; ii) the application of $E = E_0\hat{y}$ induces a SIA spin-orbit coupling with spin polarization along the x direction. Both cases have a functional form for the spin splitting which is linear in momentum. In case i) both BIA and SIA have spin polarization along the same direction (exception made for [001] oriented nanowires), therefore their contributions interfere with each other and we could get a subband dispersion which is asymmetric (or have an asymmetric spin splitting) with respect to the sign of the applied electric field, as we see in Figs. 27 and 32.¹²⁹ In case ii) we do not have interferences between BIA and SIA, because they always point in distinct directions, and the spin splitting parameters are always symmetric with respect to the applied electric field, see Figs. 22c), 28d) and 33d).

A distinction between our hard wall nanowires and quantum wires electrically defined is that, in the former, the confinement in the xy plane have very similar strengths, therefore it couples the electron dynamics in all three dimensions, which is not the case in the latter system where the confinement is much weaker than underlying quantum well confinement.¹⁰⁰ This distinction means that the Rashba model (SIA spin-orbit coupling, see Eq. (2.127)), describes very well the decoupled case (electrically defined quantum wire) but it should fail in some point for the hard wall case. The failure is seen as a deviation from the linear dependence with the electric field of the associated spin splitting parameter. Moreover, since in quantum wire systems the Rashba coefficient, described as α_R in Table 3 and associated equations, is given by the underlying asymmetry in the quantum well, it should remain invariant under changes in the electrical confinement. On the other hand, for hard wall confinement, the Rashba coefficient strictly depends on the geometric configuration of the system. Therefore, changes in the quantum confinement also change the Rashba coefficient.^{100,133}

Indeed, taking Figs. 23, 28 and 33 we see that for large confinements, $L = 30$ nm, the spin splitting coefficients, both linear and cubic in momentum, have a linear dependence with the applied electric field. However as we increase the wire diameter to $L = 60$ nm we already see that this linear dependence holds only for small values of electric field. Moreover, comparing the spin split parameters for diameters $L = 60$ nm and $L = 100$ nm

we see that they almost do not change. Hence, we can say that the Rashba parameter has a dependence on the nanowire diameter: it is small for thin wires and grows up to a saturation value for large diameters. Also, the simplified Rashba model does not predict a cubic in momentum dependence for spin splitting parameters for nanowires oriented along [001] and [111] direction, see Table 3. However, since we are using the full multi band Hamiltonian and not the simplified Rashba model, we realistically capture all the features of full model which includes: i) the dependence of the Rashba parameters with quantum confinement; ii) the deviation of linearity for large electric fields and iii) the presence of the cubic in momentum dependence of the spin splitting parameters, absent in the original Rashba model.

To clearly see this dependence on the nanowire diameter and applied electric field, in Figs. 24, 29 and 34, we show the density maps of the spin-orbit coupling energy, given by Eq. (3.3), which explicitly takes into account the linear Rashba parameter. We see that for diameters $L \geq 50$ nm the spin-orbit coupling energy becomes stable to changes in the nanowire diameter and only depends on the applied electric field. This is a consequence of Rashba coefficient's saturation. We also see that for all cases, the spin-orbit energy maximum value is of the order of $E_{\text{SO}} \approx 1$ meV which is about half of the ones for wurtzite InAs nanowires, as we shall see in the following section.

In Figs. 35-37 we show the spin orientation for the zinc-blende InSb nanowires. According to Eqs. (2.138) we see that the spin orientations of the first subband of the nanowires without an applied electric field, that is due to BIA spin-orbit coupling, is: i) for [001] oriented nanowires along the z axis; ii) [110] oriented nanowires along the y axis; and iii) [111] oriented nanowires also along the y axis. When we applied an electric field we get an extra contribution due to the SIA spin-orbit coupling which is perpendicular to both the field direction as well as the free direction of the nanowire. Therefore for fields along x axis, the spin orientation is along the y and for fields along y axis, along the x axis. Hence, the general case is a combination of both spin-orbit contributions that can mix with each other but the magnitude of the SIA contribution is about one order of magnitude higher than the BIA ones.

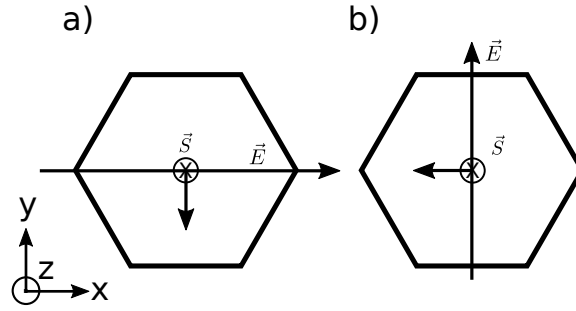


Figure 35: Spin orientation of [001] oriented zincblende nanowires. With electric field applied along a) x axis and b) y -axis.

Source: By the author.

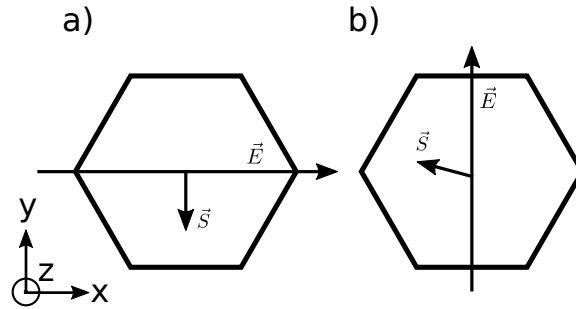


Figure 36: Spin orientation of [110] oriented zincblende nanowires. With electric field applied along a) x axis and b) y -axis. The tiled arrow in b) represents the mixing of BIA and SIA spin-orbit coupling, actually the BIA contribution to the spin orientation is about 1/10 of the SIA contribution.

Source: By the author.

3.3.2 Wurtzite InAs nanowires

Now let us discuss the effects of the quantum confinement and of the spin-orbit coupling in wurtzite systems. We begin with wurtzite nanowires oriented along [0001], [10 $\bar{1}$ 0] and [11 $\bar{2}$ 0] direction showing the calculated subband dispersion, i. e. energy as a function of free momentum k_z . We discuss the effects of the quantum confinement taking in account the crystal symmetry in the specific orientation and then we show spin splitting and the spin-orbit energy changes as we modify both applied electric field and nanowire diameter.

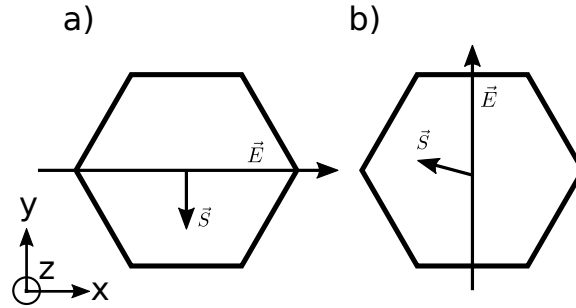


Figure 37: Spin orientation of $[111]$ oriented zincblende nanowires. With electric field applied along a) x axis and b) y -axis. The tiled arrow in b) represents the mixing of BIA and SIA spin-orbit coupling, actually the BIA contribution to the spin orientation is about $1/10$ of the SIA contribution.

Source: By the author.

3.3.2.1 $[0001]$ oriented nanowires

We begin by showing the atomic arrangement, in Fig. 38a), of a wurtzite nanowire oriented along $[0001]$ direction, and in Fig. 38b) its symmetry planes. In the bulk WZ crystal, there is glide symmetry plane which needs an extra $\frac{c}{2}$ dislocation along the z axis. Since the NWs are grown along the z direction, this symmetry plane also applies. Therefore, no confinement spin splitting induced by the bulk inversion asymmetry should appear.

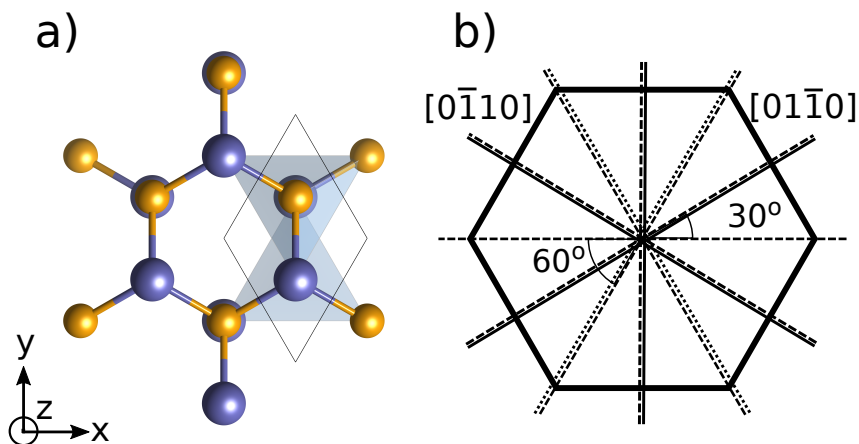


Figure 38: a) Atomic arrangement along $[0001]$ orientation of a wurtzite structure with indicated x and y axis. b) Mirror symmetry planes of the atomic structure (solid) and of the hexagonal confinement (dashed). In b), the dotted line represents the WZ glide planes, i. e., they need an extra translation of $\frac{c}{2}$ along the z direction.

Source: By the author.

In Fig. 39a) we show the subband dispersion of a wurtzite InAs nanowire oriented along [0001] direction with $L = 60$ nm for the case with applied electric field, $|E_x| = 4$ mV/nm, along the x axis and, on Fig. 39b) for a field, $|E_y| = 4$ mV/nm, along the y axis. For the case without electric field, the subbands are degenerate in spin but when the electric field is present the electronic subbands are spin split due to the spin-orbit coupling. Here, the spin splitting due SIA spin-orbit coupling is rather small, if compared to the zinc-blende [110] oriented nanowire, as we can see by the small spin splitting generated by the large electric field.

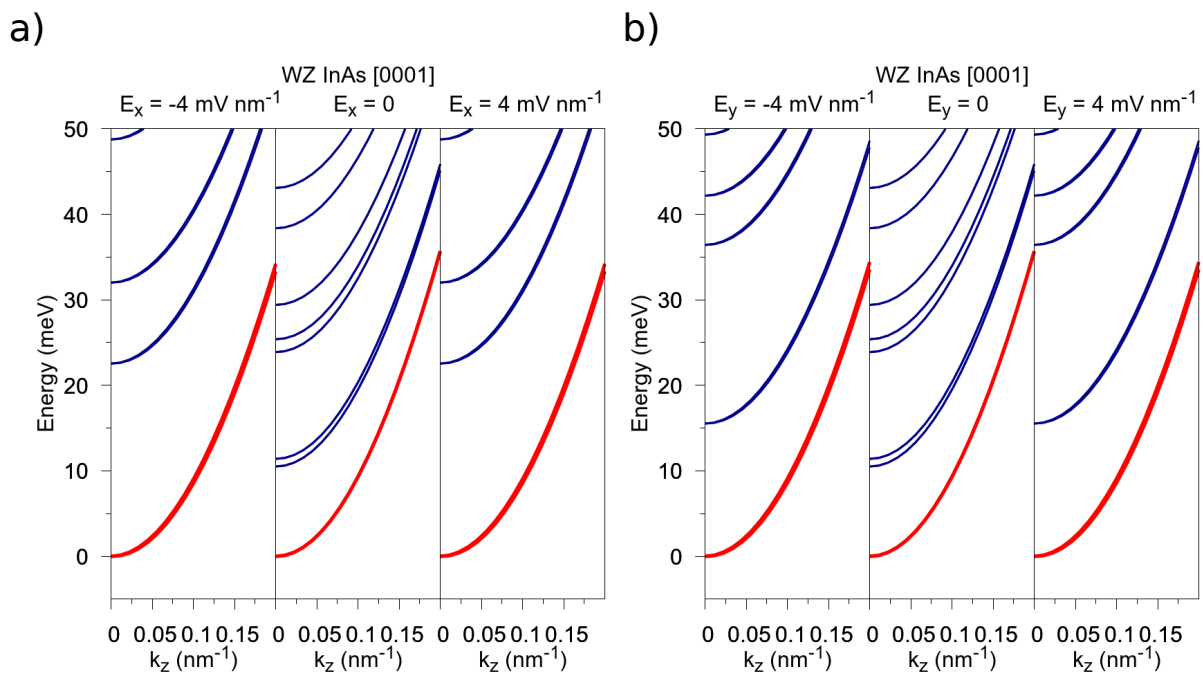


Figure 39: Calculated electronic subband dispersion for a wurtzite InAs hexagonal nanowire of 60 nm diameter oriented along [0001] direction. a) With applied electric field along x axis and b) along y axis. In each subfigure the left most spectrum corresponds to an electric field of $E = -4$ mV/nm, the central panel to zero applied electric field and the right most spectrum is for an electric field $E = 4$ mV/nm.

Source: By the author.

In Fig. 40 we show a zoom of the first subband of Fig. 39 to explicitly see the spin splitting. In a) we show the case without electric field and we can see that indeed there is no splitting. In panels b) and c) we show the zoom of the first subband for the case of an electric field applied along the x and y axis, respectively. In the insets we see the spin splitting of the subband which is linear with respect to the momentum. This linear

behavior is characteristic of a SIA related spin-orbit coupling.

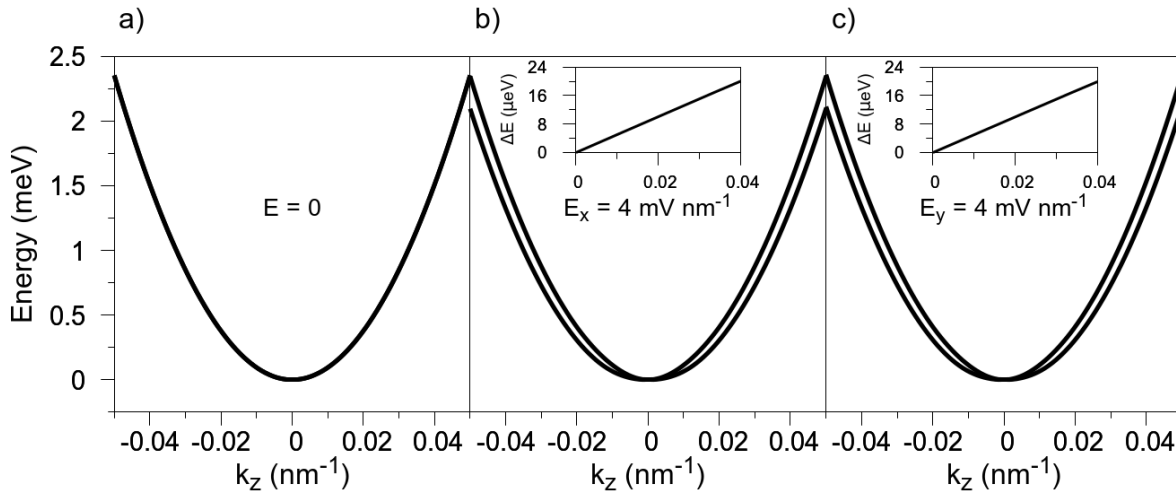


Figure 40: Zoom of the calculated first conduction subband of [0001] oriented InAs wurtzite nanowire at: a) zero; b) finite electric field, $E_x = 4$ mV/nm, along the x axis; and c) finite electric field, $E_y = 4$ mV/nm, along the y axis. In b) and c) we show, in the insets, the SIA induced spin-orbit splitting of the first conduction subband.

Source: By the author.

Given the first conduction subband, as in Fig. 40, we apply the numerical fitting method to obtain the effective masses, linear in momentum and cubic in momentum spin splitting parameters. In Fig. 41 we show the spin splitting parameters for three specific nanowire diameters, $L = 30$ nm, $L = 60$ nm and $L = 100$ nm, varying the applied electric field $E = -4, \dots, 4$ mV/nm along the x axis in panels a) and b), and along the y axis in panels c) and d). For this nanowire orientation we see that the spin splitting parameters are symmetric with respect to both orientations of the applied electric field. Here, contrary to the zinc-blende case, the spin splitting parameters do not change with the nanowire diameter and they have a non linear dependence with the applied electric field.

In Fig. 42 we show the density maps of the spin-orbit energy (see Eq. (3.3)) calculated for the first conduction subband using the fitted parameters shown in Fig. 41. In a) we show the case of applied electric field along the x axis and in b) along the y axis. Since the linear parameter, ΔS_L , shown in Fig. 41, is symmetric with respect to the applied electric field so is the spin-orbit coupling energy. For [0001] oriented wurtzite nanowires the general trend is that large values of E_{SO} come from large values of applied electric field. However for this specific orientation they are rather small.

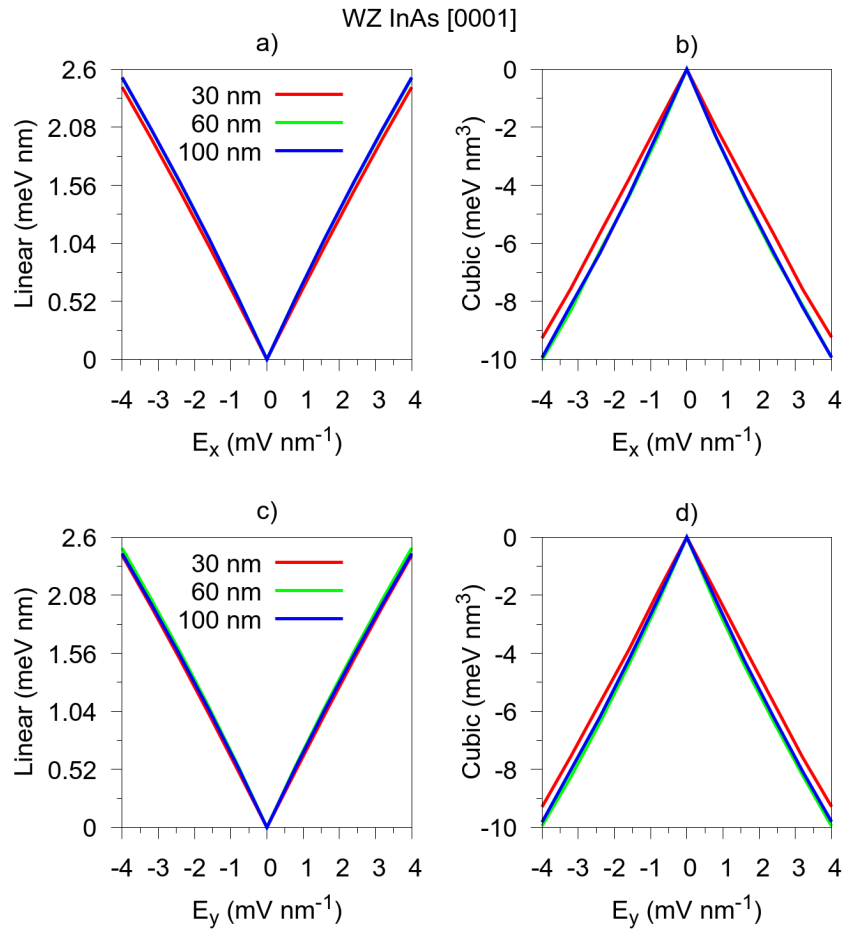


Figure 41: a) and c), linear spin-orbit splitting coefficients, ΔS_L ; b) and d) cubic spin-orbit splitting coefficients, ΔS_C , for different diameters L , for InAs wurtzite nanowires oriented along [0001]. In a) and b), the applied electric field goes along the x axis and in c) and d) along the y axis.

Source: By the author.

3.3.2.2 $[10\bar{1}0]$ and $[11\bar{2}0]$ oriented nanowires

We begin by showing the atomic arrangement, in Fig. 43a), of a wurtzite nanowire oriented along $[10\bar{1}0]$ direction, and in Fig. 43b) its symmetry planes. In Fig. 44, we also show the arrangement of a wurtzite nanowire oriented along $[11\bar{2}0]$ direction, and its symmetry planes. The atoms in the $[11\bar{2}0]$ direction do not have a specific symmetry, but in the $[10\bar{1}0]$ direction they have a C_2 symmetry with respect to the xz plane. Since the confinement have itself a hexagonal, C_{6v} , symmetry we end-up with only the invariance $y \rightarrow -y$. This lack of common symmetry together with the intrinsic BIA related spin-orbit coupling of these directions, allows a huge spin splitting of the bands.

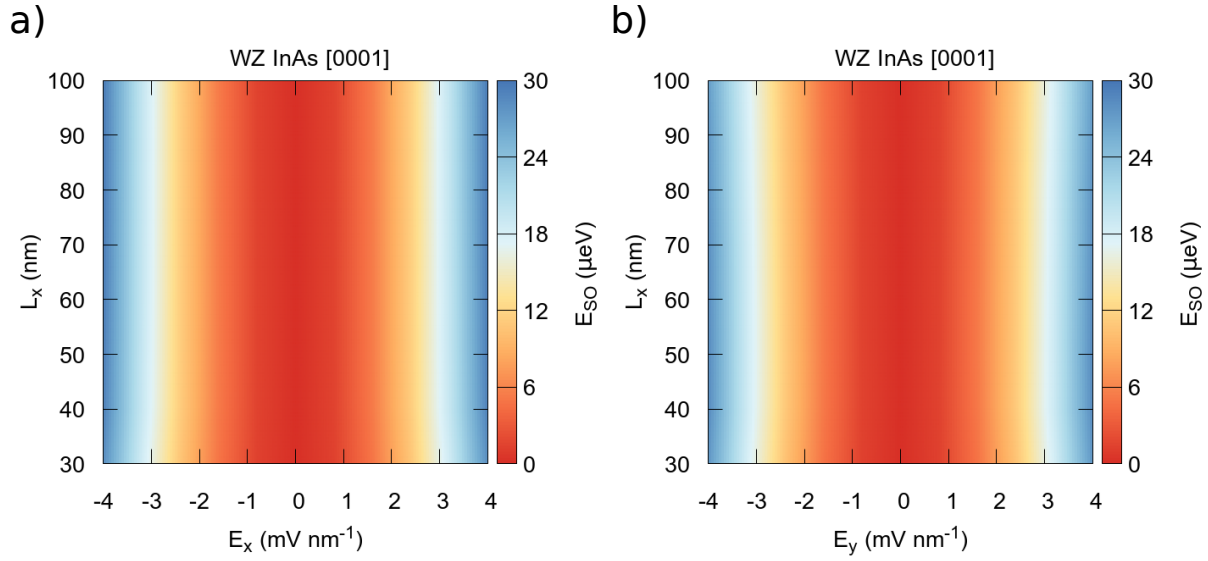


Figure 42: Calculated spin-orbit energy, for different diameters L_x and different transverse electric fields E , for InAs wurtzite nanowires oriented along $[0001]$. a) applied electric field along x axis and b) along y axis.

Source: By the author.

In Fig. 45a) we show the subband dispersion of a wurtzite InAs nanowire oriented along $[10\bar{1}0]$ or $[11\bar{2}0]$ direction with $L = 60$ nm for the case with applied electric field, $|E_x| = 4$ mv/nm, along the x axis and, on Fig. 45b) for a field, $|E_y| = 4$ mv/nm, along the y axis. For the case without electric field, the subbands have already a large spin splitting due to the intrinsic spin-orbit coupling for these specific directions. Moreover, as the the spin splitting due to the SIA spin-orbit coupling is rather small for wurtzite InAs when we apply an electric field the already large spin splitting almost suffers no change.

In Fig. 46 we show a zoom of the first subband of Fig. 45 to explicitly see the spin splitting. In a) we show the case with a negative electric field along the x axis, and in b) for the case without electric field and, in c) and d), with a positive applied electric field along the x and y axis, respectively. Here, contrary to the $[0001]$ case, we see in the inset of b) that the subband is spin split due to confinement induced by the BIA spin-orbit coupling. In the insets of a), b) and d) we see the linear behavior of the spin splitting due to the SIA spin-orbit coupling. However, in the wurtzite case, the BIA spin-orbit coupling already have a linear contribution, see Eq. (2.139), which dominates over the SIA spin-orbit coupling.

Given the first conduction subband, as in Fig. 46, we apply the numerical fitting

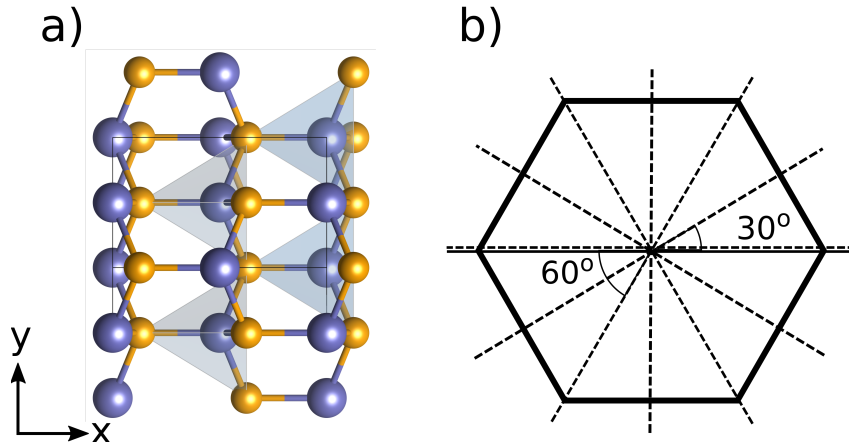


Figure 43: a) Atomic arrangement along $[10\bar{1}0]$ orientation of a wurtzite structure with indicated x and y axis. b) Mirror symmetry planes of the atomic structure (solid) and of the hexagonal confinement (dashed).

Source: By the author.

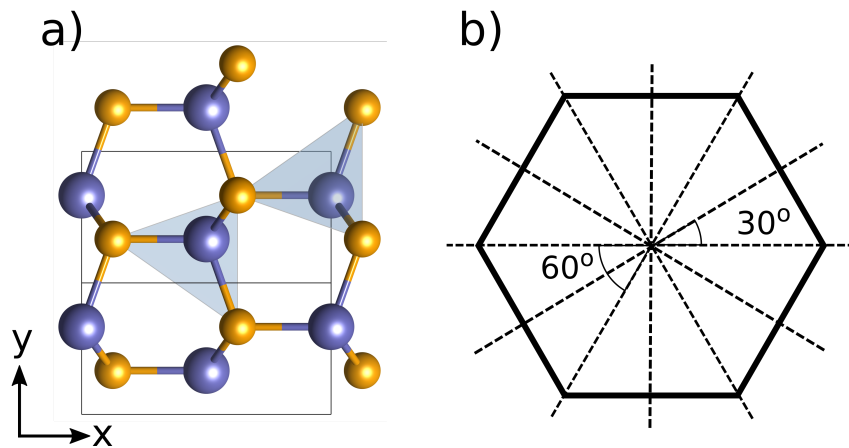


Figure 44: a) Atomic arrangement along $[11\bar{2}0]$ orientation of a wurtzite structure with indicated x and y axis. b) Mirror symmetry planes of the atomic structure (solid) and of the hexagonal confinement (dashed).

Source: By the author.

method to obtain the effective masses, linear in momentum and cubic in momentum spin splitting parameters. In Fig. 47 we show the spin splitting parameters for three specific nanowire diameters, $L = 30$ nm, $L = 60$ nm and $L = 100$ nm, varying the applied electric field $E = -4, \dots, 4$ mV/nm along the x axis in a) and b), and along the y axis in c) and d). For this nanowire orientation we see that the spin splitting parameters, for electric field along x axis are not symmetric but for electric field along y axis they are. This asymmetry

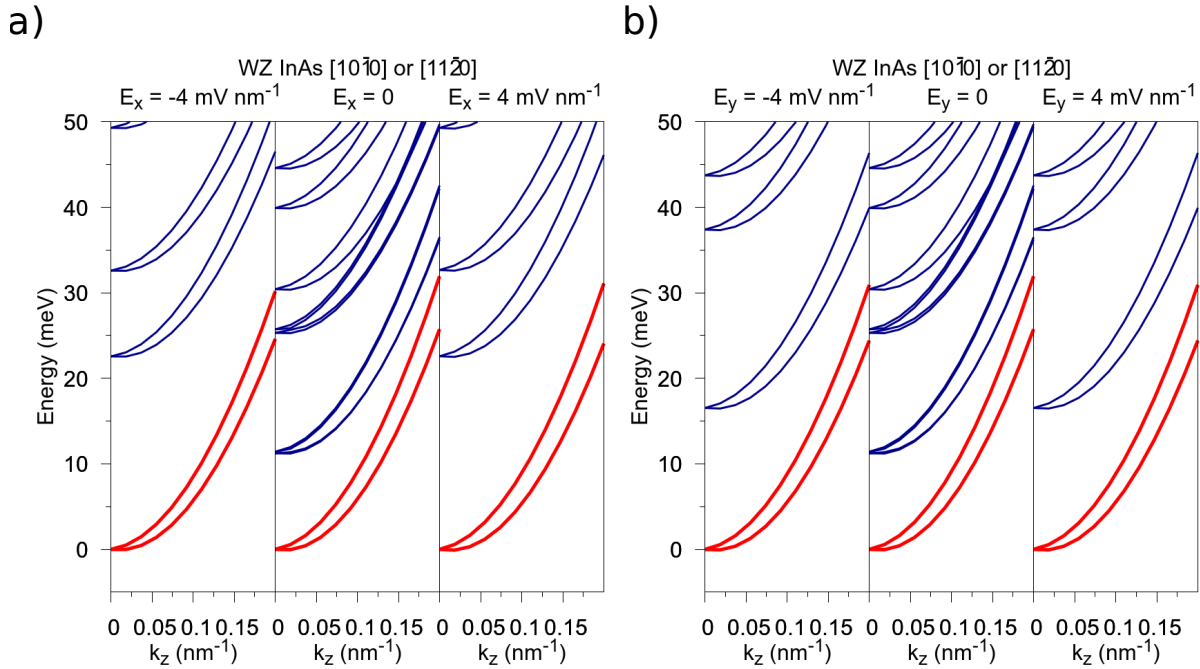


Figure 45: Calculated electronic subband dispersion for a wurtzite InAs hexagonal nanowire of 60 nm diameter oriented along $[10\bar{1}0]$ or $[11\bar{2}0]$ direction. a) With applied electric field along x axis and b) along y axis. In each subfigure the left most spectrum corresponds to an electric field of $E = -4$ mV/nm, the central panel to zero applied electric field and the right most spectrum is for an electric field $E = 4$ mV/nm.

Source: By the author.

arises from the interplay between the BIA and SIA spin-orbit couplings. Whereas for $[0001]$ orientend wurtzite the BIA spin-orbit coupling is absent, for $[10\bar{1}0]$ and $[11\bar{2}0]$ it is maximum.

In Fig. 48 we show the density maps of the spin-orbit energy (see Eq. (3.3)), calculated for the first conduction subband using the fitted parameters shown in Fig. 47. In a) we show the case of applied electric field along the x axis and in b) along the y axis. Since the linear parameter, ΔS_L , shown in Fig. 47, presents an asymmetry with respect to the applied electric field, along the x axis, we see that E_{SO} also presents such asymmetry. For electric fields along y axis we see that the spin-orbit coupling energy remains constant in all the parameter space but for a special case of a large nanowire diameter and zero applied electric field, where the rather large intrinsic BIA spin-orbit coupling dominates. Here we have two trends for the values of E_{SO} : i) for electric fields along x axis positive values of E_x give larger E_{SO} ; and for electric fields along y axis a value of $|E_y| = 1$ mV/nm

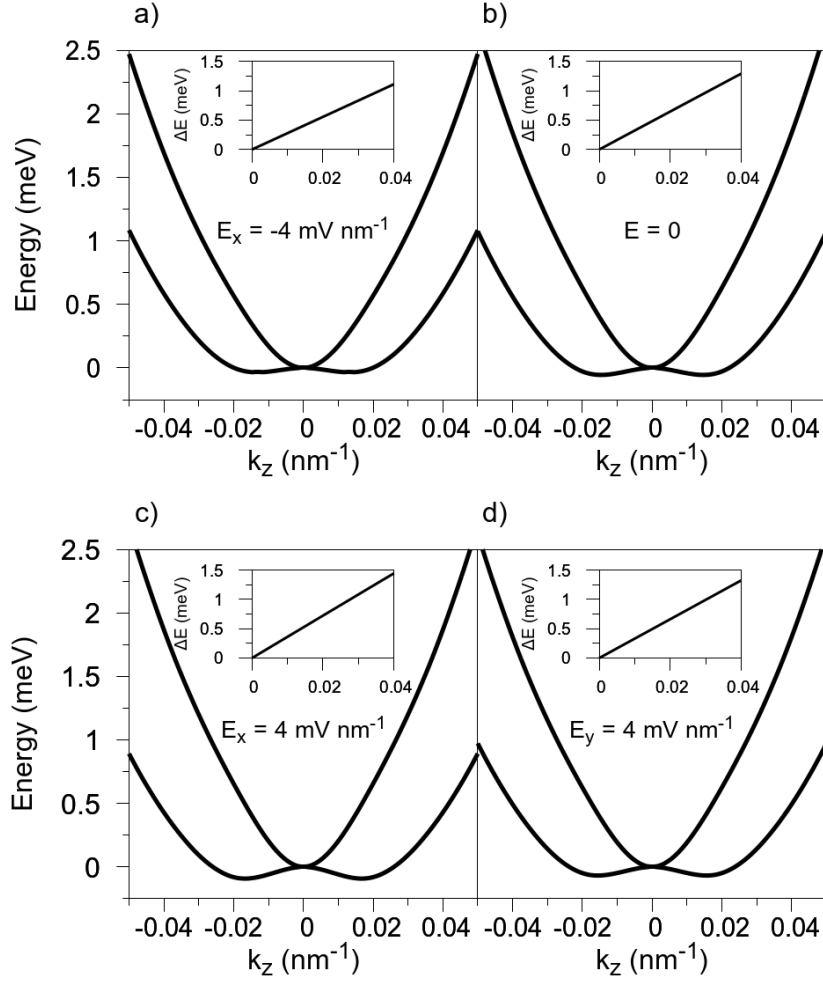


Figure 46: Zoom of the calculated first conduction subband of $[10\bar{1}0]$ or $[11\bar{2}0]$ oriented InAs wurtzite nanowire at: a) finite electric field, $E_x = -4 \text{ mV/nm}$, along the x axis; b) zero field; c) finite electric field, $E_x = 4 \text{ mV/nm}$, along the x axis; and d) finite electric field, $E_y = 4 \text{ mV/nm}$, along the y axis. In b), in the inset, we show the confinement BIA induced spin-orbit splitting and in a), c) and d), the SIA induced spin-orbit splitting of the first conduction subband.

Source: By the author.

is sufficient to saturate the E_{SO} to its maximum value.

3.3.2.3 Discussion

As in the zinc-blende case, the electronic band structure presented in Figs. 39 and 45 have some interesting features. In the absence of applied electric fields we see that the second and third conduction subbands are almost degenerate, but interesting enough for $[10\bar{1}0]$ or $[11\bar{2}0]$ due to the strong BIA spin-orbit coupling the subbands mix heavily. Up to date, we could not find any other work dedicated to the electronic band

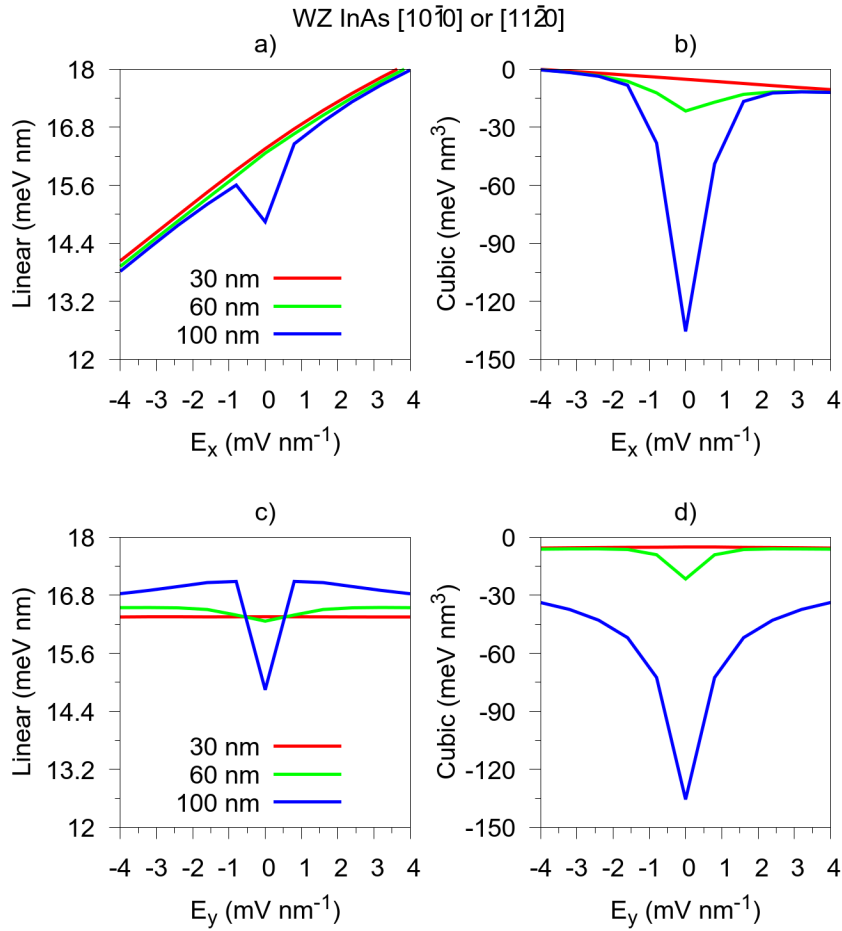


Figure 47: a) and c), linear spin-orbit splitting coefficients, ΔS_L ; b) and d) cubic spin-orbit splitting coefficients, ΔS_C , for different diameters L , for InAs wurtzite nanowires oriented along $[10\bar{1}0]$ or $[11\bar{2}0]$. In a) and b), the applied electric field goes along the x axis and in c) and d) along the y axis.

Source: By the author.

structure of wurtzite nanowires. However, our Hamiltonian is a state of the art one with parameters fitted to reproduce ab-initio bulk band structure.¹⁴⁴ Also, our Hamiltonian was used recently to reproduce experimental g-factor data.⁸⁶

To further analyze the effects of the spin-orbit coupling let us take into consideration the intrinsic BIA related spin-orbit coupling present in bulk wurtzite nanostructures. In Eq. (2.131) we see that functional form of the BIA has a linear plus a cubic in momentum dependence, also preserved when we explicitly write the BIA spin-orbit field along $[0001]$ and $[10\bar{1}0]$ or $[11\bar{2}0]$ directions, see Eq. (2.132). Again we ask: what happens to the BIA spin-orbit coupling when we confine, with a hard wall, in the xy plane making a free-standing nanowire?

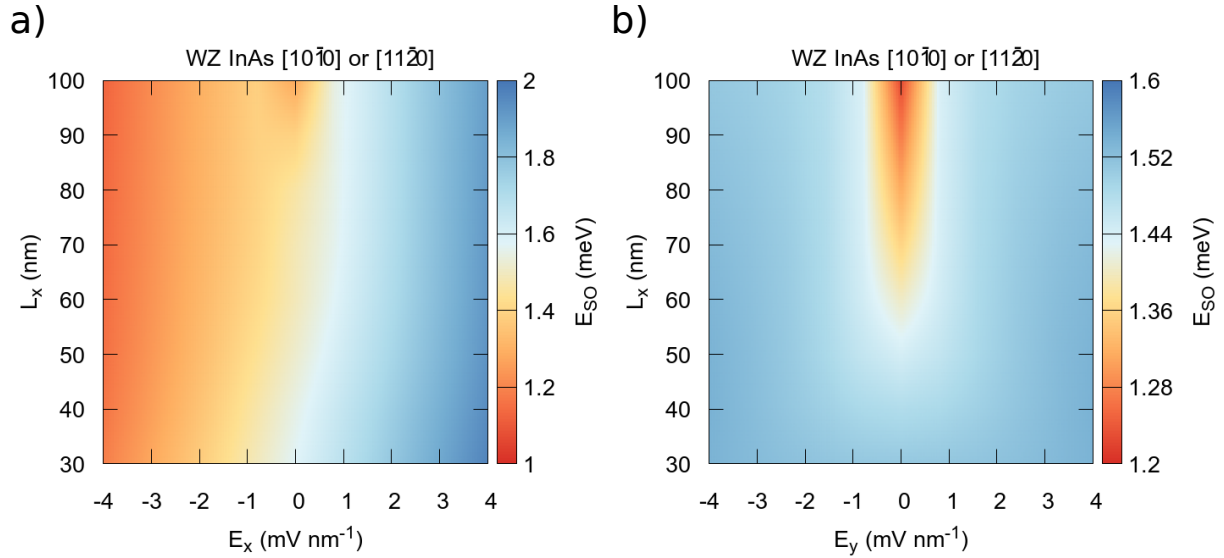


Figure 48: Calculated spin-orbit energy, for different diameters L_x and different transverse electric fields E , for InAs wurtzite nanowires oriented along $[10\bar{1}0]$ or $[11\bar{2}0]$. a) applied electric field along x axis and b) along y axis.

Source: By the author.

To answer this question taking into consideration only the first conduction subband, we projected^{134,135} the BIA Hamiltonian and found that (see Eqs. (2.139)) for nanowires oriented along $[0001]$ direction, the BIA spin-orbit is absent. Furthermore, for nanowires oriented along $[10\bar{1}0]$ or $[11\bar{2}0]$ directions, we see a linear-plus-cubic in momentum spin splitting, with the atomic arrangement and symmetries allowing a spin polarization along y , see Figs. 43 and 44. In the case of $[0001]$ direction the bulk formalism predicts the absence of BIA spin-orbit fields but in the case of $[10\bar{1}0]$ or $[11\bar{2}0]$, the bulk expression gives us non zero BIA terms. In the confined case, due to the projection, the more confined the system, the larger the BIA contribution is, but is worth mentioning that the linear term that appears in wurtzite is rather large, of the order of $\alpha^{\text{WZ}} = 0.3 \text{ eV}\text{\AA}$.¹⁰⁹ Therefore, we should expect that nanowires oriented along these directions should give already a large spin splitting parameters.

We have seen that the BIA spin-orbit coupling does not change much in the confined regimes if compared to the bulk case. Again, when we induce a structural asymmetry via the electric field, we obtain at least two cases: i) with $E = E_0\hat{x}$, a SIA spin-orbit coupling is induced with spin polarization along y direction and; ii) with $E = E_0\hat{y}$, a SIA spin-orbit coupling is induced with spin polarization along x direction. Both cases have a functional

form for the spin splitting that is linear in momentum. In case i) both BIA and SIA have spin polarizations along the same direction (exception made for [0001] oriented nanowires, which does not have BIA related spin splitting). Therefore, their contributions interfere with each other and we see a subband dispersion that is asymmetric (or an asymmetric spin splitting) with respect to the sign of the applied electric field, as we see in Fig. 46. In case ii) we do not have interferences between BIA and SIA, because they always point in distinct directions, and the spin splitting parameters are always symmetric with respect to the applied electric field, see Fig. 46d).

Since in wurtzite nanostructures there is already a linear term that appears from the bulk inversion asymmetry, many authors call this contribution as the Rashba model.^{148,187} Rashba itself derived its model based on wurtzite nanostructures,¹⁹⁷ but here, we are interested not in the linear contribution that arises from bulk inversion asymmetry, but from the linear term that arises from structural inversion asymmetry.⁵⁵ The Rashba parameter is usually expressed, for quantum well structures, as $\alpha(z) = \frac{\partial}{\partial z}\beta(z)$ ⁶⁷ where $\beta(z)$ express the dependence of the Rashba parameter with the pertinent energies of the system, i. e., the gap and spin-orbit coupling splittings. In Ref. 198, the authors provided an expression for β , based on the 8-band Kane like model for wurtzite, which reads

$$\beta = P_1 P_2 \frac{\Delta_3}{(E_v + \Delta_1 - \Delta_2 + V - \epsilon)(E_v + V - \epsilon) - 2\Delta_3^2} \quad (3.4)$$

where $\Delta_{2,3}$ are the spin-orbit interaction parameters, Δ_1 the crystal field interaction, E_v accounts for the heterostructure offset and ϵ is the energy of the given state and V is some external potential.

Following Refs. 198 and 130 we can find the Rashba parameter for wurtzite assuming that $E_v \rightarrow 0$ and $\epsilon \rightarrow E_c = E_g + \Delta_1 + \Delta_2$. Therefore, we can write the Rashba parameters as

$$\alpha = P_1 P_2 \frac{\Delta_3 (2E_g + \Delta_1 + 3\Delta_2 - 2V(z))}{[(E_g + \Delta_2 - V(z))(E_g + \Delta_1 + \Delta_2 - V(z)) - 2\Delta_3^2] \frac{\partial}{\partial z} V(z)} \quad (3.5)$$

giving a dependence with the external potential times its derivative (in our case the electric field), and not only with its derivative as in the zinc-blende case. This dependence indicates a distinct behavior as we see in Fig. 41, where the spin split parameters does not depend on the nanowire diameter.

From the linear spin splitting coefficient, showed in Fig. 41, we can extract the Rashba coefficient for wurtzite nanowires oriented along $[0001]$ direction. Since the Rashba coefficient is small for wurtzite nanostructures, we expect that the spin splitting for $[10\bar{1}0]$ or $[11\bar{2}0]$ oriented nanowires is dominated by the BIA spin orbit coupling. Indeed, in Fig. 47, we see that the spin splitting parameters have almost the same values for all nanowire diameters. When we applied an electric field along the x axis both, BIA and SIA, interfere with each other giving an asymmetric behavior to the spin splitting parameters, as seen on Figs. 47a) and 47b). On the other hand, for electric field applied on the y axis they do not interfere and we see a symmetric behavior for the spin splitting parameters, as seen on Figs. 47c) and 47d). The dip in all plots for zero electric field comes from the BIA spin orbit coupling where, for large nanowires $\beta_1^{\text{WZ}} \rightarrow 0$, and only α^{WZ} contributes to ΔS_L , see Table 3.

To see the dependence on the nanowire diameters and applied electric fields, in Figs. 42 and 48, we show the density maps of the spin-orbit coupling energy, given by Eq. (3.3), which explicitly takes into account the linear Rashba parameter. In Fig. 42 we show the E_{SO} for $[0001]$ oriented wurtzite nanowires and it only depends on the applied electric field with its maximum values of the order of $E_{\text{SO}} \approx 30 \mu\text{eV}$, which is very tiny. On the other hand, in Fig. 48 we show E_{SO} for $[10\bar{1}0]$ or $[11\bar{2}0]$ oriented wurtzite nanowires and in it we see that the values are much higher, of the order of $E_{\text{SO}} \approx 2 \text{ meV}$ and minimum of $E_{\text{SO}} \approx 1 \text{ meV}$, which is double of the the zincblende nanowires values.

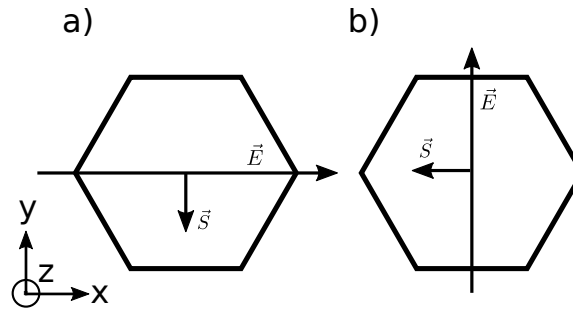


Figure 49: Spin orientation of $[0001]$ oriented wurtzite nanowires. With electric field applied along a) x axis and b) y -axis.

Source: By the author.

In Figs. 49 and 50 we show the spin orientation for the wurtzite InAs nanowires. According to Eqs. (2.139) we see that the spin orientations of the first subband of the

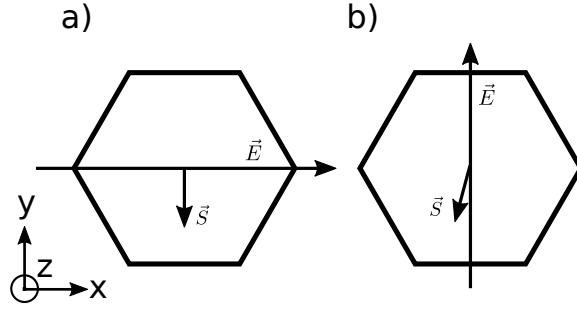


Figure 50: Spin orientation of $[10\bar{1}0]$ or $[11\bar{2}0]$ oriented wurtzite nanowires. With electric field applied along a) x axis and b) y -axis. The tiled arrow in b) represents the mixing of BIA and SIA spin-orbit coupling, actually the SIA contribution to the spin orientation is about 1/10 of the BIA contribution.

Source: By the author.

nanowires without an applied electric field, that is due to BIA spin-orbit coupling, is: i) for $[0001]$ oriented nanowires, absent; ii) for $[10\bar{1}0]$ or $[11\bar{2}0]$ oriented nanowires, along the y axis. When we applied an electric field we got an extra contribution due to the SIA spin-orbit coupling which is perpendicular to both the field direction as well as the free direction of the nanowire. Therefore, for fields along x axis, we see a spin orientation along the y and for field along y axis we get a spin orientation along the x axis. Hence, the general case is a combination of both spin-orbit contributions that can mix with each other. In $[0001]$ case, there is only the SIA spin-orbit coupling. For $[10\bar{1}0]$ or $[11\bar{2}0]$, the BIA magnitude, contrary to the zinc-blende case, is higher than the SIA by about one order of magnitude.

3.4 Superconductor proximity effects

Now that we have a complete characterization of the nanowires, let us study the superconducting proximity effects. We used Eq. (2.158) that is described in the Nambu spinor basis $\Psi(\vec{r}) = [u_{\uparrow}(\vec{r}), u_{\downarrow}(\vec{r}), v_{\downarrow}(\vec{r}), -v_{\uparrow}(\vec{r})]^T$ and we assume, for simplicity, that $\Delta_0(\vec{r})$ is constant and real. For the system to undergo the topological phase transition it has to be gapped before we couple it to the superconductor, then with a change in the parameters it has to close the gap and reopen again. At $k_z = 0$, the gap is defined by $E(0) = |V_Z - \sqrt{\Delta^2 + \mu^2}|$. The trivial phase is defined when $V_Z < \sqrt{\Delta^2 + \mu^2}$, the phase transition (closing of the gap) when $V_Z = \sqrt{\Delta^2 + \mu^2}$ and the topological phase is defined when $V_Z > \sqrt{\Delta^2 + \mu^2}$.^{28,29,32,33}

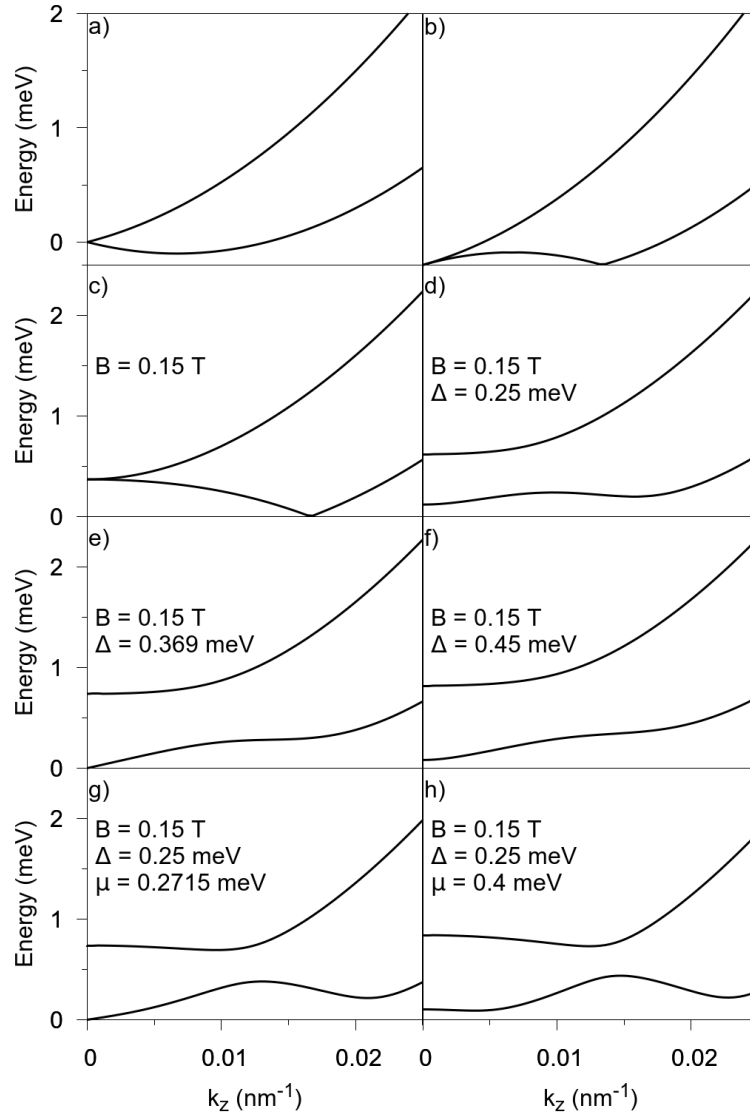


Figure 51: Zinc-blende InSb nanowire with $L = 100$ nm with magnetic field applied along the nanowire axis (and perpendicular to the spin-orbit coupling) and superconductivity proximity effect. a) Lowest subband spectrum for $\mu = B = \Delta = 0$. b) Excitation spectrum of the creation or annihilation of an electron for $\mu = B = \Delta = 0$. c) Excitation spectrum for $B = 0.15$ T, $\Delta = \mu = 0$ where Zeeman splitting opens a gap at $k_z = 0$. d) $B = 0.15$ T, $\Delta = 0.25$ meV, $\mu = 0$ with a superconducting gap for $k_z \neq 0$ and a Zeeman gap near $k_z = 0$. e) $B = 0.15$ T, $\Delta = 0.369$ meV, $\mu = 0$ meaning $V_z = \Delta$ where the gap at $k_z = 0$ is closed meaning a phase transition. f) $B = 0.15$ T, $\Delta = 0.45$ meV, $\mu = 0$ here the gap reopens confirming the phase transition. g) $B = 0.15$ T, $\Delta = 0.25$ meV, $\mu = 0.2715$ meV meaning $V_z^2 = \Delta^2 + \mu^2$, the gap at $k_z = 0$ also closes driven by the changes in the chemical potential. h) $B = 0.15$ T, $\Delta = 0.25$ meV, $\mu = 0.4$ meV the gap at $k_z = 0$ reopens, signaling the phase transition.

Using realistic parameters fitted from our multiband $\mathbf{k} \cdot \mathbf{p}$ calculations we see that for $L = 100$ nm zinc-blende InSb nanowires, the typical values which characterizes the

system are: $m^* \approx 0.017 m_0$, $\alpha \approx 0.3 \text{ eV \AA}$, $g_z^* \approx -85$, $V_Z \approx -2.46 \times B_0 \text{ meV}$ being B_0 , the magnetic field magnitude. These values are in agreement with experimental measurements³⁶ although they used the bulk g-factor which is about 60% lower than the ones we have obtained in previous sections. The proposed induced superconducting gap is $\Delta \approx 0.25 \text{ meV}$ and typical values for the magnetic field are of $B_0 \approx 0.15$.³⁶ In Fig. 51d) we show that the gap is open for $B = 0.15 \text{ T}$ and $\Delta = 0.25 \text{ meV}$, and that increasing the pairing potential, Δ , to match the Zeeman energy, the gap closes, see Fig. 51e). Further increasing the value of Δ , the gap reopens, see Fig. 51f). In Figs. 51g) and 51h) we also show that fixing a value of Δ , we can also induce the topological transition by changing the chemical potential.³² For a magnetic field applied along x or y direction the linear spin splitting coefficient does not change much but the value of the g-factor drops by a factor of 2. Hence a larger magnetic field should be used.

For [0001] wurtzite InAs oriented nanowires, we see that for $L = 100 \text{ nm}$, the typical values that characterize the system are: $m^* \approx 0.04 m_0$, $\alpha \approx 0.05 \text{ eV \AA}$, $g_x^* \approx -6.4$, $V_Z \approx -0.5788 \times B_0 \text{ meV}$. Experimental measurements³⁸ reported a pairing potential for InAs nanowires of $\Delta = 0.045 \text{ meV}$ and g-factor of $g^* \approx 20$ that is similar to our calculated g_z^* . Also, the typical values for magnetic field in this case are about $B = 0.06 \text{ T}$, but we have used a slightly higher field of $B = 0.1 \text{ T}$. In Fig. 52d) we show that the gap is opened for $B = 0.1 \text{ T}$ and $\Delta = 0.045 \text{ meV}$, and that increasing the pairing potential to match the Zeeman energy the gap closes, see Fig. 52e). Further increasing the value of Δ , the gap reopens, see Fig. 52f). In Figs. 52g) and 52h) we also show that fixing a value of Δ , we can also induce the topological transition by changing the chemical potential. For a magnetic field applied along x or y direction the linear spin-split coefficient does not change much but the value of the g-factor drops by a factor of 2. Hence, a larger magnetic field should be used.

On the other hand, for $[10\bar{1}0]$ or $[11\bar{2}0]$ wurtzite InAs oriented nanowires, we see that for $L = 100 \text{ nm}$ the typical values that characterize the system are: $m^* \approx 0.05 m_0$, $\alpha \approx 0.3 \text{ eV \AA}$, $g_x^* \approx -10$, $V_Z \approx -0.463 \times B_0 \text{ meV}$. In Fig. 53d), we show that the gap is opened for $B = 0.15 \text{ T}$ and $\Delta = 0.045 \text{ meV}$, and that increasing the pairing potential to match the Zeeman energy the gap closes, see Fig. 53e). Further increasing the value of Δ the gap reopens, see Fig. 53f). In Figs. 53g) and 53h) we also show that fixing a value of Δ , we can also induce the topological transition by changing the chemical potential.

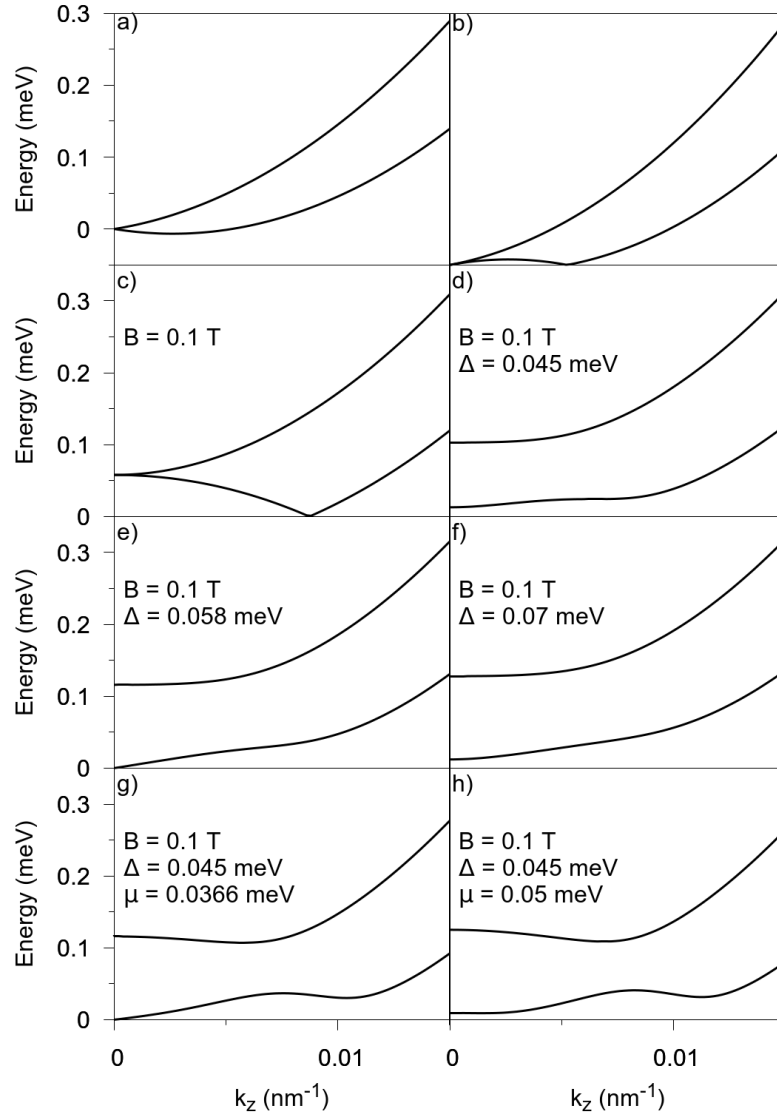


Figure 52: Wurtzite InAs nanowire oriented along $[0001]$ direction with $L = 100$ nm and magnetic field applied along the x axis (perpendicular to both the nanowire main axis and the spin-orbit coupling) and superconductivity proximity effect. a) Lowest subband spectrum for $\mu = B = \Delta = 0$. b) Excitation spectrum of the creation or annihilation of an electron for $\mu = B = \Delta = 0$. c) Excitation spectrum for $B = 0.1$ T, $\Delta = \mu = 0$ where Zeeman splitting opens a gap at $k_z = 0$. d) $B = 0.1$ T, $\Delta = 0.045$ meV, $\mu = 0$ with a superconducting gap for $k_z \neq 0$ and a Zeeman gap near $k_z = 0$. e) $B = 0.1$ T, $\Delta = 0.058$ meV, $\mu = 0$ meaning $V_z = \Delta$ where the gap at $k_z = 0$ is closed meaning a phase transition. f) $B = 0.1$ T, $\Delta = 0.07$ meV, $\mu = 0$ here the gap reopens confirming the phase transition. g) $B = 0.1$ T, $\Delta = 0.045$ meV, $\mu = 0.0366$ meV meaning $V_z^2 = \Delta^2 + \mu^2$, the gap at $k_z = 0$ also closes driven by changes in the chemical potential. h) $B = 0.1$ T, $\Delta = 0.045$ meV, $\mu = 0.05$ meV the gap at $k_z = 0$ reopens, signaling the phase transition.

Here, due to the high relative magnitudes of the spin-orbit coupling and induced pairing, the gap at $k_z = 0$ becomes tiny. For magnetic fields applied along x or y direction, the linear spin splitting coefficient does not change much but the value of the g-factor drops by a factor of 3 for the y direction and by a factor of 2 for the x direction. Hence, a larger magnetic field should be used.

Using our parameters, fitted from realistic $\mathbf{k} \cdot \mathbf{p}$ simulations, we explicitly showed that the InSb and InAs nanowires undergoes the topological phase transition, indeed, and could possibly host the zero-energy Majorana fermions. From this point on, one could start to study the stability of the topological superconducting phase, i. e., explore how to choose the chemical potential, spin-orbit coupling strength, proximity induced pairing potential and Zeeman splitting in order to maximize the bulk excitation gap.³³

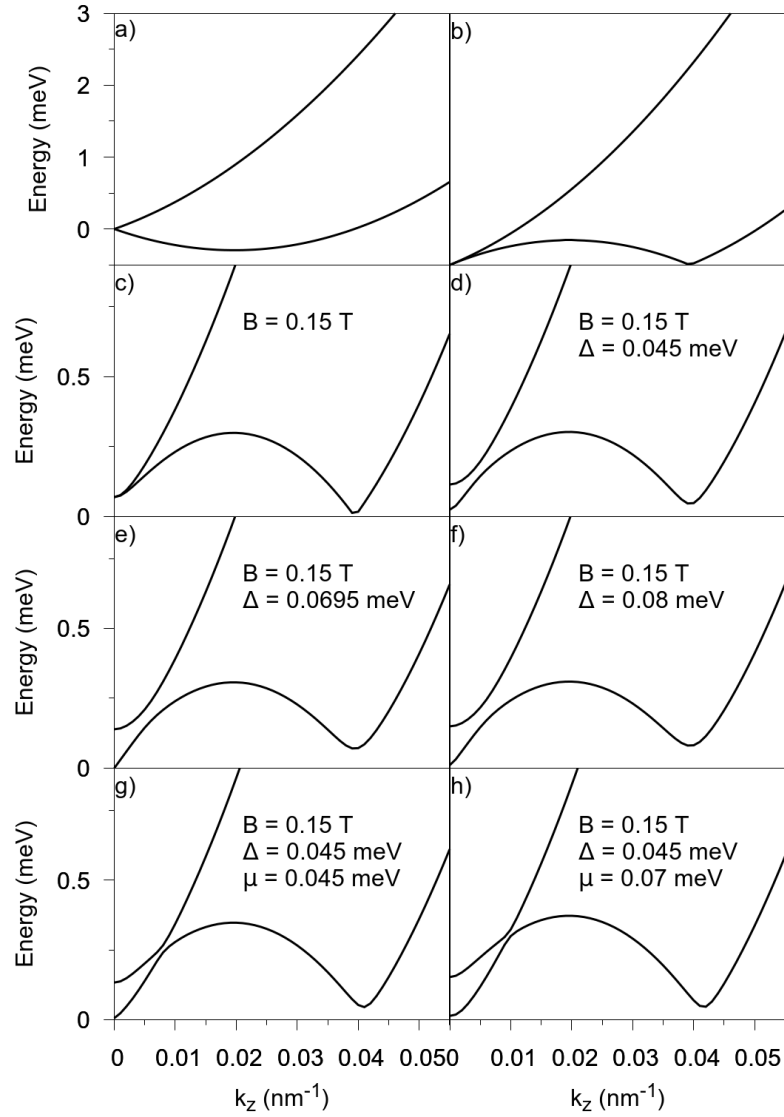


Figure 53: Wurtzite InAs nanowire oriented along $[10\bar{1}0]$ or $[11\bar{2}0]$ direction with $L = 100$ nm and magnetic field applied along the x axis (perpendicular to both the nanowire main axis and the spin-orbit coupling) and superconductivity proximity effect. a) Lowest subband spectrum for $\mu = B = \Delta = 0$. b) Excitation spectrum of the creation or annihilation of an electron for $\mu = B = \Delta = 0$. c) Excitation spectrum for $B = 0.15$ T, $\Delta = \mu = 0$ where Zeeman splitting opens a gap at $k_z = 0$. d) $B = 0.15$ T, $\Delta = 0.045$ meV, $\mu = 0$ with a superconducting gap for $k_z \neq 0$ and a Zeeman gap near $k_z = 0$. e) $B = 0.15$ T, $\Delta = 0.0695$ meV, $\mu = 0$ meaning $V_z = \Delta$ where the gap at $k_z = 0$ is closed meaning a phase transition. f) $B = 0.15$ T, $\Delta = 0.08$ meV, $\mu = 0$ here the gap reopens confirming the phase transition. g) $B = 0.15$ T, $\Delta = 0.045$ meV, $\mu = 0.045$ meV meaning $V_z^2 = \Delta^2 + \mu^2$, the gap at $k_z = 0$ also closes driven by changes in the chemical potential. h) $B = 0.15$ T, $\Delta = 0.045$ meV, $\mu = 0.07$ meV the gap at $k_z = 0$ reopens, signaling the phase transition.

4 CONCLUSION

In this Thesis we performed a systematic investigation of the spin-orbit interaction in hexagonal semiconductor nanowires under a transverse applied electric field. In specific, we focused in the first conduction subband of zinc-blende InSb and wurtzite InAs deriving compact expressions for the bulk inversion asymmetry (BIA) spin-orbit coupling mechanism that can be used in a 2×2 effective model. We also analyzed the interplay between the structural inversion asymmetry (SIA), induced by the transversal applied electric field, and the BIA. We used realistic multiband $\mathbf{k} \cdot \mathbf{p}$ Hamiltonians^{132,144} in the envelope function approximation and plane waves expansion to extract relevant physical parameters that describes the lowest energy band with high fidelity. Besides the spin-split parameters we also calculated the g-factor tensor and applied the BdG formalism (coupling with a superconductor) to find if, indeed, the nanowires undergo a topological phase transition.

We found that in zinc-blende InSb nanowires the BIA is influenced by the quantum confinement, with thin nanowires presenting larger spin-split than the thick ones. On the other hand, for wurtzite InAs nanowires there is an already large linear in momentum BIA coefficient in the bulk description which is not affect by quantum confinement, see Eq. (2.139). These BIA contribution remains unchanged for $[10\bar{1}0]$ or $[11\bar{2}0]$ oriented nanowires while BIA is absent for $[0001]$. Moreover, we found that the spin orientation for the lowest conduction subband is along y direction in all nanowires, except for $[110]$ zinc-blende oriented nanowires where it is along z direction. Furthermore, when we applied a transverse electric field, we found that the SIA spin-orbit coupling dominates the spin-split of zinc-blende nanowires whereas the contrary was observed for wurtzite, where the BIA dominates. Hence, the spin-orbit coupling in zinc-blende InSb nanowires can be fine tuned by external sources, such as gates and doping, while for wurtzite InAs the very crystal phase dictates the spin-orbit coupling.

Commonly, the SIA spin-orbit coupling is treated using the Rashba model that assumes a linear dependence on both the momentum and the applied electric field. Since we used a realistic multiband approach, where the spin-orbit coupling is built-in on the equations describing the system, we checked the validity of the Rashba model. We found that for high electric field the spin-split is no longer linear with the applied electric field.

Moreover, there is always a cubic momentum dependence in the spin-split, even when the BIA is absent.

Quantum confinement and spin-orbit coupling are also known to drastically change the g-factor tensor in low dimensional semiconductor nanostructures.^{4,76,80} Under the $\mathbf{k} \cdot \mathbf{p}$ perturbation theory, the g-factor tensor is easily obtained as a summation of the momentum matrix elements among the nanostructure quantum states.¹³² With our numerical approach we were able to compute it and found that quantum confinement quenches the g-factor value. For wurtzite nanowires oriented along [0001] direction we found that g_z^* grows linearly with the nanowire diameter while the in-plane g-factor saturates into the bulk value. Wurtzite nanowires oriented along $[10\bar{1}0]$ or $[11\bar{2}0]$ direction presented the same trend but with a cyclic permutation $x, y, z \rightarrow z, x, y$. Furthermore, we also found that the g-factors have an in-plane anisotropy related to the nanowire orientation and the spin-orbit coupling field.

Last, with our realistic set of parameters describing the first conduction band of the nanowires, we used the BdG formalism to describe the superconductivity induced effects and check if the system undergoes the topological phase transition. Indeed we found that they do undergo a phase transition with an effective p-wave pairing. Therefore, the hybrid semiconductor-superconductor proposal using nanowires with large spin-orbit coupling can indeed host the zero energy Majorana fermions.

In summary, our investigation of the spin-orbit coupling in nanowires showed that in zinc-blende InSb nanowires the spin-split of the energy bands can be fine tuned by external sources while in wurtzite InAs nanowires it is fixed by the crystal phase. These findings have implications in the field of spintronics where the precise control of the spin allows for more efficient device operation. Also, we showed that indeed the induced s-wave superconductivity pairing generates an effective p-wave pairing in the nanowires required for the topological phase transition that ultimately can guide the physics community into finding the zero energy Majorana modes in the hybrid setup. Finally, we like to point out that our methodology is not restricted to only these systems and can be used to study any low dimensional semiconductor nanostructures in any configuration.

4.1 Future activities and projects

The study of the g-factor is an active research field and has still some open questions. For example the in-plane anisotropy of the g-factor in quantum wells still needs further investigations.⁵ It is believed that the BIA spin-orbit coupling is responsible for the anisotropy and using our numerical approach we can try to answer this question. Furthermore, to our current knowledge this Thesis is the first to present some calculations about the g-factor for wurtzite InAs nanowires besides the common [0001] orientation. Other III-V compounds crystallize in the wurtzite crystal phase when grown as nanowires^{107,109} such as GaAs, GaSb, InSb and InP, for instance. We can definitely devise a Hamiltonian to describe these systems, as done in Ref. 144 and investigate their g-factors and their impact on spintronics applications. Indeed, the g-factor in these systems have experimental interest as, for instance, Ref. 90 studied the g-factor on InP wurtzite nanowires under high magnetic fields.

Another project that naturally follows this Thesis is the implementation of the BdG formalism using the full multiband $\mathbf{k} \cdot \mathbf{p}$ Hamiltonians. Since we already know that using only the first subband the system undergo the topological phase transition, what we can say when there is more than one subband occupied? In this way we can simulate the full hybrid setup, the contacts, and probe the existence of the Majorana fermions at the end of the wires and under which conditions they could really appear. Moreover, instead of applying an magnetic field there is also the possibility to induce an exchange potential in the nanowire via a magnetic layer.^{32,33} Using a magnetic layer instead of an applied magnetic field has the advantage to not break the superconductivity since the magnetization is being induced only in the region of interest. Our approach has also been used to study the magnetic properties of diluted magnetic systems^{199,200} and can also be used to probe the induced exchange potential inside the nanowire.

REFERENCES

- 1 WANG, J. et al. Highly polarized photoluminescence and photodetection from single indium phosphide nanowires. **Science**, v. 293, n. 5534, p. 1455, 2001.
- 2 COUTO, O. D. D. et al. Anisotropic spin transport in (110) GaAs quantum wells. **Physical Review Letters**, v. 98, n. 3, p. 036603, 2007.
- 3 NEFYODOV, Y. A. et al. g -factor anisotropy in a GaAs/Al_xGa_{1-x}As quantum well probed by electron spin resonance. **Physical Review B**, v. 83, n. 4, p. 041307, 2011.
- 4 SANDOVAL, M. A. T. et al. Mesoscopic spin-orbit effect in the semiconductor nanostructure electron g factor. **Physical Review B**, v. 86, n. 19, p. 195302, 2012.
- 5 QIAN, X. et al. Anisotropic in-plane spin dynamics in (110)-oriented GaAs/AlGaAs multiple quantum well. **Journal of Applied Physics**, v. 121, n. 15, p. 153901, 2017.
- 6 KANE, C. L.; MELE, E. J. Quantum spin hall effect in graphene. **Physical Review Letters**, v. 95, n. 22, p. 226801, 2005.
- 7 BERNEVIG, B. A.; HUGHES, T. L.; ZHANG, S.-C. Quantum spin Hall effect and topological phase transition in HgTe quantum wells. **Science**, v. 314, n. 5806, p. 1757, 2006.
- 8 SINOVA, J. et al. Spin hall effects. **Reviews of Modern Physics**, v. 87, n. 4, p. 1213, 2015.
- 9 ŽUTIĆ, I.; FABIAN, J.; SARMA, S. D. Spintronics: fundamentals and applications. **Reviews of Modern Physics**, v. 76, n. 2, p. 323, 2004.
- 10 DERY, H. et al. Spintronic nanoelectronics based on magneto-logic gates. **IEEE Transactions on Electronic Devices**, v. 59, n. 259, 2012.
- 11 SINOVA, J.; JUNGWIRTH, T. Surprises from the spin hall effect. **Physics Today**, v. 70, n. 7, p. 38, 2017.
- 12 SHULAKER, M. M. et al. Carbon nanotube computer. **Nature**, v. 501, n. 7468, p. 526, 2013.
- 13 ŽUTIĆ, I.; FARIA JUNIOR, P. E. Semiconductor lasers: taken for a spin. **Nature Nanotechnology**, v. 9, n. 10, p. 750, 2014.
- 14 FARIA JUNIOR, P. E. et al. Toward high-frequency operation of spin lasers. **Physical Review B**, v. 92, n. 7, p. 075311, 2015.
- 15 _____. Wurtzite spin lasers. **Physical Review B**, v. 95, n. 11, p. 115301, 2017.
- 16 HASAN, M. Z.; KANE, C. L. Colloquium: topological insulators. **Reviews of Modern Physics**, v. 82, n. 4, p. 3045, 2010.
- 17 QI, X.-L.; ZHANG, S.-C. Topological insulators and superconductors. **Reviews of Modern Physics**, v. 83, n. 4, p. 1057, 2011.

- 18 KLITZING, K. v.; DORDA, G.; PEPPER, M. New method for high-accuracy determination of the fine-structure constant based on quantized hall resistance. **Physical Review Letters**, v. 45, n. 6, p. 494, 1980.
- 19 GU, Z.-C.; WEN, X.-G. Tensor-entanglement-filtering renormalization approach and symmetry-protected topological order. **Physical Review B**, v. 80, n. 15, p. 155131, 2009.
- 20 CHEN, X.; GU, Z.-C.; WEN, X.-G. Classification of gapped symmetric phases in one-dimensional spin systems. **Physical Review B**, v. 83, n. 3, p. 035107, 2011.
- 21 CHEN, X.; LIU, Z.-X.; WEN, X.-G. Two-dimensional symmetry-protected topological orders and their protected gapless edge excitations. **Physical Review B**, v. 84, n. 23, p. 235141, 2011.
- 22 POLLMANN, F. et al. Symmetry protection of topological phases in one-dimensional quantum spin systems. **Physical Review B**, v. 85, n. 7, p. 075125, 2012.
- 23 PANKRATOV, O.; PAKHOMOV, S.; VOLKOV, B. Supersymmetry in heterojunctions: band-inverting contact on the basis of $\text{Pb}_{1-x}\text{Sn}_x\text{Te}$ and $\text{Hg}_{1-x}\text{Cd}_x\text{Te}$. **Solid State Communications**, v. 61, n. 2, p. 93, 1987.
- 24 KÖNIG, M. et al. Quantum spin hall insulator state in HgTe quantum wells. **Science**, v. 318, n. 5851, p. 766, 2007.
- 25 TIAN, J. et al. Observation of current-induced, long-lived persistent spin polarization in a topological insulator: a rechargeable spin battery. **Science Advances**, v. 3, n. 4, p. e1602531, 2017.
- 26 FU, L.; KANE, C. L. Superconducting proximity effect and Majorana fermions at the surface of a topological insulator. **Physical Review Letters**, v. 100, n. 9, p. 096407, 2008.
- 27 MAJORANA, E. Teoria simmetrica dell'elettrone e del positrone. **Il Nuovo Cimento (1924-1942)**, v. 14, n. 4, p. 171, 2008.
- 28 ELLIOTT, S. R.; FRANZ, M. Colloquium: Majorana fermions in nuclear, particle, and solid-state physics. **Reviews of Modern Physics**, v. 87, n. 1, p. 137, 2015.
- 29 ALICEA, J. New directions in the pursuit of Majorana fermions in solid state systems. **Reports on Progress in Physics**, v. 75, n. 7, p. 076501, 2012.
- 30 KITAEV, A. Unpaired Majorana fermions in quantum wires. **Physics-Uspekhi**, v. 44, n. 10S, p. 131, 2000.
- 31 SATO, M.; TAKAHASHI, Y.; FUJIMOTO, S. Non-abelian topological order in s -wave superfluids of ultracold fermionic atoms. **Physical Review Letters**, v. 103, n. 2, p. 020401, 2009.
- 32 SAU, J. D. et al. Generic new platform for topological quantum computation using semiconductor heterostructures. **Physical Review Letters**, v. 104, n. 4, p. 040502, 2010.
- 33 ALICEA, J. Majorana fermions in a tunable semiconductor device. **Physical Review B**, v. 81, n. 12, p. 125318, 2010.

- 34 OREG, Y.; REFAEL, G.; OPPEN, F. von. Helical liquids and Majorana bound states in quantum wires. **Physical Review Letters**, v. 105, n. 17, p. 177002, 2010.
- 35 LUTCHYN, R. M.; SAU, J. D.; SARMA, S. D. Majorana fermions and a topological phase transition in semiconductor-superconductor heterostructures. **Physical Review Letters**, v. 105, n. 7, p. 077001, 2010.
- 36 MOURIK, V. et al. Signatures of Majorana fermions in hybrid superconductor-semiconductor nanowire devices. **Science**, v. 336, n. 6084, p. 1003, 2012.
- 37 DENG, M. T. et al. Anomalous zero-bias conductance peak in a Nb–InSb nanowire–Nb hybrid device. **Nano Letters**, v. 12, n. 12, p. 6414, 2012.
- 38 DAS, A. et al. Zero-bias peaks and splitting in an Al-InAs nanowire topological superconductor as a signature of Majorana fermions. **Nature Physics**, v. 8, n. 12, p. 887, 2012.
- 39 LEE, E. J. H. et al. Zero-bias anomaly in a nanowire quantum dot coupled to superconductors. **Physical Review Letters**, v. 109, n. 18, p. 186802, 2012.
- 40 LIU, J. et al. Zero-bias peaks in the tunneling conductance of spin-orbit-coupled superconducting wires with and without Majorana end-states. **Physical Review Letters**, v. 109, n. 26, p. 267002, 2012.
- 41 PIKULIN, D. I. et al. A zero-voltage conductance peak from weak antilocalization in a Majorana nanowire. **New Journal of Physics**, v. 14, n. 12, p. 125011, 2012.
- 42 KELLS, G.; MEIDAN, D.; BROUWER, P. W. Near-zero-energy end states in topologically trivial spin-orbit coupled superconducting nanowires with a smooth confinement. **Physical Review B**, v. 86, n. 10, p. 100503, 2012.
- 43 VERNEK, E. et al. Subtle leakage of a Majorana mode into a quantum dot. **Physical Review B**, v. 89, n. 16, p. 165314, 2014.
- 44 RUIZ-TIJERINA, D. a. et al. Interaction effects on a Majorana zero mode leaking into a quantum dot. **Physical Review B**, v. 91, n. 11, p. 115435, 2015.
- 45 SCHARF, B.; ŽUTIĆ, I. Probing Majorana-like states in quantum dots and quantum rings. **Physical Review B**, v. 91, n. 14, p. 144505, 2015.
- 46 PRADA, E.; SAN-JOSE, P.; AGUADO, R. Transport spectroscopy of NS nanowire junctions with Majorana fermions. **Physical Review B**, v. 86, n. 18, p. 180503, 2012.
- 47 RAINIS, D. et al. Towards a realistic transport modeling in a superconducting nanowire with Majorana fermions. **Physical Review B**, v. 87, n. 2, p. 024515, 2013.
- 48 FRANZ, M. Majorana's wires. **Nature Nanotechnology**, v. 8, n. 3, p. 149, 2013.
- 49 SARMA, S. D.; SAU, J. D.; STANESCU, T. D. Splitting of the zero-bias conductance peak as smoking gun evidence for the existence of the Majorana mode in a superconductor-semiconductor nanowire. **Physical Review B**, v. 86, n. 22, p. 220506, 2012.
- 50 BEN-SHACH, G. et al. Detecting Majorana modes in one-dimensional wires by charge sensing. **Physical Review B**, v. 91, n. 4, p. 045403, 2015.

- 51 YOU, J.-B. et al. Majorana transport in superconducting nanowire with Rashba and Dresselhaus spin-orbit couplings. **Journal of Physics: condensed matter**, v. 27, n. 22, p. 225302, 2015.
- 52 Zhang, H. et al. **Ballistic Majorana nanowire devices**. 2016. Available from: <https://arxiv.org/pdf/1603.04069.pdf>. Accessible at: 25 Jul. 2017.
- 53 HE, Q. L. et al. Chiral Majorana fermion modes in a quantum anomalous hall insulator-superconductor structure. **Science**, v. 357, n. 6348, p. 294, 2017.
- 54 DRESSELHAUS, G. Spin-orbit coupling effects in zinc blende structures. **Physical Review**, v. 100, n. 2, p. 580, 1955.
- 55 BYCHKOV, Y. A.; RASHBA, E. Properties of a 2D electron gas with lifted spectral degeneracy. **JETP Letters**, v. 39, n. 2, p. 78, 1984.
- 56 BERNEVIG, B. A.; ORENSTEIN, J.; ZHANG, S.-C. Exact SU(2) symmetry and persistent spin helix in a spin-orbit coupled system. **Physical Review Letters**, v. 97, n. 23, p. 236601, 2006.
- 57 KORALEK, J. D. et al. Emergence of the persistent spin helix in semiconductor quantum wells. **Nature**, v. 458, n. 7238, p. 610, 2009.
- 58 SCHLIEMANN, J.; EGUES, J. C.; LOSS, D. Nonballistic spin-field-effect transistor. **Physical Review Letters**, v. 90, n. 14, p. 146801, 2003.
- 59 DATTA, S.; DAS, B. Electronic analog of the electro-optic modulator. **Applied Physics Letters**, v. 56, n. 7, p. 665, 1990.
- 60 RAINIS, D.; LOSS, D. Conductance behavior in nanowires with spin-orbit interaction: a numerical study. **Physical Review B**, v. 90, n. 23, p. 235415, 2014.
- 61 ZAWADZKI, W.; PFEFFER, P. Spin splitting of subband energies due to inversion asymmetry in semiconductor heterostructures. **Semiconductor Science and Technology**, v. 19, n. 1, p. R1, 2004.
- 62 THORGILSSON, G. et al. Rashba spin orbit interaction in a quantum wire superlattice. **Physical Review B**, v. 85, n. 4, p. 045306, 2012.
- 63 NOWAK, M. P.; SZAFRAN, B. Spin-polarization anisotropy in a narrow spin-orbit-coupled nanowire quantum dot. **Physical Review B**, v. 87, n. 20, p. 205436, 2013.
- 64 WEPEREN, I. van et al. Spin-orbit interaction in InSb nanowires. **Physical Review B**, v. 91, n. 20, p. 201413, 2015.
- 65 SCHERÜBL, Z. et al. Electrical tuning of Rashba spin-orbit interaction in multigated InAs nanowires. **Physical Review B**, v. 94, n. 3, p. 035444, 2016.
- 66 GOVERNALE, M.; ZÜLICHE, U. Rashba spin splitting in quantum wires. **Solid State Communications**, v. 131, n. 9-10, p. 581 - 589, 2004.
- 67 FABIAN, J. et al. Semiconductor spintronics. **Acta Physica Slovaca**, v. 57, n. 4-5, p. 565, 2007.

- 68 MIRELES, F.; KIRCZENOW, G. Ballistic spin-polarized transport and Rashba spin precession in semiconductor nanowires. **Physical Review B**, v. 64, n. 2, p. 024426, 2001.
- 69 SCHEID, M. et al. All-electrical detection of the relative strength of Rashba and Dresselhaus spin-orbit interaction in quantum wires. **Physical Review Letters**, v. 101, n. 26, p. 266401, 2008.
- 70 BARDEEN, J.; COOPER, L. N.; SCHRIEFFER, J. R. Theory of superconductivity. **Physical Review**, v. 108, n. 5, p. 1175, 1957.
- 71 BOGOLJUBOV, N.; TOLMACHOV, V. V.; ŠIRKOV, D. A new method in the theory of superconductivity. **Fortschritte der Physik**, v. 6, n. 11-12, p. 605, 1958.
- 72 ANDREEV, A. The thermal conductivity of the intermediate state in superconductors. **Journal of Experimental and Theoretical Physics**, v. 46, n. 5, p. 1823, 1964.
- 73 STANESCU, T. D.; TEWARI, S. Majorana fermions in semiconductor nanowires: fundamentals, modeling, and experiment. **Journal of Physics: condensed matter**, v. 25, n. 23, p. 233201, 2013.
- 74 ROTH, L. M.; LAX, B.; ZWERDLING, S. Theory of optical magneto-absorption effects in semiconductors. **Physical Review**, v. 114, n. 1, p. 90, 1959.
- 75 HERMANN, C.; WEISBUCH, C. k.p perturbation theory in III-V compounds and alloys: a reexamination. **Physical Review B**, v. 15, n. 2, p. 823, 1977.
- 76 KISELEV, A. A.; IVCHENKO, E. L.; RÖSSLER, U. Electron g factor in one- and zero-dimensional semiconductor nanostructures. **Physical Review B**, v. 58, n. 24, p. 16353, 1998.
- 77 PRYOR, C. E.; FLATTÉ, M. E. Landé g factors and orbital momentum quenching in semiconductor quantum dots. **Physical Review Letters**, v. 96, n. 2, p. 026804, 2006.
- 78 PFEFFER, P.; ZAWADZKI, W. Anisotropy of spin g factor in GaAs/Ga_{1-x}Al_xAs symmetric quantum wells. **Physical Review B**, v. 74, n. 23, p. 233303, 2006.
- 79 DE, A.; PRYOR, C. E. Calculation of Landé g factors for III-V nanowire quantum dots and comparison with experiment. **Physical Review B**, v. 76, n. 15, p. 155321, 2007.
- 80 YUGOVA, I. A. et al. Universal behavior of the electron g factor in InGaAs/Al_xGa_{1-x}As quantum wells. **Physical Review B**, v. 75, n. 24, p. 245302, 2007.
- 81 GELABERT, M. M.; SERRA, L. g -factor anisotropy of hole quantum wires induced by Rashba interaction. **Physical Review B**, v. 84, n. 7, p. 075343, 2011.
- 82 SANDOVAL, M. A. T. et al. Spin-orbit interaction strength and anisotropy in III-V semiconductor heterojunctions. **Physical Review B**, v. 87, n. 8, p. 081304, 2013.
- 83 INTRONATI, G. A. et al. Spin-orbit effects in nanowire-based wurtzite semiconductor quantum dots. **Physical Review B**, v. 88, n. 4, p. 045303, 2013.
- 84 YANG, L.-W. et al. Tuning of the electron g factor in defect-free GaAs nanodisks. **Physical Review B**, v. 92, n. 24, p. 245423, 2015.

- 85 SANDOVAL, M. T. et al. Electron g factor anisotropy in asymmetric III-V semiconductor quantum wells. **Semiconductor Science and Technology**, v. 31, n. 11, p. 115008, 2016.
- 86 WINKLER, G. W. et al. Orbital contributions to the electron g factor in semiconductor nanowires. **Physical Review Letters**, v. 119, n. 3, p. 037701, 2017.
- 87 TADJINE, A.; NIQUET, Y.-M.; DELERUE, C. Universal behavior of electron g -factors in semiconductor nanostructures. **Physical Review B**, v. 95, n. 23, p. 235437, 2017.
- 88 NILSSON, H. A. et al. Giant, level-dependent g factors in InSb nanowire quantum dots. **Nano Letters**, v. 9, n. 9, p. 3151, 2009.
- 89 SCHROER, M. D. et al. Field tuning the g factor in InAs nanowire double quantum dots. **Physical Review Letters**, v. 107, n. 17, p. 176811, 2011.
- 90 DE LUCA, M. et al. Magneto-optical properties of wurtzite-phase InP nanowires. **Nano Letters**, v. 14, n. 8, p. 4250, 2014.
- 91 ALBRECHT, S. M. et al. Exponential protection of zero modes in Majorana islands. **Nature**, v. 531, n. 7593, p. 206, 2016.
- 92 BELYKH, V. V. et al. Large anisotropy of electron and hole g factors in infrared-emitting InAs/InAlGaAs self-assembled quantum dots. **Physical Review B**, v. 93, n. 12, p. 125302, 2016.
- 93 BJÖRK, M. T. et al. Tunable effective g factor in InAs nanowire quantum dots. **Physical Review B**, v. 72, n. 20, p. 201307, 2005.
- 94 SOUSA, R.; SARMA, S. D. Gate control of spin dynamics in III-V semiconductor quantum dots. **Physical Review B**, v. 68, n. 15, p. 155330, 2003.
- 95 ERLINGSSON, S. I.; EGUES, J. C.; LOSS, D. Energy spectra for quantum wires and two-dimensional electron gases in magnetic fields with Rashba and Dresselhaus spin-orbit interactions. **Physical Review B**, v. 82, n. 15, p. 155456, 2010.
- 96 GHARAATI, A.; KHORDAD, R. Electron g -factor in quantum wire in the presence of Rashba effect and magnetic field. **Superlattices and Microstructures**, v. 51, n. 1, p. 194 – 202, 2012.
- 97 KUMAR, M. et al. Energy dispersion and electron g -factor of quantum wire in external electric and magnetic fields with Rashba spin orbit interaction. **Superlattices and Microstructures**, v. 57, p. 11, 2013. doi: 10.1016/j.spmi.2013.01.007.
- 98 SAKR, M. In-plane electron g -factor anisotropy in nanowires due to the spin-orbit interaction. **Physica E**, v. 64, p. 68 – 71, 2014.
- 99 MAIER, F.; KLOEFFEL, C.; LOSS, D. Tunable g factor and phonon-mediated hole spin relaxation in Ge/Si nanowire quantum dots. **Physical Review B**, v. 87, n. 16, p. 161305, 2013.
- 100 DE ANDRADE E SILVA, E. A.; ROCCA, G. C. L. Rashba spin splitting in semiconductor quantum wires. **Physical Review B**, v. 67, n. 16, p. 165318, 2003.

- 101 HOHENBERG, P.; KOHN, W. Inhomogeneous Electron Gas. **Physical Review**, v. 136, n. 3B, p. B864, 1964.
- 102 KOHN, W.; SHAM, L. J. **Physical Review**, v. 140, n. 4A, p. A1133, 1965.
- 103 SLATER, J. C.; KOSTER, G. F. Simplified LCAO method for the periodic potential problem. **Physical Review**, v. 94, n. 6, p. 1498, 1954.
- 104 HARRISON, W. **Electronic structure and the properties of solids: the physics of the chemical bond**. New York: Dover Publications, 1989. (Dover Books on Physics).
- 105 GORINGE, C. M.; BOWLER, D. R.; HERNÁNDEZ, E. Tight-binding modeling of materials. **Reports on Progress in Physics**, v. 60, n. 12, p. 1447, 1997.
- 106 DE, A.; PRYOR, C. E. Predicted band structures of III-V semiconductors in the wurtzite phase. **Physical Review B**, v. 81, n. 15, p. 155210, 2010.
- 107 PANSE, C.; KRIEGNER, D.; BECHSTEDT, F. Polytypism of GaAs, InP, InAs, and InSb: an *ab initio* study. **Physical Review B**, v. 84, n. 7, p. 075217, 2011.
- 108 CHEIWCHANCHAMNANGIJ, T.; LAMBRECHT, W. R. L. Band structure parameters of wurtzite and zinc-blende GaAs under strain in the GW approximation. **Physical Review B**, v. 84, n. 3, p. 035203, 2011.
- 109 GMITRA, M.; FABIAN, J. First-principles studies of orbital and spin-orbit properties of GaAs, GaSb, InAs, and InSb zinc-blende and wurtzite semiconductors. **Physical Review B**, v. 94, n. 16, p. 165202, 2016.
- 110 GMITRA, M. et al. Band-structure topologies of graphene: spin-orbit coupling effects from first principles. **Physical Review B**, v. 80, p. 235431, 2009.
- 111 GEIM, A. K.; GRIGORIEVA, I. Van der Waals heterostructures. **Nature**, v. 499, n. 7459, p. 419, 2013.
- 112 CHHOWALLA, M. et al. The chemistry of two-dimensional layered transition metal dichalcogenide nanosheets. **Nature Chemistry**, v. 5, n. 4, p. 263, 2013.
- 113 SIPAHI, G. M. et al. Spin polarization of Co(0001)/graphene junctions from first principles. **Journal of Physics: condensed matter**, v. 26, n. 10, p. 104204, 2014.
- 114 JANCU, J.-M. et al. Empirical sp^ds* tight-binding calculation for cubic semiconductors: General method and material parameters. **Physical Review B**, v. 57, n. 11, p. 6493, 1998.
- 115 NIQUET, Y. M. et al. Electronic structure of semiconductor nanowires. **Physical Review B**, v. 73, n. 16, p. 165319, 2006.
- 116 LIAO, G. et al. Electronic structures of [001]- and [111]-oriented InSb and GaSb free-standing nanowires. **Journal of Applied Physics**, v. 118, n. 9, 2015.
- 117 KONSCHUH, S.; GMITRA, M.; FABIAN, J. Tight-binding theory of the spin-orbit coupling in graphene. **Physical Review B**, v. 82, n. 24, p. 245412, 2010.

- 118 FANG, S. et al. Ab initio tight-binding Hamiltonian for transition metal dichalcogenides. **Physical Review B**, v. 92, n. 20, p. 205108, 2015.
- 119 BASTOS, C. M. O. et al. Stability and accuracy control of k.p parameters. **Semiconductor Science and Technology**, v. 31, n. 10, p. 105002, 2016.
- 120 LÖWDIN, P.-O. A note on the quantum-mechanical perturbation theory. **Journal of Chemical Physics**, v. 19, n. 11, p. 1396, 1951.
- 121 ZEIGER, H.; PRATT, G. **Magnetic interactions in solids**. Oxford: Clarendon Press, 1973. (International series of monographs on physics).
- 122 ENDERLEIN, R.; HORING, J. M. N. **Fundamentals of semiconductor physics and devices**. Singapore: World Scientific, 1997.
- 123 LUTTINGER, J.; KOHN, W. Motion of electrons and holes in perturbed periodic fields. **Physical Review**, v. 97, n. 4, p. 869, 1955.
- 124 KANE, E. O. **Physics of III-V compounds**. New York: Academic Press, 1966. v. 1.
- 125 BASTARD, G. **Wave mechanics applied to semiconductor heterostructure**. France: Halsted Press, 1988.
- 126 BARAFF, G.; GERSHONI, D. Eigenfunction-expansion method for solving the quantum-wire problem: formulation. **Physical Review B**, v. 43, n. 5, p. 4011, 1991.
- 127 BURT, M. G. The justification for applying the effective-mass approximation to microstructures. **Journal of Physics: condensed matter**, v. 4, n. 32, p. 6651, 1992.
- 128 YU, P. Y.; CARDONA, M. **Fundamentals of semiconductors:: physics and materials properties**. Berlin: Springer, 2010.
- 129 DE ANDRADE E SILVA, E. A. Conduction-subband anisotropic spin splitting in iii-v semiconductor heterojunctions. **Physical Review B**, v. 46, n. 3, p. 1921, 1992.
- 130 DE ANDRADE E SILVA, E. A.; ROCCA, G. C. L.; BASSANI, F. Spin-split subbands and magneto-oscillations in III-V asymmetric heterostructures. **Physical Review B**, v. 50, n. 12, p. 8523, 1994.
- 131 _____. Spin-orbit splitting of electronic states in semiconductor asymmetric quantum wells. **Physical Review B**, v. 55, n. 24, p. 16293, 1997.
- 132 WINKLER, R. **Spin-orbit coupling effects in two-dimensional electron and hole systems**. Berlin: Springer, 2003. (Springer tracts in modern physics, no. 191).
- 133 ZHANG, X. W.; XIA, J. B. Rashba spin-orbit coupling in InSb nanowires under transverse electric field. **Physical Review B**, v. 74, n. 7, p. 075304, 2006.
- 134 BERNARDES, E. et al. Spin-orbit interaction in symmetric wells with two subbands. **Physical Review Letters**, v. 99, n. 7, p. 076603, 2007.
- 135 CALSAVERINI, R. S. et al. Intersubband-induced spin-orbit interaction in quantum wells. **Physical Review B**, v. 78, n. 15, p. 155313, 2008.

- 136 LIU, Q. et al. Orbital mapping of energy bands and the truncated spin polarization in three-dimensional rashba semiconductors. **Physical Review B**, v. 94, n. 12, p. 125207, 2016.
- 137 ERLINGSSON, S. I.; EGUES, J. C. All-electron topological insulator in InAs double wells. **Physical Review B**, v. 91, n. 3, p. 035312, 2015.
- 138 TARASENKO, S. A. et al. Split dirac cones in HgTe/CdTe quantum wells due to symmetry-enforced level anticrossing at interfaces. **Physical Review B**, v. 91, n. 8, p. 081302, 2015.
- 139 PARK, S.-H.; AHN, D.; CHUANG, S.-L. Electronic and optical properties of a- and m-plane wurtzite InGaN-GaN quantum wells. **IEEE Journal of Quantum Electronics**, v. 43, n. 12, p. 1175, 2007.
- 140 FORTUNA, S. A.; LI, X. Metal-catalyzed semiconductor nanowires: a review on the control of growth directions. **Semiconductor Science and Technology**, v. 25, n. 2, p. 024005, 2010.
- 141 KROGSTRUP, P. et al. Epitaxy of semiconductor–superconductor nanowires. **Nature Materials**, v. 14, n. 4, p. 400, 2015.
- 142 HJORT, M. et al. Electronic and structural differences between wurtzite and zinc blende InAs nanowire surfaces: experiment and theory. **ACS Nano**, v. 8, n. 12, p. 12346–12355, 2014.
- 143 PFEFFER, P.; ZAWADZKI, W. Five-level $k \cdot p$ model for the conduction and valence bands of GaAs and InP. **Physical Review B**, v. 53, n. 19, p. 12813, 1996.
- 144 FARIA JUNIOR, P. E. et al. Realistic multiband $k \cdot p$ approach from *ab initio* and spin-orbit coupling effects of InAs and InP in wurtzite phase. **Physical Review B**, v. 93, n. 23, p. 235204, 2016.
- 145 CHUANG, S. L.; CHANG, C. S. $k \cdot p$ method for strained wurtzite semiconductors. **Physical Review B**, v. 54, n. 4, p. 2491, 1996.
- 146 BERESFORD, R. Full-zone $k \cdot p$ method of band structure calculation for wurtzite semiconductors. **Journal of Applied Physics**, v. 95, n. 11, p. 6216–6224, 2004.
- 147 RINKE, P. et al. Consistent set of band parameters for the group-III nitrides AlN, GaN, and InN. **Physical Review B**, v. 77, n. 7, p. 075202, 2008.
- 148 FU, J. Y.; WU, M. W. Spin-orbit coupling in bulk ZnO and GaN. **Journal of Applied Physics**, v. 104, n. 9, p. 093712, 2008.
- 149 VOON, L.; WILLATZEN, M. **The $k \cdot p$ method**: electronic properties of semiconductors. Berlin: Springer, 2009.
- 150 MARNETTO, A.; PENNA, M.; GOANO, M. An accurate dual-expansion-point full-brillouin-zone $k \cdot p$ model for wurtzite semiconductors. **Journal of Applied Physics**, v. 108, n. 3, p. 033701, 2010.
- 151 FARIA JUNIOR, P. E.; SIPAHI, G. M. Band structure calculations of InP wurtzite/zinc-blende quantum wells. **Journal of Applied Physics**, v. 112, n. 10, p. 103716, 2012.

- 152 MIAO, M. S. et al. Polarization-driven topological insulator transition in a GaN/InN/GaN quantum well. **Physical Review Letters**, v. 109, n. 18, p. 186803, 2012.
- 153 EHRHARDT, M.; KOPRUCKI, T. **Multi-band effective mass approximations: advanced mathematical models and numerical techniques**. Berlin: Springer, 2014. (Lecture notes in computational science and engineering).
- 154 BERNEVIG, B.; HUGHES, T. **Topological insulators and topological superconductors**. Princeton: Princeton University Press, 2013.
- 155 HERLACH, F. On the cyclotron effective mass of GaAs. **Journal of Physics C**, v. 7, n. 16, p. L308, 1974.
- 156 BECKER, W. M.; RAMDAS, A. K.; FAN, H. Y. Energy band structure of gallium antimonide. **Journal of Applied Physics**, v. 32, n. 10, p. 2094, 1961.
- 157 SPITZER, W. G.; FAN, H. Y. Determination of optical constants and carrier effective mass of semiconductors. **Physical Review**, v. 106, n. 5, p. 882, 1957.
- 158 CARDONA, M. Electron effective masses of InAs and GaAs as a function of temperature and doping. **Physical Review**, v. 121, n. 3, p. 752, 1961.
- 159 DUGDALE, D. J.; BRAND, S.; ABRAM, R. A. Direct calculation of $\mathbf{k} \cdot \mathbf{p}$ parameters for wurtzite AlN, GaN, and InN. **Physical Review B**, v. 61, n. 19, p. 12933, 2000.
- 160 RAMOS, L. E. et al. Structural, electronic, and effective-mass properties of silicon and zinc-blende group-III nitride semiconductor compounds. **Physical Review B**, v. 63, n. 16, p. 165210, 2001.
- 161 KANE, E. O. Band structure of indium antimonide. **Journal of Physics and Chemistry of Solids**, v. 1, n. 4, p. 249, 1957.
- 162 PIDGEON, C. R.; BROWN, R. N. Interband magneto-absorption and faraday rotation in InSb. **Physical Review**, v. 146, n. 2, p. 575, 1966.
- 163 SUZUKI, K.; HENSEL, J. C. Quantum resonances in the valence bands of germanium. i. theoretical considerations. **Physical Review B**, v. 9, n. 10, p. 4184, 1974.
- 164 TREBIN, H. R.; RÖSSLER, U.; RANVAUD, R. Quantum resonances in the valence bands of zinc-blende semiconductors. i. theoretical aspects. **Physical Review B**, v. 20, n. 2, p. 686, 1979.
- 165 CARDONA, M.; CHRISTENSEN, N. E.; FASOL, G. Relativistic band structure and spin-orbit splitting of zinc-blende-type semiconductors. **Physical Review B**, v. 38, n. 3, p. 1806, 1988.
- 166 PFEFFER, P.; ZAWADZKI, W. Conduction electrons in GaAs: five-level $k \cdot p$ theory and polaron effects. **Physical Review B**, v. 41, n. 3, p. 1561, 1990.
- 167 LUTTINGER, J. M. Quantum theory of cyclotron resonance in semiconductors: general theory. **Physical Review**, v. 102, n. 4, p. 1030, 1956.
- 168 VURGAFTMAN, I.; MEYER, J. R.; RAM-MOHAN, L. R. Band parameters for III-V compound semiconductors and their alloys. **Journal of Applied Physics**, v. 89, n. 11, p. 5815, 2001.

- 169 JANCU, J.-M. et al. Atomistic spin-orbit coupling and k.p parameters in III-V semiconductors. **Physical Review B**, v. 72, n. 19, p. 193201, 2005.
- 170 DICK, K. A. et al. Control of III–V nanowire crystal structure by growth parameter tuning. **Semiconductor Science and Technology**, v. 25, n. 2, p. 024009, 2010.
- 171 KROGSTRUP, P. et al. Structural phase control in self-catalyzed growth of GaAs nanowires on silicon (111). **Nano Letters**, v. 10, n. 11, p. 4475, 2010.
- 172 FARIA JUNIOR, P. E.; CAMPOS, T.; SIPAHI, G. M. Interband polarized absorption in InP polytypic superlattices. **Journal of Applied Physics**, v. 116, n. 19, p. 193501, 2014.
- 173 GADRET, E. G. et al. Valence-band splitting energies in wurtzite InP nanowires: Photoluminescence spectroscopy and ab initio calculations. **Physical Review B**, v. 82, n. 12, p. 125327, 2010.
- 174 CHUANG, S. L.; CHANG, C. S. A band-structure model of strained quantum-well wurtzite semiconductors. **Semiconductor Science and Technology**, v. 12, n. 3, p. 252, 1997.
- 175 STIER, O.; BIMBERG, D. Modeling of strained quantum wires using eight-band k-p theory. **Physical Review B**, v. 55, n. 12, p. 7726, 1997.
- 176 VEPREK, R. G.; STEIGER, S.; WITZIGMANN, B. Reliable k.p band structure calculation for nanostructures using finite elements. **Journal of Computational Electronics**, v. 7, n. 4, p. 521, 2008.
- 177 MEI, T. Fourier transform-based k.p method of semiconductor superlattice electronic structure. **Journal of Applied Physics**, v. 102, n. 5, p. 053708, 2007.
- 178 PRESS, W. **Numerical recipes in C: the art of scientific computing**. Cambridge: Cambridge University Press, 2007.
- 179 VUKMIROVĆ, N.; TOMIĆ, S. Plane wave methodology for single quantum dot electronic structure calculations. **Journal of Applied Physics**, v. 103, n. 10, p. 103718, 2008.
- 180 PÉREZ-JORDÁ, J. M. Fast solution of elliptic partial differential equations using linear combinations of plane waves. **Physical Review E**, v. 93, n. 2, p. 023304, 2016.
- 181 FOREMAN, B. A. Elimination of spurious solutions from eight-band $\mathbf{k} \cdot \mathbf{p}$ theory. **Physical Review B**, v. 56, n. 20, p. R12748, 1997.
- 182 CARTOIXÀ, X.; TING, D. Z.-Y.; MCGILL, T. C. Numerical spurious solutions in the effective mass approximation. **Journal of Applied Physics**, v. 93, n. 7, p. 3974, 2003.
- 183 VEPREK, R. G.; STEIGER, S.; WITZIGMANN, B. Ellipticity and the spurious solution problem of $\mathbf{k} \cdot \mathbf{p}$ envelope equations. **Physical Review B**, v. 76, n. 16, p. 165320, 2007.
- 184 EISSFELLER, T.; VOGL, P. Real-space multiband envelope-function approach without spurious solutions. **Physical Review B**, v. 84, n. 19, p. 195122, 2011.

- 185 WINKLER, R. Spin orientation and spin precession in inversion-asymmetric quasi-two-dimensional electron systems. **Physical Review B**, v. 69, n. 4, p. 045317, 2004.
- 186 KAMMERMEIER, M. et al. Weak (anti)localization in tubular semiconductor nanowires with spin-orbit coupling. **Physical Review B**, v. 93, n. 20, p. 205306, 2016.
- 187 VOON, L. C. L. Y. et al. Terms linear in k in the band structure of wurtzite-type semiconductors. **Physical Review B**, v. 53, n. 16, p. 10703, 1996.
- 188 OPPEN, F. V.; PENG, Y.; PIENKA, F. **Topological superconducting phases in one dimension**. Available from: <http://www.physik.fu-berlin.de/en/einrichtungen/ag/ag-von-oppen/papers/lecture_Oppen.pdf>. Accessible at: 28 Jul. 2017.
- 189 BASTARD, G. Superlattice band structure in the envelope-function approximation. **Physical Review B**, v. 24, n. 10, p. 5693, 1981.
- 190 XIA, J.-B.; CHANG, Y.-C. Theory of the electronic structure of porous Si. **Physical Review B**, v. 48, n. 8, p. 5179, 1993.
- 191 TOMOV, S.; DONGARRA, J.; BABOULIN, M. Towards dense linear algebra for hybrid GPU accelerated manycore systems. **Parallel Computing**, v. 36, n. 5-6, p. 232, 2010.
- 192 TOMOV, S. et al. **Dense linear algebra solvers for multicore with GPU accelerators**. 2010. Available from: <http://ieeexplore.ieee.org/stamp/stamp.jsp?arnumber=5470941>. Accessible at: 24. Jul. 2017.
- 193 DONGARRA, J. et al. **Accelerating numerical dense linear algebra calculations with GPUs**. 2014. Available from: <https://pdfs.semanticscholar.org/833c/7267a2948259917ad06a78e3abd4fe2dcccfd.pdf>. Accessible at: 24. Jul. 2017.
- 194 HEWITT, E.; HEWITT, R. E. The Gibbs-Wilbraham phenomenon: An episode in fourier analysis. **Archive for History of Exact Sciences**, v. 21, n. 2, p. 129, 1979.
- 195 NUTTALL, A. Some windows with very good sidelobe behavior. **IEEE Transactions on Acoustics, Speech, and Signal Processing**, v. 29, n. 1, p. 84–91, 1981.
- 196 RÖSSLER, U.; KAINZ, J. Microscopic interface asymmetry and spin-splitting of electron subbands in semiconductor quantum structures. **Solid State Communications**, v. 121, n. 6-7, p. 313, 2002.
- 197 RASHBA, E.; SHEKA, V. Symmetry of energy bands in crystals of wurtzite type II. symmetry of bands with spin-orbit interaction included. **Fizika Tverdogo Tela**, v. 1, n. 2, p. 162, 1959.
- 198 LITVINOV, V. I. Electron spin splitting in polarization-doped group-III nitrides. **Physical Review B**, v. 68, n. 15, p. 155314, 2003.
- 199 RODRIGUES, S. C. P. et al. Charge and spin distributions in $\text{Ga}_{1-x}\text{Mn}_x\text{As}/\text{GaAs}$ ferromagnetic multilayers. **Physical Review B**, v. 70, n. 16, p. 165308, 2004.

200 SIPAHI, G. M. et al. Charge and spin distribution in ferromagnetic Mn-doped InGaAs/GaAs multilayers. **Applied Physics Letters**, v. 85, n. 25, p. 6209, 2004.